University College London

Computational studies of magnetite Fe_3O_4 and related spinel-structured materials

Thesis submitted for the degree of Doctor of Philosophy (PhD) by

David Santos Carballal

Supervised by

Prof. Nora H. de Leeuw

University College London

Department of Chemistry

March 2015

Declaration

I, David Santos Carballal, confirm that the work presented in this thesis is my own. Where information has been derived from other sources, I confirm that this has been indicated in the thesis.

David Santos Carballal

March 2015

Abstract

This thesis presents the results of *ab initio* based simulation studies of magnetite (Fe_3O_4) and related FeM_2X_4 (thio)spinels with M = Cr, Mn, Fe, Co and Ni and X = O and S. Using density functional theory with long-range dispersion correction and on-site Coulomb interactions (DFT + U – D2), we have investigated a number of properties of these materials.

Firstly, we present a study of the inversion degree and its relevance in the electronic structure and magnetic properties of the spin filter candidates FeM_2X_4, which are one of the key devices in spintronic applications. We also analyze the role played by the size of the ions and by the crystal field stabilization effects in determining the equilibrium inversion degree. Secondly, we present the calculations of the elastic constants and other macroscopic mechanical properties by applying elastic strains on the unit cell of Fe_3O_4, which is the main component in different types of catalysts used in myriad of industrial processes. Thirdly, we calculate the geometries and surface free energies of a number of Fe_3O_4 surfaces at different compositions, including the non-dipolar stoichiometric plane, and those with a deficiency or excess of oxygen atoms. We propose a morphology in thermodynamic equilibrium conditions for the nanocrystals of this compound. We also present the simulated scanning tunnelling microscopy images of the different terminations of the surfaces shown on the Fe_3O_4 morphology. Finally, we investigate the initial oxidation stages of the greigite (Fe_3S_4) (001) surface induced by water. Fe_3S_4 is a mineral widely identified in anoxic aquatic environments and certain soils, which can be oxidised by these environments

producing and extremely acid solution of sulfur-rich wastewater called acid mine drainage (AMD). We propose a number of mechanisms involving one or two water molecules and one OH group to explain the replacement of one sulfur by one oxygen atom in this mineral.

The findings presented in this thesis provides a theoretical insight into various bulk and surface properties of this group of compounds.

Table of contents

Acknowledgments

Firstly, I would like to thank my supervisor, Professor Nora de Leeuw, for opening the doors of her group to me and for giving me the professional possibilities that I would have never dreamt of. I am also very grateful to her for introducing me to the materials modelling field and being a source of support and guidance during the last four years.

I also would like to express my special gratitude to Dr Alberto Roldan, Dr Ricardo Grau-Crespo and Dr Zhimei Du for their invaluable help and guidance at different stages of my postgraduate studies at UCL. I would also like to thank all my colleagues that have made my stay at UCL a memorable time in my life and especially to Ashley Shields, who was always happy to read my writings.

I am very grateful for a Graduate Global Excellence Award from UCL and an Overseas Research Scholarship from the UCL Industrial Doctorate Centre in Molecular Modelling and Materials Science. I also acknowledge the use of the computer clusters on which this work was carried out, including HECToR, ARCHER, IRIDIS and Legion supercomputers, as well as Huygens and IB-server clusters.

Finally, thank you to my mum, my grandmother Teresita, sister, aunties and the rest of my family in Cuba, who encouraged me and supported my decision of doing a PhD. I would also like to thank my cousin Jorge Luis and his family in Costa Rica for their invaluable help, as well as my wife Jiayu, for her love and understanding at this time. I would like to dedicate this thesis to the memory of my dad and grandmother Lolita.

List of publications

The work described in this thesis has been published in the following papers:

Roldan, A., **Santos-Carballal, D.**, & de Leeuw, N. H. (2013). A Comparative DFT Study of the Mechanical and Electronic Properties of Greigite Fe_3S_4 and Magnetite Fe_3O_4. *The Journal of Chemical Physics*, *138*(20), 204712. doi:10.1063/1.4807614.

Santos-Carballal, D., Roldan, A., Grau-Crespo, R., & de Leeuw, N. H. (2014). A DFT Study of the Structures, Stabilities and Redox Behaviour of the Major Surfaces of Magnetite Fe_3O_4. *Physical Chemistry Chemical Physics*, *16*(39), 21082–21097. doi:10.1039/c4cp00529e.

Santos-Carballal, D., Roldan, A., Grau-Crespo, R., & de Leeuw, N. H. (2014). First-Principles Study of the Inversion Thermodynamics and Electronic Structure of $Fe\mathit{M}_2\mathit{X}_4$ (Thio)Spinels (M = Cr, Mn, Co, Ni; X = O, S). *Submitted to Physical Review B*.

Santos-Carballal, D., Roldan, A., & de Leeuw, N. H. (2014). Initial Oxidation of the Greigite Fe_3S_4(001) Surface Induced by Water: A Density Functional Theory Study. *To be submitted*.

List of abbreviations

AES: Auger electron spectroscopy

AMD: Acid mine drainage

APDB: Antiphase domain boundaries

ARD: Acid rock drainage

CG: Conjugate gradients

DFT: Density functional theory

DFT – D2: Method combining the DFT energy with a correction to the long-range dispersion interactions

DFT + *U*: Method combining a DFT Hamiltonian with a Hubbard Hamiltonian for the description of the on-site Coulomb interactions

DOS: Density of states

GGA: Generalized gradient approximation

HF: Hartree Fock

HMF: Half-metallic ferrimagnets

HSE: Hybrid density functional that incorporates 25% of Hartree Fock exchange developed by Heyd, Scuseria and Ernzerhof

IDM: Improved dimer method

KS: Kohn-Sham

LDA: Local density approximation

LDOS: Local density of states

LEED: Low-energy electron diffraction

LEEM: Low-energy electron microscopy

LEIS: Low-energy ion scattering

LPAW: Linear augmented plane-wave

ML: Mono layer

NCPP: Norm-conserving pseudopotentials

PAW: Projector augmented-wave

PBE: Generalized gradient approximation density functional developed by Perdew, Burke and Ernzerhof

PBEsol: Revision of the PBE functional for solids

PDOS: Projected density of states

PW91: Generalized gradient approximation density functional developed by Perdew and Wang

RHEED: Reflection high-energy electron diffraction

RMM-DIIS: Residual minimisation method-direct inversion in the iterative subspace

SD: Steepest descent

SNG: Substitute natural gas

STM: Scanning tunnelling microscopy

STS: Scanning tunnelling spectroscopy

TS: Tkatchenko-Scheffler

USPP: Ultrasoft pseudopotentials

VASP: Vienna *Ab-initio* Simulation Package

VSEPR: Valence Shell Electron Pair Repulsion

VWN: Vosko, Wilk and Nusair

WGS: Water gas shift

XPD: X-ray photoelectron diffraction

XPS: X-ray photoelectron spectroscopy

XRD: X-rays diffraction

List of tables

List of figures

1

Magnetite Fe_3O_4 and related spinel-structured materials

1.1 Introduction

In this thesis, we present a computational investigation of the solid state chemistry of (thio)spinels and the surface chemistry of magnetite (Fe_3O_4) and greigite (Fe_3S_4). These group of compounds occur naturally in many of the Earth's layers, such as the lithosphere, pedosphere and biosphere, where they play an important role in the interrelationship between them via cyclic processes of redistribution and transformation. Therefore, (thio)spinels are of interest in various scientific disciplines and their research has led to a vast collection of interdisciplinary communications whose outcomes have been rather inconclusive at times. For instance, the conduction and magnetic properties of the (thio)spinels and their relationship with the equilibrium inversion degree have not yet been systematically explained, which is essential for spintronic applications. The nature of the forces operating on Fe_3O_4 and their effect on the mechanical and dynamical properties of this compound have not yet been elucidated. Moreover, although Fe_3O_4 is widely used as the main component of

industrial catalysts in myriad processes, there is no agreement in either the termination of its main surfaces or the thermodynamics of the redox reactions taking place on them. Similarly, the initial oxidation process of the Fe_3S_4(001) surface is still largely unknown. Fe_3S_4 is a mineral thought to have played an important catalytic role in the iron-sulfur origin of life theory (Russell and Hall, 1997) and may contribute to the formation of acid mine drainage (AMD).

In this chapter, we review the natural occurrences of these materials, especially Fe_3O_4, and their synthetic preparation. We present the common characteristics of the crystal structure and morphology of the spinel group and discuss the electronic and magnetic properties of this group of materials and their applications, mainly as catalysts.

1.2 Natural occurrence and synthesis

1.2.1 Rocks, ores and soils

Magnetite also known as "lodestone" or "loadstone", which is a portmanteau of the words "leading" and "stone", has been used as the orientation element since the earliest compasses due to its magnetic properties. Its name derives possibly from the Greek region of Magnesia (Anthony *et al.*, n.d.). Fe_3O_4 is found ubiquitously in all of the three groups of rocks forming the lithosphere, *i.e.* magmatic (Frost and Lindsley, 1991), metamorphic (Frost, 1991) and sedimentary (Morad and Aldahan, 1986) rocks. In all these environments, and especially in the magmatic rocks, magnetite appears forming solid solutions known generically as titanomagnetites ($Fe_{3-x}Ti_xO_4$) (Grant, 1985), where usually $0.0 < x < 0.8$ (Frost and Lindsley, 1991). Other ions such as Ni,

Cr, Mn and Co, can also replace Fe in small amounts (Sidhu *et al.*, 1980, 1978). Sedimentary Fe_3O_4 is found forming deposits of banded iron formation (Huberty *et al.*, 2012), iron stones in purely sedimentary ores (Torres-Ruiz, 1983) or deep sea sediments (Petersen *et al.*, 1986) with both detrital and biogenic origin. Fe_3O_4 is also found in certain soils of the pedosphere, where two formation routes are suggested, namely *in situ* inorganic formation of this mineral (Maher and Taylor, 1988) or its accumulation from dead magnetotactic bacteria (Fassbinder *et al.*, 1990). Finally, Fe_3O_4 is an important component of meteorites coming from Mars, which suggests the presence of this iron oxide phase on that planet's surface (Bradley *et al.*, 1996).

Greigite is named after Dr JW Greig (1895−1977), who was an American mineralogist and physical chemist (Anthony *et al.*, n.d.). Although Fe_3S_4 is not the most stable iron sulfide structure, it has been widely identified in anoxic aquatic environments, such as marine (Roberts and Turner, 1993), brackish (Jelinowska *et al.*, 1998) or fresh water (Jelinowska *et al.*, 1995; Snowball, 1991) as well as during the formation of certain soils (Fassbinder *et al.*, 1990; Fassbinder and Stanjek, 1994). Layers of Fe_3S_4 have been found in lacustrine sediments consisting of interbedded clastics, aragonite, silt, sand or clay (Frank *et al.*, 2007) as well as in varved-like laminae of alternating sulfide-bearing and sulfide-free layers (Skinner *et al.*, 1964).

Chromite ($FeCr_2O_4$) derives its name from its content of chromium (Anthony *et al.*, n.d.). $FeCr_2O_4$ is an accessory cumulus mineral in layered peridotites (Cameron, 1978), an ultramafic rock classified as magmatic, which has low silica and high iron and magnesium content. The presence of $FeCr_2O_4$ on mafic and ultramafic rocks can also

have a detrital origin (Lee, 1999). Relic $FeCr_2O_4$ is also common in fossil meteorites (Bunch *et al.*, 1967; Nyström *et al.*, 1988; Ramdohr, 1967) and in those meteorites coming from the mare regions of the moon (Arai *et al.*, 1996; Papike *et al.*, 1976).

Daubréelite ($FeCr_2S_4$) is named in honour to Professor GA Daubrée (1814−1896), who was a French meteorite researcher (Anthony *et al.*, n.d.). Small amounts of $FeCr_2S_4$ are found naturally only in meteorites (Chikamii *et al.*, 1999; El Goresy, 1967).

Violarite ($FeNi_2S_4$) derives its name from the violet colour of its polished surface (Anthony *et al.*, n.d.). $FeNi_2S_4$ occurs rarely as a product of the initial alteration of nickel ores near the earth surface (Arnold and Malik, 1974).

1.2.2 Organisms

Biominerals are inorganic solids produced by living organisms. The formation of these minerals can follow one of two routes according to the level of complexity of the producing organism. For example, (1) in animals, biominerals formation is mediated by an organic support or membrane surface, while in (2) some bacterial and algae species, the biomineralization process is induced by favourable chemical conditions (Lowenstam, 1981). Amongst all the compounds relevant to this thesis, only Fe_3O_4 and Fe_3S_4 are biotically formed.

Magnetite formed biotically has been reported in the teeth of chitons (Lowenstam, 1962). Biogenic Fe_3O_4 has also been found in magnetotactic bacteria (the type of microorganisms that use this mineral for orientation porpoises) in marine environments (Blakemore, 1975), anaerobic soils (Fassbinder *et al.*, 1990) and in lakes

(Vali and Kirschvink, 1991) as well as in magnetotactic algae in brackish sediments (Torres de Araujo *et al.*, 1986). Fe_3O_4 is also found in honey bees (Gould *et al.*, 1978) and in the skull of homing pigeons (Walcott *et al.*, 1979), where it seems to have the same function than in magnetotactic bacteria. In the chitons (Kirschvink and Lowenstam, 1979; Lowenstam, 1981; Nesson and Lowenstam, 1985) and bacteria (Mann *et al.*, 1989), the mechanism for the Fe_3O_4 biomineralization is supposed to be similar and it involves the reaction of ferrihydrite with dissolved Fe^{2+}, according to the following process:

$$5Fe^{2+} + 2Fe_5HO_8 + 4H_2O \rightarrow 5Fe_3O_4 + 10H^+ \qquad (1.1)$$

Biogenic **greigite** has also being identified in magnetotactic bacteria from brackish, sulfide-rich waters and sediments (Mann *et al.*, 1990) as well as in the scales of a hydrothermal vent gastropod (Goffredi *et al.*, 2004). Biologically produced Fe_3O_4 and Fe_3S_4 may persist once the organism that formed it has died and may therefore, contribute to the natural magnetic remanence of sediments (Stolz *et al.*, 1986), as was discussed above.

To the best of our knowledge, **$FeNi_2O_4$**, **$FeMn_2O_4$**, **$FeMn_2S_4$**, **$FeCo_2O_4$** and **$FeCo_2S_4$** do not occur naturally in the lithosphere, pedosphere or biosphere.

1.2.3 Synthetic preparation

Magnetite is usually extracted from rock ores, which are the primary source of iron oxides (Cornell and Schwertmann, 2003). Fe_3O_4 can also be synthesised in the laboratory by a number of different hydrothermal methods. The first method reported

for the synthesis of Fe_3O_4, known as Schikorr reaction (Schikorr, 1929), involves the oxidation of $Fe(OH)_2$, obtained from the alkaline hydrolysis of $FeSO_4$, using heat under inert atmosphere, as follows:

$$3Fe(OH)_2 \rightarrow Fe_3O_4 + 2H_2O + H_2 \qquad (1.2)$$

However, this method was never very convenient due to complicated side reactions and it was later modified by starting from various Fe^{2+} salts in solution and adding different types of oxidizing agents (David and Welch, 1956; Regazzoni *et al.*, 1981; Sarel *et al.*, 1989). There are other types of methods for synthesising Fe_3O_4 that instead favour the reduction of Fe^{3+} compounds (Booy and Swaddle, 1978; Kominami *et al.*, 1999) or the combination of Fe^{2+}/Fe^{3+} ions in solution (Regazzoni *et al.*, 1981).

Greigite is formed as an intermediate in the solid-state transformation of mackinawite (FeS) into pyrite (FeS_2) (Benning *et al.*, 2000; Dekkers and Schoonen, 1996; Hunger and Benning, 2007; Wilkin and Barnes, 1996). The model for the FeS to Fe_3S_4 transition proposed by Lennie *et al.* (1997) requires the diffusion of approximately two of every four Fe^{2+} cations from tetrahedral sites in FeS to octahedral sites in Fe_3S_4, with the concomitant oxidation of half the migrating Fe^{2+} to Fe^{3+}. Fe_3S_4 can also be formed via a hydrothermal method, in which a solution of sulfide and elemental sulfur is mixed with heat in stoichiometric proportions with another containing an Fe^{2+} salt (Dekkers and Schoonen, 1994; Horiuchi *et al.*, 1974).

Chromite crystals can be grown in the laboratory through the chemical vapour transport method. This technique requires high temperatures to heat a stoichiometric mixture of FeO and Cr_2O_3 inside an evacuated quartz tube to obtain a polycrystalline

powder of $FeCr_2O_4$. This sample requires further thermic treatment in presence of $CrCl_3$, the transport agent, to obtain single crystals (Bordács *et al.*, 2009; Ohgushi *et al.*, 2008). $FeCr_2O_4$ is also formed by firing a mixture of Fe_2O_3 and Cr_2O_3 in an atmosphere of CO_2 and H_2 or CO at 950 − 1300 °C (Klemme *et al.*, 2000; Tanaka *et al.*, 1966), or in vacuum by adding also pure Fe and heating (Shirane *et al.*, 1964). $FeCr_2O_4$ can also be prepared through combustion of a mixture of the stoichiometric amounts of aqueous saturated solutions of $Fe(NO_3)_2$, $Cr(NO_3)_3$ and urea (Manoharan and Patil, 1992).

Daubréelite polycrystalline powders are prepared from a heated mixture of the stoichiometric amount of elemental Fe, Cr and S (Kim, 2004; Ramirez *et al.*, 1997; Shirane *et al.*, 1964). Further heating of $FeCr_2S_4$ powder in the presence of transport agent can also lead to single crystals (Ohgushi *et al.*, 2008). $FeCr_2S_4$ nanocrystals are also formed via a wet chemistry method, where iron(II) acetylacetonate, chromium(III) acetylacetonate and 1-dodecanethiol in stoichiometric amounts are dissolved in oleylamine and heated at 335 °C for 30 minutes (Mao and Lee, 2014).

$FeNi_2O_4$ is synthesised by co-precipitating the hydroxides of iron and nickel with NaOH, followed by heat treatment at a pressure of 140 atm (Shafer, 1962). **Violarite** is formed by heating a stoichiometric mixture of elemental Fe, Ni and S (Tenailleau *et al.*, 2006; Townsend *et al.*, 1977).

$FeCo_2O_4$ is synthesised by heating a mixture of Fe_2O_3 and Co_2O_3 in stoichiometric proportions (Murray and Linnett, 1976; Muthuselvam and Bhowmik, 2009). $FeCo_2O_4$ is also prepared by co-precipitating the iron and cobalt hydroxydes, from an aqueous

solution of $FeCl_3$ and $CoCl_2$ prepared in 1:2 molar ratio, by adding a basic solution under heat (Ferreira *et al.*, 2003). A *chimie douce* method has been used for the preparation of $FeCo_2O_4$, where a concentrated solution of $FeCl_2$ and $CoCl_2$, prepared in a 1:2 ratio, is made to react with oxalic acid to precipitate an oxalate precursor, which transforms into the spinel with heat (Le Trong *et al.*, 2008).

The synthesis of **$FeCo_2S_4$**, **$FeMn_2O_4$** and **$FeMn_2S_4$** have not been reported until this date.

1.3 Crystal structure and morphology of spinels

1.3.1 Crystal structure of spinels

The spinel structure is named after the mineral spinel $MgAl_2O_4$. This structure is characteristic of compounds with chemical formula $M'M_2X_4$, where M' and M represent metallic cations and X is an oxygen or bivalent chalcogen anion (in this thesis, M' = Fe; M = Cr, Mn, Fe, Co, Ni and X = O, S). The spinel structure is composed by a face-centred cubic unit cell based on 32 X anions which are nearly regularly close packed. Amongst the holes created by the anions' arrangement, 8 of the tetrahedral (A) and 16 of the octahedral (B) are occupied by cations. For the compounds of interest in this thesis where all Fe ions are in the tetrahedral positions, the symmetry corresponds to the $Fd\bar{3}m$ space group (Krupicka and Novak, 1982). The most common oxidation states of the transition metals in spinels are 2+, 3+ and 4+ which leads to two types of spinels. The 2−3 type has two 3+ and one 2+ cations per formula unit while the 4−2

type has two 2+ and one 4+ cations per formula unit. According to this classification, all the compositions studied in this thesis are 2−3 spinels.

Magnetite has the cubic spinel structure (Bragg, 1915) above the Verwey temperature (T_V = 122 K) (Verwey, 1939) and below this temperature it becomes monoclinic (Wright *et al.*, 2002). **Chromite** and **$FeMn_2O_4$** also have the cubic spinel structure above the Jahn-Teller temperature (T_{JT} = 135 (Shirane *et al.*, 1964) and 473 K respectively (Van Landuyt *et al.*, 1972)). Below these temperatures, the crystals become tetragonal.

Gregite, **daubréelite**, **$FeNi_2O_4$**, **violarite** and **$FeCo_2O_4$** have no first-order phase transition found.

1.3.2 Morphology of spinel crystals

Magnetite crystals, both synthetic and natural, have been described with octahedral morphologies enclosed by (111) planes and octahedral with truncated corners morphologies by adding the (001) surfaces. Twinning has also been reported and it occurs on the (111) plane. Hydrothermal methods usually produce rounded, cubic or octahedral crystals, whose dimensions can be controlled by modifying the initial reactants and chemical conditions. For example, precipitation of Fe_3O_4 in neutral (Regazzoni *et al.*, 1981; Taylor and Schwertmann, 1974) and mild acid (Couling and Mann, 1985; Sidhu *et al.*, 1978) conditions give particles sized smaller than 0.1 μm. Larger (0.03−1.1 μm) octahedral and sphere particles can be obtained in mild basic conditions (David and Welch, 1956; Sugimoto and Matijević, 1980), while a strong basic environment favours cubic crystals (Feitknecht, 1959). Fe_3O_4 crystals capping

the teeth of chitons display different sizes and morphologies (Towe and Lowenstam, 1967; Webb *et al.*, 1989). However, those found in magnetotactic bacteria are hexagonal, rectangular, cubic, bullet shaped (Schüler, 1999) or forming twins (Devouard *et al.*, 1998). These morphologies are based on the octahedral and elongated hexagonal prism which can be obtained combining the (111), (001) and (010) surfaces (Devouard *et al.*, 1998; Mann and Frankel, 1989).

Greigite from sediments also shows octahedral crystal morphology (Roberts and Weaver, 2005; Skinner *et al.*, 1964) or platy and needle-like particles 5−15 μm size (Snowball and Thompson, 1990a, 1990b). Biogenic Fe_3S_4 crystals have octahedral shape with truncated corners (Heywood *et al.*, 1990), a morphology which is also found, along with polyhedral crystals, in hydrothermally synthesised Fe_3S_4 (Chang *et al.*, 2008).

Natural **chromite** in magmatic rocks shows octahedral morphologies with rounded edges or hollow prismatic crystals with octahedral terminations (Leblanc, 1980). $FeCr_2O_4$ synthesised using the chemical vapour transport method gives octahedral crystals (Ohgushi *et al.*, 2008).

Similarly, **daubréelite** synthesised via the chemical vapour transport method (Ohgushi *et al.*, 2008) or found in meteorites (Chikamii *et al.*, 1999) have octahedral morphologies. Those $FeCr_2S_4$ particles formed through the wet chemistry method tend to give spherical shapes (Mao and Lee, 2014).

For **$FeNi_2O_4$**, **violarite**, **$FeCo_2O_4$**, **$FeCo_2S_4$**, **$FeMn_2O_4$** and **$FeMn_2S_4$**, there are no studies of the crystal morphologies to the best of our knowledge.

1.4 Magnetic and electric properties of spinels

The magnetic properties in most of the (thio)spinels are based on the Néel's two sublattice model of ferrimagnetism (Néel, 1948). These sublattices are defined as the tetrahedral and octahedral positions while the model itself is based on the molecular field method. According to this model, the superexchange interaction between paramagnetic ions occupying different sublattices is negative and stronger than for those cations within any of the sublattices. These interactions lead to the so-called collinear Néel configuration, where the spins in tetrahedral and octahedral sublattices are aligned antiparallely and the total magnetization is the difference between the magnetizations of the two sublattices. Additionally, two other types of magnetic structures can exist in spinel compounds, *i.e.* the Yafet-Kittel triangular canting (Yafet and Kittel, 1952) and the spiral (Kaplan *et al.*, 1961) configurations. Unless otherwise stated, in the below description of the magnetic and electronic properties, all the (thio)spinels are Néel type ferrimagnets.

Magnetite is a ferrimagnetic material at ambient conditions and has a Néel temperature (T_N) of 850 K, the temperature at which it becomes paramagnetic. Fe_3O_4 is also half-metallic at ambient conditions due to an insulator band gap in the majority channel of the spins, which is associated with the tetrahedral sublattice (Zhang and Satpathy, 1991). Below the Verwey temperature (T_V = 122 K), together with the first-order phase transition, Fe_3O_4 becomes fully insulator (Verwey, 1939).

Greigite is also a ferrimagnetic half-metal with a Néel temperature reported for a very wide range going from ~300 to ~530 °C (Dekkers *et al.*, 2000).

Chromite, **daubréelite**, **$FeCo_2O_4$** and **$FeMn_2O_4$** are ferrimagnetic below the Néel temperature (T_N = 80 (Shirane *et al.*, 1964), 180 (Shirane *et al.*, 1964), 450 (Kawano *et al.*, 1976) and 383 K (Van Landuyt *et al.*, 1972) respectively). $FeCr_2O_4$ has also a spin rearrangement temperature (T_S = 35 K), below which the spins are no longer collinear and have a spiral structure (Shirane *et al.*, 1964). $FeMn_2O_4$ is semiconducting at least up to 900 K (Kulkarni and Darshane, 1985).

Magnetization measured in **$FeNi_2O_4$** (Shafer, 1962) and **$FeNi_2S_4$** (Vaughan and Craig, 1985) shows that these are paramagnetic compounds. As **$FeCo_2S_4$** and **$FeMn_2S_4$** do not occur naturally and have they been synthesised before, there is no experimental information about their magnetic or electronic properties.

1.5 Catalytic applications of Fe_3O_4

Magnetite is one of the principal types of iron oxides used as the main component of industrial heterogeneous catalysts because of its stability, availability and cost. Due to its electronic properties, Fe_3O_4 can catalyse both oxidation/reduction and acid/base reactions (Cornell and Schwertmann, 2003). For example, Fe_3O_4 is part of the catalysts used in processes such as the production of ammonia (NH_3) from H_2 and N_2 (the Haber-Bosch process) and the conversion of CO and H_2 into hydrocarbons (Fischer-Tropsch process). Fe_3O_4 also catalyses the water gas shift (WGS) reaction, which supplies H_2 to the Haber-Bosch and Fischer-Tropsch processes.

1.5.1 Haber-Bosch process for the production of ammonia

Ammonia is the primary feedstock for the production of fertilizers and nitric acid. More than 90 % of NH_3 is manufactured through the process described below which was developed by Fritz Haber and Carl Bosch between 1905 and 1910 (Topham, 1985). The reaction of formation of NH_3 from elemental hydrogen and nitrogen can be written as,

$$N_2 + 3H_2 \rightarrow 2NH_3 \tag{1.3}$$

As the reaction is exothermic $\left(\Delta H = -108.7 \text{kJ} \cdot \text{mol}^{-1}\right)$, the highest equilibrium yield is obtained at low temperatures and high pressures. However, the catalyst-free homogeneous gas phase equation (1.3) is hindered kinetically by the large activation energy (estimated between 230 – 420 $\text{kJ} \cdot \text{mol}^{-1}$ (Appl, 2012)). The largest contribution to the activation energy is due to the high stability of molecular N_2, which has a dissociation energy significantly larger than that of H_2.

Pure Fe-based heterogeneous catalysts reduce the activation energy of the rate determining step in the mechanism of NH_3 formation to 81.17 $\text{kJ} \cdot \text{mol}^{-1}$ (Spencer *et al.*, 1982). This step was initially suggested by experiments (Emmett and Brunauer, 1934; Scholten *et al.*, 1959) and later confirmed by microkinetic modelling (Aparicio and Dumesic, 1994) to be the N_2 adsorption and dissociation. Fe_3O_4 is the most suitable industrial catalyst for NH_3 production as portions of its surface can be reduced *in situ* by H_2 into the catalytically active α-Fe (Almquist and Crittenden, 1926), where the chemisorption of N_2 is neither too strong nor too weak (Aika *et al.*, 1973; Logan

and Kemball, 1960). The catalyst surface has an interconnected system of pores, which represent 44 – 46 % of the volume of the catalyst granule (Nielsen, 1981), where NH_3 formation takes place. Al_2O_3, the structural promoter and one of the additives of the catalyst, forms a solid solution with Fe_3O_4 (Dry and Ferreira, 1967; Garbassi *et al.*, 1972; Westrik, 1953), which favours α-Fe crystallites nucleation (Bogdandy *et al.*, 1963) (of high surface area) instead of their growth (Bare *et al.*, 1986). In the catalytically active (reduced) Fe_3O_4, the electronic promoter (K_2O, another additive of the catalyst) is atomically adsorbed and covers 20 – 50 % of the catalyst surface (Ertl, 1983), reducing its electron work function (Appl, 2012). This reduces the activation energy for the dissociative adsorption of N_2 and the adsorption energy of NH_3, which can desorb easily from the surface leaving it free to interact with more H_2 and N_2 molecules (Ertl, 1983). The activity of the catalyst is also enhanced by trace amounts of other additives, some of which are impurities in the original ore (Bond, 1974; Bridger and Snowden, 1970). During the manufacture of the catalyst, Fe_3O_4 together with the additives are melted electrically or in electric arc furnaces and the cooled melt is ground to the proper particle size (Appl, 2012).

1.5.2 Fischer-Tropsch synthesis

The Fischer-Tropsch process is named after Franz Fischer and Hans Tropsch, who developed it in 1926. This process is the best-known indirect coal liquefaction method where syngas (a mixture of CO and H_2) is transformed to a variety of useful products, such as substitute natural gas (SNG), gasoline, diesel oil, wax and alcohols (Kaneko

et al., 2012). The non-selective production of these products by the Fischer-Tropsch synthesis can be represented as follows:

$$n\mathrm{CO} + (2n+1)\mathrm{H_2} \rightarrow \mathrm{C}_n\mathrm{H}_{2n+2} + n\mathrm{H_2O} \quad (1.4)$$

$$n\mathrm{CO} + 2n\mathrm{H_2} \rightarrow \mathrm{C}_n\mathrm{H}_{2n} + n\mathrm{H_2O} \quad (1.5)$$

$$n\mathrm{CO} + 2n\mathrm{H_2} \rightarrow \mathrm{C}_n\mathrm{H}_{2n+1}\mathrm{OH} + (n-1)\mathrm{H_2O} \quad (1.6)$$

where *n* is an integer, equation (1.4) represents the reaction of formation of alkanes, equation (1.5) of alkenes and equation (1.6) of alcohols.

For the above reactions to take place, CO and H_2 molecules need to be activated by a heterogeneous catalyst's surface. There are three theories for the general mechanism of C−C bonds formation in these reactions. The first mechanism postulates that these bonds are formed via polymerization of -CH_2- fragments. The second pathway proposes that they are formed through the condensation of hydroxymethylene groups (−CHOH) with elimination of one H_2O molecule (Kummer and Emmett, 1953). The third scheme indicates that C−C bonds are formed through the insertion of CO into any of the metal-alkyl bonds (Henrici-Olive and Olive, 1976; Pichler and Schulz, 1970). Nevertheless, in any of these theories, the addition of hydrogen to the carbon intermediate has been suggested to be the rate-determining step (Huff and Satterfield, 1984).

Fe_3O_4 is one of the main components of the catalysts normally used for the Fischer-Tropsch synthesis. However, the working catalyst is only achievable once Fe_3O_4 is exposed to the syngas and is reduced to a mixture of α-Fe and iron carbide (χ-Fe_5C_2),

with high quantity of remnant Fe_3O_4 (Satterfield *et al.*, 1986). Cu and a SiO_2 support are additives of the catalyst that promote the reduction of Fe_3O_4 and avoid the sintering of the α-Fe phase respectively (Jin and Datye, 2000). Other additives, such as various alkali and alkaline earth metal oxides, increase the basicity of the Fe_3O_4 catalyst surface, which reduces the CH_4 selectivity during Fischer-Tropsch synthesis (Dry and Oosthuizen, 1968).

1.5.3 Water gas shift reaction

The water-gas shift (WGS) reaction is an important step in the production of H_2 for various industrial processes. This reaction is considered as a pre-step in the Fischer-Tropsch synthesis and therefore part of the indirect coal liquefaction process. Initially, coal is reacted with steam and O_2 to produce a mixture of CO and H_2 (syngas mixture). During the water-gas shift reaction, the ratio of H_2 to CO is adjusted to the requirements of the desired (Fischer-Tropsch) synthesis by means of the following equilibrium (Kaneko *et al.*, 2012):

$$CO+H_2O \rightleftharpoons H_2+CO_2 \tag{1.7}$$

The equilibrium of equation (1.7) is independent of pressure and is moderately exothermic $\left(\Delta H = -41.16\text{kJ}\cdot\text{mol}^{-1}\right)$. This limits the production of H_2 at high temperatures, the condition at which the reaction is kinetically favourable (Rhodes *et al.*, 1995). There are two mechanistic pathways proposed to explain how the water-gas shift reaction occurs: associative or regenerative (Armstrong and Hilditch, 1920). In the associative mechanism, CO and H_2O molecules are initially adsorbed onto the

catalyst to form an intermediate that decomposes into the H_2 and CO_2. The regenerative mechanism proposes that H_2O forms H_2 and oxidises the catalyst's surface, which is the rate-limiting step (Nakamura *et al.*, 1990). This step is followed by the regeneration of the initial state of the catalyst, which oxidises the CO to CO_2.

Fe_2O_3/Cr_2O_3 are the main components of the modern catalysts used for the high temperature water-gas shift reaction (310−450 °C), where the regenerative mechanism is believed to be the dominant pathway (Rethwisch and Dumesic, 1986). This initial process is followed by a low temperature step using a Cu-based catalyst in order to achieve low-levels output of CO (Rhodes *et al.*, 1995). In the Cu-based catalysts, there is still uncertainty on which is the dominant pathway taking place (Campbell and Daube, 1987; Koryabkina *et al.*, 2003; Liu and Rodriguez, 2007). We are not going to describe the low-temperature catalysts in this section, as these materials and processes are out of the scope of this thesis.

In the high temperature process, the catalyst becomes active after it is carefully reduced to Fe_3O_4 by the initial syngas mixture (Gonzalez *et al.*, 1986). α-Fe and iron carbides formed due to over-reduction of Fe_2O_3 are undesirable (Gonzalez *et al.*, 1986), as they are known to be catalysts of the Fischer-Tropsch process, where H_2 and CO are consumed (Kaneko *et al.*, 2012). The Fe^{2+}/Fe^{3+} pair occupying the octahedral positions in Fe_3O_4 acts as a redox couple to dissociate H_2O into H_2 and adsorbed oxygen (Rhodes *et al.*, 1995). Cr_2O_3 is a structural promoter, which avoids the thermal sintering of the Fe_3O_4 crystallites formed (Domka *et al.*, 1983) and keeps a high ratio of the surface area to the mass of the catalyst. Traces of Pb^{4+} salts increase the

covalency and electron transport capabilities of Fe_3O_4, which favours the H_2O reduction (Topsøe and Boudart, 1973).

1.5.4 Other applications of Fe_3O_4 and the (thio)spinels

Fe_3O_4 has a number of other applications, such as being part of materials for potentially remediating chromium-contaminated groundwater (dos Santos Coelho *et al.*, 2008). A Fe/Fe_3O_4 composite is the reactive reductant material where surface Fe_B^{2+} from Fe_3O_4 plays an important role in the reaction. As the reduction takes place, metallic Fe transfers an electron to Fe_3O_4 to reduce Fe_B^{3+} and regenerate the active ion. This reactive composite could also be used together with H_2O_2 for the oxidation of organic contaminants via an heterogeneous Fenton process (Costa *et al.*, 2008; Moura *et al.*, 2006).

Nanosized Fe_3O_4 particles are another promising component of anode materials with excellent cycling and rate performance for the next generation of high-performance lithium-ion batteries. Amongst the different construction proposals are highly dispersed and superparamagnetic Fe_3O_4 nanoparticles encapsulated by a carbon matrix forming a homogeneous Fe_3O_4@C composite (Cui *et al.*, 2009); superparamagnetic (Zhang and Zhang, 2009) Fe_3O_4 nanowires carbon coated (Muraliganth *et al.*, 2009) and Cu nanorods covered by a plating of Fe_3O_4 (Taberna *et al.*, 2006).

Fe_3O_4 nanoparticles can also have possible application as part of anticancer drug therapies. Fe_3O_4 magnetic nanoparticles enclosed by human serum albumin can act as drug carriers that can be magnetically guided to the target area and have sustained-

release properties due to the slow decomposition of the albumin (Lin *et al.*, 2007). Fe_3O_4 nanoparticles capped with tetraheptylammonium can be magnetically oriented to leukemia cells and improve the uptake of the antitumoral drug daunorubicin by them. The nanoparticle binds competitively to a glycoprotein of the membrane of the cell, inhibiting it and synergistically allowing drug accumulation within the cell (Wang *et al.*, 2007).

Fe_3O_4 magnetic nanoparticles have a further application as one of the components of highly sensitive and selective analytical sensors. These nanoparticles can act as peroxidase mimetics that catalyse the oxidation of a substrate with H_2O_2 (Wei and Wang, 2008; Zhu and Diao, 2011) or glucose (Wei and Wang, 2008) to give a coloured product and provide a colorimetric detection of these molecules. These types of catalytic properties of Fe_3O_4 can also offer other great potential applications as biosensors in the future.

The structural analogy between Fe_3S_4 and $FeNi_2S_4$ with certain contemporary enzymes cofactors in the form of (Fe,Ni)S clusters (Russell and Martin, 2004) has led to proposals that these minerals could have played an important catalytic role in the primordial metabolism (Huber and Wächtershäuser, 1997). The iron-sulfur membrane theory, as this origin of life theory is known (Russell and Hall, 1997), suggests that initially FeS and NiS membranes precipitated due to specific pH and ionic conditions near the ocean floor *circa* 4 billion years ago (Russell and Martin, 2004). The first organic molecules were then formed after the reduction of CO_2 catalysed by the oxidation of Fe^{2+} ions probably through a mechanism similar to the modern-day

acetyl-coenzyme A pathway (Ferry, 1995; Huber and Wächtershäuser, 1997; Russell and Martin, 2004). Bio-inspired by this theory, the catalytic properties of Fe_3S_4 and $FeNi_2S_4$ towards carbon-activation could lead to economically viable applications to convert industrially produced CO_2 into fine chemicals and mitigate the consequences of climate change.

1.6 Objectives of the thesis

A literature review about the occurrences as well as structural, magnetic, electric and catalytic properties of FeM_2X_4 (thio)spinels shows the importance of this group of compounds. However, more work is needed to increase the understanding of these properties. In this thesis, we have employed computational modelling tools, which are summarized in Chapter 2, with the aim to study a number of bulk and surface properties of FeM_2X_4. Chapter 3 provides details of the calculated equilibrium inversion degree and electronic structure of FeM_2X_4. Chapter 4 and 5 present the calculated mechanical properties as well as the structure, stabilities and redox behaviour of the major surfaces of Fe_3O_4 respectively. Chapter 6 gives a theoretical insight into the initial oxidation of $Fe_3S_4(001)$ surface induced by H_2O. The results presented in these chapters will help to gain a deeper understanding of the surface chemistry and bulk properties of FeM_2X_4 and will contribute to our general knowledge of the catalytic and electronic applications of these group of materials.

2

Methods for materials modelling

2.1 Introduction

In this chapter we review the methods, models and tools for materials modelling that have been used to carry out the research presented in this thesis. We have chosen to use *ab initio* quantum chemistry methods and in particular the density functional theory (DFT) approximation, as it provides details of the electronic structure of the systems under consideration. Within this framework, we have used throughout this thesis the Vienna *Ab-initio* Simulation Package (VASP) (Kresse and Furthmüller, 1996a, 1996b; Kresse and Hafner, 1994, 1993).

We present the time-independent nonrelativistic Schrödinger equation and the indispensable Born-Oppenheimer approximation in order to describe the motion of many electrons in a field of static nuclei. We also introduce the Hartree-Fock method for solving multi-electronic systems. We discuss a different approach: the Hohenberg-Kohn theorems of the density functional theory and how they became applicable through the Kohn-Sham equations as well as two levels of approximation of this theory. We describe two alternatives to improve the exchange term, namely *via* a Hubbard Hamiltonian method or hybrid functionals. We are also concerned with the simplification of the number of electrons to consider in the simulations of periodic

solids and atoms through plane-wave basis sets and pseudopotentials respectively. We present a methodology to improve the description of the long range dispersion interactions. We discuss how the geometry optimization is carried out and how work the different methods for searching them. Finally, we introduce different techniques for the characterization of the optimized geometries, such as vibrational frequencies, density of states and Bader analysis of the charges.

2.2 The Schrödinger equation

Electronic structure methods are based on the explicit consideration of the *M* nuclei and *N* electrons forming a chemical system. The problem of the interaction of these *M* + *N* particles can be described using the non-relativistic time-independent Schrödinger equation:

$$E\Psi = \left[-\sum_{i=1}^{N} \frac{1}{2} \nabla_i^2 - \sum_{A=1}^{M} \frac{1}{2M_A} \nabla_A^2 - \sum_{i=1}^{N} \sum_{A=1}^{M} \frac{Z_A}{r_{iA}} + \sum_{i=1}^{N-1} \sum_{j>i}^{N} \frac{1}{r_{ij}} + \sum_{A=1}^{M-1} \sum_{B>A}^{M} \frac{Z_A Z_B}{R_{AB}} \right] \Psi \quad (2.1)$$

The above expression is given in atomic units, where *E* represents the energy and Ψ is the wavefunction. r_{iA}, r_{ij} and R_{AB} are the *i*th electron - *A*th nucleus, *i*th - *j*th electrons as well as *A*th - *B*th nuclei distances, respectively. Z_A is the atomic number of nucleus *A* and M_A represents the ratio of its mass to the mass of an electron. The Laplace operator (∇) represents the second derivative with respect to the spatial coordinates of the nucleus or electron. The terms within the operator in the right hand side of the equation (2.1) represent, in this order, the kinetic energy of the electrons; the kinetic

energy of the nuclei; the coulomb attraction between electrons and nuclei; the coulomb repulsion between electrons and the coulomb repulsion between nuclei, respectively.

By solving equation (2.1), it is possible to obtain all the physical-chemical properties (except for the relativistic effects) of the system under study. However, equation (2.1) has the problem of two sets of related variables: electrons and nuclei.

A simplification to the above problem is based on the fact that the mass of an electron is approximately 1830 times smaller than the mass of a proton, for which it is possible to assume that electrons move much faster than nuclei. The Born-Oppenheimer approximation (Born and Oppenheimer, 1927) simplifies the Schrödinger equation by separating electronic and nuclear coordinates in the many-body wavefunction by neglecting the kinetic energy of the nuclei and considering the nuclei repulsion to be constant. The simplified equation describes the motion of electrons in an arrangement of static nuclei:

$$E\Psi = \left[-\sum_{i=1}^{N} \frac{1}{2} \nabla_i^2 - \sum_{i=1}^{N} \sum_{A=1}^{M} \frac{Z_A}{r_{iA}} + \sum_{i=1}^{N-1} \sum_{j>i}^{N} \frac{1}{r_{ij}} \right] \Psi \tag{2.2}$$

The Schrödinger equation in the above form only has an exact solution for hydrogen-like atoms (those composed of a nucleus of any size and a single electron) and additional simplifications are required for multi-electronic or poly-atomic systems.

For systems with more than one electron, the coulomb repulsion between electrons is difficult to evaluate and other approximations are required. Among the earlier approximations of the Schrödinger equation were those aimed to reduce the electronic interaction to one-electron problem. This is the foundation of the Hartree-Fock (HF)

method, which considers every electron interacting with a mean-field of all the other electrons. The HF method has the disadvantage that it only correlates the motion of electrons with parallel spins, which makes the total energy given by the HF method to differ by the correlation energy from the exact total energy. Although some refinements have been developed (the so-called post-HF methods) to improve the difference of energies, the density functional theory (DFT) method is the one usually preferred in the context of solid state modelling.

2.3 Density functional theory

2.3.1 The Hohenberg-Kohn theorems

A fresh approach for bypassing the many-body problem of the Schrödinger equation was proposed by Hohenberg and Kohn (1964). They showed that the electronic density $\rho(\mathbf{r})$ of the ground state of the system uniquely determines the Hamiltonian and therefore all the properties of a physical system, such as the total external potential acting on the electrons $V(\mathbf{r})$.

They also proved that a functional $F[\rho(\mathbf{r})]$ is needed to calculate the energy $E[\rho(\mathbf{r})]$ of an electronic system. Therefore, combining the two previous theorems, it is possible to express $E[\rho(\mathbf{r})]$ as:

$$E[\rho(\mathbf{r})] = \int V(\mathbf{r})\rho(\mathbf{r})d\mathbf{r} + F[\rho(\mathbf{r})] \tag{2.3}$$

where $V(\mathbf{r})$, for atomic systems, is the coulomb attraction between nuclei and electrons and $F[\rho(\mathbf{r})]$ contains the kinetic energy as well as inter-electronic coulomb repulsion, exchange and correlation energies.

The variational principle is used to minimize the value of $E[\rho(\mathbf{r})]$ in order to obtain the ground state energy of the real system, the exact $\rho(\mathbf{r})$ and the rest of its properties. Despite all of the above demonstrations, the new approach still faced the difficulty of solving the electron-electron term in the Hamiltonian, see equation (2.2).

2.3.2 Kohn-Sham equations

Kohn and Sham (1965) refined the early density functional theory by stating that a fictitious system of non-interacting electrons has the same density as the real system of interacting electrons, whose energy can be separated into the following terms:

$$E[\rho(\mathbf{r})] = T_{ni}[\rho(\mathbf{r})] + V_{ne}[\rho(\mathbf{r})] + V_{ee}[\rho(\mathbf{r})] + E_{xc}[\rho(\mathbf{r})] \qquad (2.4)$$

where $T_{ni}[\rho(\mathbf{r})]$ represents the kinetic energy of the non-interacting electrons, $V_{ne}[\rho(\mathbf{r})]$ represents the nuclei-electron interaction, $V_{ee}[\rho(\mathbf{r})]$ represents the inter-electronic repulsion and $E_{xc}[\rho(\mathbf{r})]$ represents the exchange-correlation energy. The last term is a correction to the kinetic energy and the non-classical inter-electronic repulsion due to exchange and correlation.

In order to minimize the energy $E[\rho(\mathbf{r})]$, it is convenient to express it as a function of one-electron orbitals ψ_i, as:

$$E\left[\rho(\mathbf{r})\right] = \sum_{i=1}^{N}\left\langle \psi_i \left| -\frac{1}{2}\nabla^2 - \sum_{A=1}^{M}\frac{Z_A}{\left|\mathbf{r}-\mathbf{R}_A\right|} + \frac{1}{2}\int\frac{\rho(\mathbf{r}')}{\left|\mathbf{r}-\mathbf{r}'\right|}d\mathbf{r}' \right| \psi_i \right\rangle + E_{xc}\left[\rho(\mathbf{r})\right] \quad (2.5)$$

where

$$\rho(\mathbf{r}) = \sum_{i=1}^{N}\left|\psi_i\right|^2 \quad (2.6)$$

The problem of finding the one-electron orbitals that minimize the equation of energy is then solved via the Kohn-Sham equation:

$$\hat{h}^{KS}\psi_i = \left[-\frac{1}{2}\nabla^2 - \sum_{A=1}^{M}\frac{Z_A}{\left|\mathbf{r}-\mathbf{R}_A\right|} + \frac{1}{2}\int\frac{\rho(\mathbf{r}')}{\left|\mathbf{r}-\mathbf{r}'\right|}d\mathbf{r}' + V_{xc}(\mathbf{r}) \right]\psi_i = \varepsilon_i^{KS}\psi_i \quad (2.7)$$

where the functional derivative $V_{xc}(\mathbf{r})$ is equal to $\delta E_{xc}\left[\rho(\mathbf{r})\right]/\delta\rho(\mathbf{r})$.

The Kohn-Sham equation is then solved self-consistently, which means that a model density is given to the equation (2.4) to obtain an energy that is used to solve equation (2.7) and find the new density $\rho(\mathbf{r})$ from equation (2.6).

However, the form of $E_{xc}\left[\rho(\mathbf{r})\right]$ is important in DFT and two approximations for its calculation are discussed in the next section.

2.3.3 Exchange-correlation functionals: LDA and GGA

In this section, we discuss two levels of approximation for the calculation of the exchange-correlation energy, namely the local density approximation (LDA) and the generalized gradient approximation (GGA).

In the LDA (or LSDA, after Local Spin Density Approximation, for spin polarized systems) approximation, the exchange-correlation energy is calculated as:

$$E_{xc}^{LDA} = \int d^3\mathbf{r}\rho(\mathbf{r})\varepsilon_{xc}^{LDA} \tag{2.8}$$

where ε_{xc}^{LDA} is the exchange-correlation energy per particle of a uniform electron gas (jellium). The Vosko, Wilk and Nusair (VWN) functional, one of the most common of this type, was developed by fitting the results from Quantum Monte Carlo Calculations (Ceperley and Alder, 1980) to mathematical expressions (Perdew and Zunger, 1981; Vosko *et al.*, 1980). The LDA is a good approximation for systems where the density varies slowly or moderately over space, like metals.

A more elaborated approach to calculate the exchange-correlation energy is by considering the variation of the electronic density in the vicinity of the integration point and not only its value in such a point, as in LDA. By making ε_{xc} depend additionally on the gradients of the electronic density $\nabla\rho(\mathbf{r})$, it is possible to introduce non-local effects on the functional, which leads to the generalized gradient approximation (GGA):

$$E_{xc}^{GGA} = \int d^3\mathbf{r}\left(\rho(\mathbf{r}), \nabla\rho(\mathbf{r})\right) \tag{2.9}$$

There are several implementations of GGA functionals and all of them describe more accurately the system under investigation than LDA functionals. Popular GGA exchange-correlation functionals include the one developed by Perdew and Wang (PW91) (Perdew *et al.*, 1993, 1992) which was constructed using data from LDA, improving the results of pure local approximation methods (Burke *et al.*, 1998, 1995;

Hammer *et al.*, 1993; Stixrude *et al.*, 1994). Another example is the Perdew, Burke and Ernzerhof (PBE) (Perdew *et al.*, 1997, 1996a) and its revision for solids PBEsol (Perdew *et al.*, 2008). In this thesis we have used the PW91 functional in Chapters 4 and 6, PBE functional in Chapter 5 and PBEsol functional in Chapter 3. For example, the optimized lattice parameter of Fe_3O_4 obtained using the PW91 functional (8.390 Å) reproduces in very good agreement the experimental one (8.390 Å), while PBE overstimates it slightly (8.398 Å) and PBEsol understimates it (8.345 Å). Note that the above results were obtained including the corrections described in the following sections that affect the performance of pure GGA functionals.

2.4 DFT + *U* method

The electronic self-interaction is another shortcoming associated with most of the DFT methods. It arises when the correlation term is not treated exactly and produces artificially delocalized electron densities. In materials with strongly interacting and very localized electrons, such as in many transition metal oxides, the DFT method is unable to reproduce a realistic electronic structure, as it fails to open the band gap (Leung *et al.*, 1991; Terakura *et al.*, 1984) or underestimates it (Sawatzky and Allen, 1984; Zaanen *et al.*, 1985). This DFT limitation is not only exclusive to transition metal oxides, but is also found in rare earth compounds and some non-metal oxides (Pacchioni, 2001).

The incorporation of a Hubbard Hamiltonian (Hubbard, 1963) is one of the solutions used to overcome the electron self-interaction in DFT, which is known as DFT + *U*

(Anisimov *et al.*, 1991). The added U parameter enhances the on-site Coulomb repulsion between electrons in the same *d*-bands by penalizing the double occupation of these bands. This can be seen as an increment in energy associated with the introduction of an electron in certain *d*-orbitals, *i.e.* $U = E\left(d^{n+1}\right) + E\left(d^{n-1}\right) - 2E\left(d\right)$, which opens band gaps close to the experimental ones or those obtained from more demanding computational methods.

There are two types of DFT + U methods and in this thesis we have used the Hamiltonian in the version proposed by Dudarev *et al.* (1998) which takes the form:

$$E_{DFT+U} = E_{DFT} + \frac{U_{\text{eff}}}{2}\sum_{\sigma}\left[\rho^{\sigma} - \rho^{\sigma}\rho^{\sigma}\right] \tag{2.10}$$

where ρ^{σ} is the on-site density matrix of the *d*-electrons with spin σ and U_{eff} is equal to the difference between U, the spherically averaged Hubbard parameter, and J, the screened exchange energy.

The DFT + U method only makes physical sense when U_{eff} and $\left[\rho^{\sigma} - \rho^{\sigma}\rho^{\sigma}\right]$ are both bigger than 0. The latter can be shown easily in the idempotency limit of ρ^{σ}. This means that the eigenvalue of this matrix is either 0 to 1, which are values associated with fully unoccupied or occupied *d*-levels. The net result is a DFT + U energy which is always bigger than the pure DFT energy.

The DFT + U method can be applied to both local and gradient corrected functionals. However, better results are typically obtained with GGA while different U values are usually required for each type of functional to obtain comparable results (Rohrbach *et*

al., 2003). The method also affects geometrical factors indirectly after the variation of electronic properties (Rohrbach *et al.*, 2003; Rollmann *et al.*, 2004). In this thesis, the U_{eff} values used to describe adequately the *d* bands of each transition metal ion were dependant of the functional used. The optimal U_{eff} values were determined by fitting the calculated band gap to the experimental one, where this information was available, or the calculated positions of the *d* band centres to those obtained from using hybrid functionals, a more demanding calculation method described in the following section.

2.5 Hybrid functionals

Another solution used to improve the description of the exchange term in DFT calculations is based on the partial ($0 < a < 1$) incorporation of an exact exchange part from HF in hybrid functionals:

$$E_{xc} = (1-a) E_x^{DFT} + aE_x^{HF} + aE_c^{HF} \tag{2.11}$$

The incorporation of the non-local HF exchange part also provides some degree of self-interaction cancellation, as this term and the classical Coulomb interaction have opposite signs. The use of only the exact HF exchange, $a = 1$ in equation (2.11), worsen the hybrid functional results as there is an important error cancellation element taking place between the DFT exchange and correlation functionals (Ivanov *et al.*, 1999).

In Chapter 3 of this thesis we have used the Heyd-Scuseria-Ernzerhof (HSE) functional (Heyd *et al.*, 2006, 2003) which includes 25% of the HF exchange and is one of the most widely used functionals in solid state modelling.

2.6 The electronic problem in periodic solids

So far, we have seen how several methods are able to break down the multi-electronic problem into accurate one-electron expressions. However, for crystalline solids, symmetry elements can also be taken into account to reduce the number of atoms, and therefore electrons, considered in the simulation of those in the unit cell. In this section we analyse how plane-wave basis sets are able to handle this simplification.

2.6.1 Bloch's theorem

The wavefunction of a free electron is described by a plane wave $\psi \sim e^{i\mathbf{k}\cdot\mathbf{r}}$ where the points with constant value form a plane perpendicular to the vector $\mathbf{k}$. Another property of the wavefunction of one electron $\psi_{i,\mathbf{k}}(\mathbf{r})$ moving in a periodic potential is its similarity to the one of a free electron $e^{i\mathbf{k}\cdot\mathbf{r}}$ only modulated by the function $f_{i,\mathbf{k}}(\mathbf{r})$ (Bloch, 1929):

$$\psi_{i,\mathbf{k}}(\mathbf{r}) = f_{i,\mathbf{k}}(\mathbf{r}) e^{i\mathbf{k}\cdot\mathbf{r}} \tag{2.12}$$

The function $f_{i,\mathbf{k}}(\mathbf{r})$ also has the same periodic character as the crystal. This means that $f_{i,\mathbf{k}}(\mathbf{r})$ has the same value when the input argument is $\mathbf{r}$ or any translational vector $\mathbf{T}$ with the same periodicity of the crystal.

The expansion of $f_{i,\mathbf{k}}(\mathbf{r})$ as a Fourier series of the vectors $\mathbf{G}$ in the reciprocal lattice:

$$f_{i,\mathbf{k}}(\mathbf{r}) = \sum_{\mathbf{G}} c_{i,\mathbf{k},\mathbf{G}} e^{i\mathbf{G}\cdot\mathbf{r}} \tag{2.13}$$

where the vectors $\mathbf{G}$ are defined by the expression $e^{i\mathbf{G}\cdot\mathbf{T}} = 1$.

From the above equations, it is easy to see that solutions for wavefunctions with index $\mathbf{k}+\mathbf{G}$ are identical to those with index $\mathbf{k}$. Therefore, it is enough to find solutions only for the values of $\mathbf{k}$ -points in the first Brillouin zone, which is the primitive cell in reciprocal space.

There are several methods aimed at providing good choices of $\mathbf{k}$ -points such as the improved tetrahedron method (Blöchl *et al.*, 1994) which breaks up the cell in the reciprocal space into tetrahedra as well as the Monkhorst and Pack method (Monkhorst and Pack, 1976), that generates a set of special points in the Brillouin zone.

2.6.2 Plane-wave expansion of the wavefunctions

Each wavefunction can also be expressed as an expansion in a basis set of planes waves by substituting equation (2.13) in (2.12):

$$\psi_{i,\mathbf{k}}(\mathbf{r}) = \sum_{\mathbf{G}} c_{i,\mathbf{k}+\mathbf{G}} e^{i(\mathbf{k}+\mathbf{G})\cdot\mathbf{r}} \tag{2.14}$$

The electronic wavefunction is only described exactly by an infinite plane-wave basis set. However, in practice, as the $c_{i,\mathbf{k}+\mathbf{G}}$ coefficients tend to zero for plane-waves of high kinetic energy, it is truncated to include only those plane waves with kinetic energy $(\hbar/2m)|\mathbf{k}+\mathbf{G}|^2$ below certain cut-off.

Since the wavefunction $\psi_{i,\mathbf{k}}(\mathbf{r})$ depends on the plane wave coefficients $c_{i,\mathbf{k}+\mathbf{G}}$, the problem of solving the Kohn-Sham equation is reduced to find the set of $c_{i,\mathbf{k}+\mathbf{G}}$ that minimizes the energy.

Although the size of the wavefunction is determined by the cut-off of the kinetic energy of the plane waves, it is still large for systems that comprise both the core and valence electrons. In the next section, we are going to analyse the pseudopotential approximation that reduces this problem by considering explicitly only the valence electrons of the system.

2.7 Pseudopotentials

The pseudopotential theory also aims to reduce the complexity of the calculations. It works by replacing the Coulomb potential of the core electrons and nucleus with a potential acting on the valence electrons, based on the low chemical reactivity of the core electrons.

One of the most common forms are the norm-conserving pseudopotentials (NCPP) which were developed from atomic calculations. This type of pseudopotential can then be subsequently used in calculations where those atoms are also combined forming compounds.

In the core region of any atom, the core wavefunctions oscillate rapidly due to the strong Coulomb potential. However, under the NCPP methodology, this part of the

wavefunction is replaced by a soft nodeless pseudo-wavefunction with the same charge as the all-electron wavefunction within this region (Hamann *et al.*, 1979).

There are several variations of this approach, like the ultrasoft pseudopotentials (USPP). In the USPP methodology, the charge of the core electrons is allowed to change, whose variation is compensated with the introduction of localized atom-centred augmentation charges (Vanderbilt, 1990).

2.7.1 The projector augmented-wave method

The most robust of the pseudopotential methods developed so far is the projector augmented-wave (PAW) method (Blöchl, 1994), which borrows ideas from the all-electron linear augmented plane-wave (LAPW) method (Andersen, 1975).

In the PAW approximation, the wavefunction can be expressed as:

$$\psi(\mathbf{r}) = \tilde{\psi}(\mathbf{r}) + \sum_{\Lambda} \left[\phi_{\Lambda}(\mathbf{r}) - \tilde{\phi}_{\Lambda}(\mathbf{r}) \right] \left\langle \tilde{p}_{\Lambda} \middle| \tilde{\psi} \right\rangle \tag{2.15}$$

where $|\psi\rangle$ and $|\tilde{\psi}\rangle$ are the wavefunction and pseudo-wavefunction respectively, $|\phi_{\Lambda}\rangle$ and $|\tilde{\phi}_{\Lambda}\rangle$ are the one-electron Schrödinger equations for the isolated atom (partial waves) and auxiliary pseudo partial waves respectively and $\tilde{p}_{\Lambda}$ are the projector functions.

In this formalism, $|\psi\rangle$ behaves like an atom within the atomic (augmentation) regions and outside (interstitial regions), it is identical to $|\tilde{\psi}\rangle$. The basis set in the augmentation region is formed by the solutions of $|\phi_{\Lambda}\rangle$, which have a nodal behaviour.

Within the augmentation regions, $|\tilde{\psi}\rangle$ is cancelled out by the expansion of $|\tilde{\phi}_\Lambda\rangle$ that is chosen in such a way that equals $|\phi_\Lambda\rangle$ in the interstitial regions.

Although equation (2.15) is exact for a complete expansion of $|\phi_\Lambda\rangle$, this term is in practice truncated, which contributes to its fast convergence. This also leads to some contribution of $|\tilde{\psi}\rangle$ in the augmentation regions.

In this method, while core electrons are considered frozen at the atomic solutions, the full all-electron wavefunction is used, which enables the calculation of properties that depend on the full charge and spin density, such as hyperfine parameters (Cottenier *et al.*, 2005). Moreover, the convergence of $|\tilde{\psi}\rangle$ is faster in PAW than in NCPP and USPP due to the truncation of $|\phi_\Lambda\rangle$.

We have used the PAW method in the result chapters of this thesis in the implementation in VASP by Kresse and Joubert (1999).

2.8 Dispersion interaction correction methods

Another limitation of any implementation of pure DFT is its lack of a proper way to describe long-range dispersion interactions. Due to the local character of its functionals, the method fails to correlate the electronic movement of remote atoms (Ruzsinszky *et al.*, 2005). The most common form to overcome this restriction is to

add a correction $\left(E_{\text{vdW}}\right)$ within certain cutoff to the conventional Kohn-Sham DFT energy $\left(E_{\text{KS-DFT}}\right)$:

$$E_{\text{DFT-vdW}} = E_{\text{KS-DFT}} + E_{\text{vdW}} \tag{2.16}$$

The correction term $\left(E_{\text{vdW}}\right)$ can be calculated using a dispersion interaction method. Among these, one of the most robusts is the D2 method of Grimme (2006), which has been proved to provide better structural and mechanical energies predictions in crystals of different nature in comparison to standard DFT functionals, at low computational costs (Bučko *et al.*, 2010) and is the one used in this thesis. According to the D2 method, the E_{vdW} contribution is expressed as:

$$E_{\text{vdW}} = -\frac{s_6}{2}\sum_{A=1}^{M}\sum_{B=1}^{M}\sum_{L}\frac{C_{6AB}}{R_{AB,L}^6} f_{d,6}\left(R_{AB,L}\right) \tag{2.17}$$

where the sums are over the total number of atoms M, C_{6AB} is the dispersion coefficient for the atom pair AB, $R_{AB,L}$ represents the distance between atom A located in the reference cell and atom B in the translation of the unit cell L and s_6 is a global scaling parameter that has been optimized for different DFT functionals. $f_{d,6}$ is a Fermi-type damping function introduced to minimize contributions from interactions within typical bond distances calculated as:

$$f_{d,6}\left(R_{AB,L}\right) = \frac{1}{1+e^{-d\left(R_{AB}/R_{\text{vdW-}AB}-1\right)}} \tag{2.18}$$

where d is the damping parameter.

The dispersion coefficient C_{6AB} is calculated using the geometric mean of the atomic C_{6A} and C_{6B} parameters. $R_{\text{vdW-}AB}$ is the sum of the atomic van der Waals radii of the atoms *A* and *B* and together with the atomic C_{6A} have been tabulated for each element and have been determined in a rather non-sensitive way to the chemical environment.

The D2 method has been subject of variations, such as the D3 method of Grimme *et al.* (2010), the D3 (zero) damping method (Grimme *et al.*, 2011), the Tkatchenko-Scheffler (TS) method (Tkatchenko and Scheffler, 2009), the TS + SCS self-consistent screening method (Tkatchenko *et al.*, 2012). However, D3 and D3(zero) method add a higher level of complexity to the expressions and TS as well as TS + SCS make strongly ionic systems to outperform (Bučko *et al.*, 2013).

2.9 Geometry optimizations

In this section, we comment on the optimization of atomic positions and cell parameters. These procedures are based not only on finding the minimum of the electronic energy but also of the inter-nuclear Coulomb energies (total energy, by combining both) at 0 K, see **Figure 2.1**.

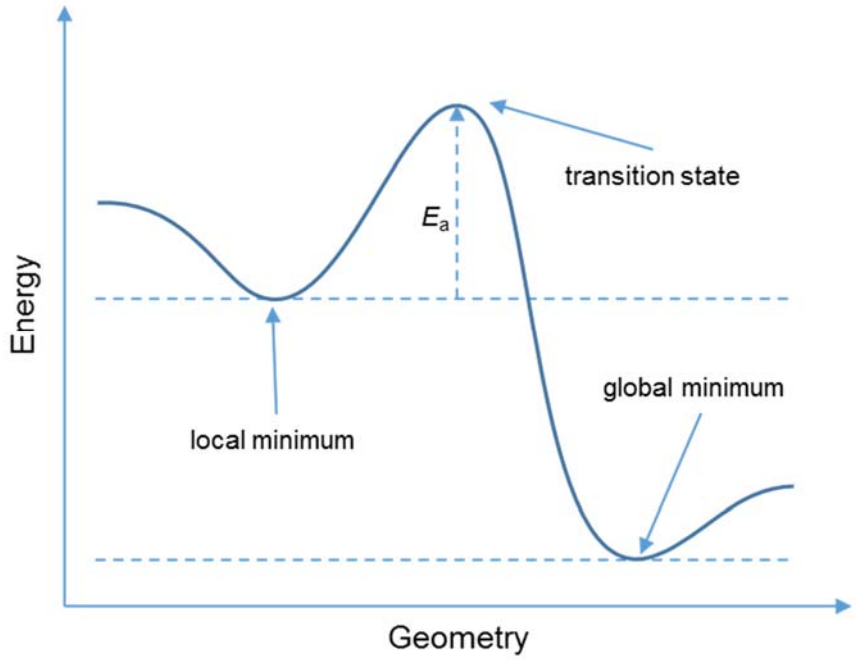

Figure 2.1. Profile representation of a local and global minima separated by a transition state, where E_a is the activation energy.

2.9.1 Optimisation of ionic positions: the conjugate gradients method

The conjugate gradients (CG) is one among the various algorithms (Gill *et al.*, 1981) developed to find the minimum of a function of several variables. In the context of an ionic system, this method works by calculating the energy function $E(\mathbf{R})$ and its gradient with respect to the ion's (nuclei) coordinates $\mathbf{R}$. As $-\partial E(\mathbf{R})/\partial \mathbf{R}$ is, by definition, the force $\mathbf{F}$ on the ions, its calculation is reduced to solve the Hellmann-Feynman theorem for a given system.

The CG method is based on the steepest descent (SD) algorithm, where atoms are moved in the direction of $\mathbf{F}$, see **Figure 2.2 (a)**. In the SD technique, the evaluation

of $E(\mathbf{R})$ is first carried out along a line at regular intervals between two points. For a given initial position $\mathbf{R}_1$, the new position will be:

$$\mathbf{R}_2 = \mathbf{R}_1 + b_1\mathbf{F}(\mathbf{R}_1) \tag{2.19}$$

where b_1 is chosen to make $\mathbf{F}(\mathbf{R}_2)\cdot\mathbf{F}(\mathbf{R}_1)$ equal to zero.

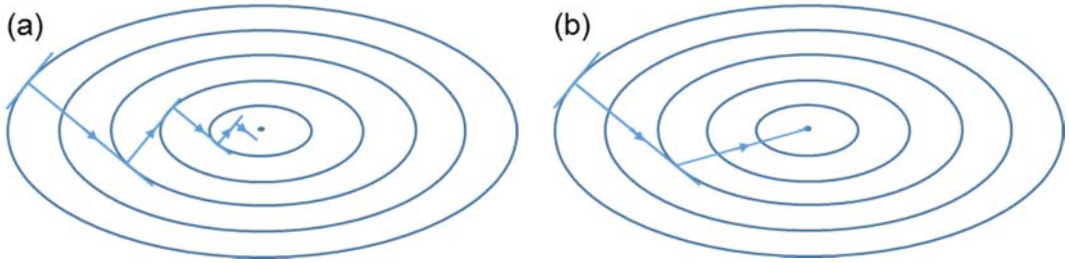

Figure 2.2. Schematic illustration of (a) the steepest descent (SD) and (b) the conjugate gradients (CG) algorithms.

The new gradient $\mathbf{F}(\mathbf{R}_2)$ is perpendicular to the previous line and the procedure is repeated from the new point to the direction of $\mathbf{F}(\mathbf{R}_2)$ until the minimum is located.

The SD method has the disadvantage of only allowing perpendicularly related directions in searching for a minimum. This causes the SD algorithm to require, in some cases, a large number of iterations to converge.

Although the first step of the CG and SD techniques is the same, in the CG method, the direction of successive displacements is allowed to take any direction, which can be expressed as:

$$\mathbf{R}_{m+1} = \mathbf{R}_m + b_m\mathbf{S}_m \tag{2.20}$$

Now the search vector $\mathbf{S}_m$ contains information from the gradient and the search direction from the previous step:

$$\mathbf{S}_m = \mathbf{F}(\mathbf{R}_m) + \gamma_m \mathbf{S}_{m-1} \tag{2.21}$$

where the scalar coefficient γ_m is zero for $m = 1$ and for the successive steps it is defined by Fletcher and Reeves (1964) as:

$$\gamma_m = \frac{\mathbf{F}(\mathbf{R}_m) \cdot \mathbf{F}(\mathbf{R}_m)}{\mathbf{F}(\mathbf{R}_{m-1}) \cdot \mathbf{F}(\mathbf{R}_{m-1})} \tag{2.22}$$

The main advantage of the CG with respect to the SD method is that it reduces considerably the number of iterations (search steps) needed to locate the minimum of the energy function. In the CG algorithm, search directions are optimally independent (*conjugate*) from each other, which allows for a quadratic function of *M* variables to find the minimum in *M* steps, see **Figure 2.2 (b)**.

In the VASP code, after the initial SD iteration, the subsequent line minimization of the CG method has been programmed in several steps: i) a trial step into the search direction (scaled gradients) is carried out, where the energy and forces are recalculated. ii) From the change of the energy and forces calculated in the previous step, the total energy is cubically (or quadratically) interpolated and its approximate minimum is calculated, to where the corrector step is performed. iii) After the corrector step, the forces and energy are recalculated and VASP checks whether there is a significant component of the forces parallel to the previous search direction. If this is the case, the line minimization is improved by further corrector steps.

In the above explanation, we have assumed that the energy function has a single minimum. In the case that it has several minima, the method described will locate the minimum in whose basin the initial sampling point lies.

2.9.2 Relaxation of cell parameters: Pulay stress and equation of state method

If not only the atoms' positions but also the cell parameters are being optimized, then the "Pulay stress" may arise (Francis and Payne, 1990).

The reason for this error is that plane wave basis set is not complete with respect to changes of the volume. It means that the energy cut-off and size of the reciprocal lattice cell determine the number of basis functions. The variation of the volume of the crystal cell, due to the optimization of the lattice parameter, will change the number of plane waves in the basis set for the same energy cut-off. The effect of this error is equivalent to a pressure bigger than 0, or stress which tends to decrease the volume.

Usually, setting an energy cut-off ~30% higher than that required for energy convergence is enough for achieving the stress tensor convergence. The higher cut-off has, however, the disadvantage of making the calculations more computationally demanding.

An alternative method to avoid the Pulay stress is to carry out volume conserving relaxations, where only ion coordinates and cell shape are allowed to relax. Therefore, the basis set is constant and this type of relaxation does not have the same problems, as the Pulay stress depends mainly on the volume. The resulting energy *versus* volume points are fitted to a cubic equation of state, whose minimum gives the equilibrium volume of the cell.

2.9.3 Transition states

The transition state is at the top of the lowest energy path (saddle point) between two stable configurations and it defines the reaction coordinate for transitions such as chemical reactions or diffusion processes, see **Figure 2.1**. Finding this point also allows the estimation of the activation energy barrier required for this process to happen.

Among the different methods developed to find saddle points (Henkelman *et al.*, 2002), in this thesis we have used a combination of two: the climbing image nudged elastic band (cNEB) method (Henkelman *et al.*, 2000; Sheppard *et al.*, 2008) and the improved dimer method (IDM) (Heyden *et al.*, 2005). The cNEB is based on the NEB (Jónsson *et al.*, 1998; Mills *et al.*, 1995; Sheppard *et al.*, 2008) method, where a series of images along the reaction coordinate (band) are created and kept equidistant during relaxation by adding spring forces between. A constrained optimization of all images except the initial and final ones is carried out using the residual minimisation method-direct inversion in the iterative subspace (RMM-DIIS) (Pulay, 1980; Wood and Zunger, 1985). This is a quasi-Newton algorithm based only on the forces and stress tensor in which the norm of the residual vector is minimised by diagonalasing the inverse of the Hessian matrix. The climbing image NEB (cNEB) is a simplification of this method, where the total number of images are reduced and the accuracy of the saddle point is increased. In the cNEB, the image with highest energy is freed from the spring constraints and its force along the tangent is inverted to allow this image to maximize its energy along the band and minimize it in all other directions. The saddle

point is the optimized image. A further modification of cNEB method is the improved tangent (Henkelman and Jónsson, 2000; Sheppard *et al.*, 2008), designed to avoid possible kinks along the band.

The IDM is the form in which the dimer method (Henkelman and Jónsson, 1999; Olsen *et al.*, 2004) has been implemented in VASP. This algorithm has been designed to find the transition state by knowing only the initial configuration and giving to the calculation the initial dimer axis, which is the one with the unstable (negative) vibrational mode.

2.10 Analysis of optimized geometries

In this section we present the methodologies we have used to obtain the properties that characterise the optimized geometries, such as: vibrational frequencies, density of states, atomic charges and atomic spin densities.

2.10.1 Vibrational frequencies

In any optimized geometry, the gradients of each vibrational mode are equal to zero. The minimum, either local or global, has all second derivatives positive, which means that all vibrational frequencies are real. A transition state, on the other hand, has one imaginary frequency, for which one of the second derivatives is negative.

In VASP, the second derivative from the energy gradients variation is calculated numerically from small displacements (in the harmonic region) of each atom at each Cartesian coordinate. In systems composed by a surface and an adsorbate, the phonons

of the former and the vibrational frequencies of the latter can be, to a good approximation, considered to be decoupled. Therefore, the calculations can be further simplified by neglecting the phonons of the surface. The Hessian matrix (matrix of the second derivative of the energy with respect to the atomic positions) is determined from the forces. Its eigenvalues are the vibrational frequencies and the eigenvectors are the vibrational normal modes of the system.

2.10.2 Density of states

In periodic solid systems, where there is a large number of atoms, the individual discrete energy levels are so close together that they form continuous bands. Density of states (DOS) plots are a convenient way to characterise these energy bands as they represent the number of states available to be occupied by electrons per unit cell at a specified energy. The DOS also hold information about the site-projected DOS (PDOS) as well as the up (α) and down (β) electronic states. PDOS are essential to study the bands involved in chemical bonds. Modifications in their intensity and position indicate charge transfers as well as ionic or covalent interactions.

2.10.3 Bader analysis of the charges

The ‘atoms in molecules’ theory was proposed by Bader based initially on the Lewis model and the Valence Shell Electron Pair Repulsion (VSEPR) for the topological analysis of the electronic density (Bader, 1994, 1990; Bader *et al.*, 1994, 1988). This is a methodology for partitioning atomic charges which is also applicable and convenient to use in condensed matter as it is based upon the electronic density and its gradient, which are magnitudes easily obtained from DFT calculations. The chemical

bond between two atoms has the highest electronic density between the two nuclei where the electron density gradient vectors start and end. 'Atoms in molecules' simply defines an atom as bound by a cavity whose surface has zero flux of the gradient vectors. Several atomic properties, such as charge and spin density can be integrated over this space and give a result not sensitive to the basis set used, unlike wavefunction population schemes (Ángyán *et al.*, 1994; De Proft *et al.*, 2002; Wiberg and Rablen, 1993).

3

Inversion thermodynamics and electronic structure of FeM_2X_4 (thio)spinels (M = Cr, Mn, Fe, Co, Ni; X = O, S)

3.1 Introduction

The electronics industry has been revolutionized over the last four decades due to the continuous miniaturization of integrated circuits. Spintronics, short for spin electronics, has emerged as the basis for the next generation of electronic devices (Felser *et al.*, 2007). The concept of spintronics is to take advantage of both the electron charge and spin in solid-state systems, and therefore its applications require magnetic materials with highly spin-polarized electrons at the Fermi energy (Žutić *et al.*, 2004). This can be achieved by half-metallic ferrimagnets (HMF) (Coey and Venkatesan, 2002) with Curie temperature higher than room temperature. The spin-polarized density of states (DOS) of these compounds has a marked asymmetry around the Fermi energy, where one of the spin channels is a conductor while the other one

behaves as an insulator (de Groot *et al.*, 1983), making them electronic spin filters. Spintronic applications are based on spin valves (Nozaki *et al.*, 2013; Sukegawa *et al.*, 2012), where two HMF layers are sandwiching a non-magnetic layer. In spintronic applications of high efficiency, the resistivity of the spin valve is required to be extremely sensible to the magnetic field (magnetoresistance) (Felser *et al.*, 2007).

The magnetoresistive behavior (Berdunov *et al.*, 2004b; Eerenstein *et al.*, 2002), and the half-metallic and ferrimagnetic (Kida *et al.*, 2011; Piekarz *et al.*, 2010; Roldan *et al.*, 2013; Zhang and Satpathy, 1991) nature of the inverse spinel magnetite (Fe_3O_4), together with the ubiquity of this iron oxide (Cornell and Schwertmann, 2003), indicates its suitability for spintronic applications (Coey and Chien, 2011; Felser *et al.*, 2007; Szotek *et al.*, 2006). The origin of these properties in Fe_3O_4 has been traditionally rationalized in terms of its inverse spinel structure. The ferrimagnetism in Fe_3O_4 arises from the antiparallel alignment of the magnetic moments of the ions in the tetrahedral and octahedral sublattices (which is known as collinear Néel configuration) (Néel, 1948), while the hopping of the extra electron in the minority channel of the spins explains the half-metallic properties (Zhang and Satpathy, 1991). Greigite (Fe_3S_4) has been shown to have a similar electronic structure to its oxide counterpart Fe_3O_4 (Roldan *et al.*, 2013). Both compounds are sometimes found associated with other transition metals of similar ionic radii (Shannon, 1976) and valence as Fe, such as Mn, Co, Ni and Cr (Slick, 1980), forming spinel compounds of formula FeM_2X_4 (Brabers, 1995). In these systems, *M* represents the transition metal and *X* represents the oxygen or sulfur atom, where the sulfide spinels are usually called

thiospinels (Charnock *et al.*, 1990; Vaughan and Craig, 1985; Vaughan and Tossell, 1981). The substituted spinels could retain the type of magnetic behavior of their parent compounds (magnetite or greigite), which is driven by a negative superexchange interaction that is stronger between ions occupying different sublattices than between ions within the same sublattice (Néel, 1948).

The crystal structure of a (thio)spinel is face-centered-cubic and the space group is $Fd\bar{3}m$. The cubic unit cell contains eight units of FeM_2X_4 where the 32 anions are in a cubic closed packed arrangement, while 8 of the tetrahedral holes and 16 of the octahedral ones are occupied by all the cations, see **Figure 3.1**. As originally suggested by Barth and Posnjak (1932), different cation arrangements of the (thio)spinel formula can be rewritten as $\left(\mathrm{Fe}_{1-x}M_x\right)_{\mathrm{A}}\left(\mathrm{Fe}_xM_{2-x}\right)_{\mathrm{B}}X_4$, where A and B denote tetrahedral and octahedral sites respectively, while x is the degree of inversion. In normal spinels (x = 0), Fe ions occupy exclusively the A sublattice and M is confined to the B sublattice. In inverted spinels (x = 1), the A sublattice holds half of the M cations and the B sublattice is equally populated with Fe and M ions. When $0 < x < 1$, Fe and M have an intermediate degree of distribution within the A and B sublattices. For all the inversion degrees, the $Fd\bar{3}m$ symmetry of the spinel is often retained, as long as all cations are fully randomly distributed within each sublattice, which makes all the sites within each sublattice effectively equivalent. In such cases the cation distribution is fully characterized by the inversion degree x. The degree of inversion in spinels has been found to be affected by different factors, including the ionic radii of the distributed species, the electronic configuration, the electrostatic energy of the lattice, the short-

range Born repulsion energy, crystal field effects, and polarization effects (Brabers, 1995; Slick, 1980).

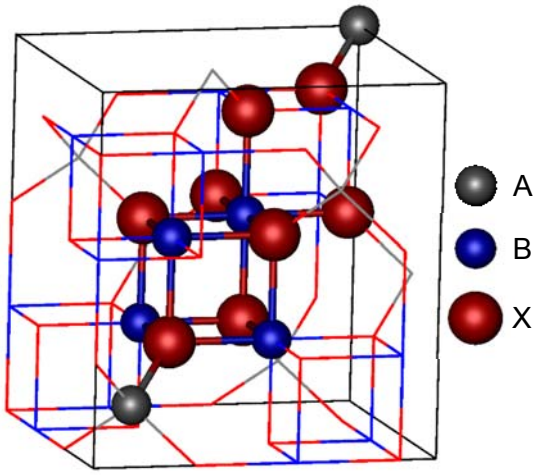

Figure 3.1. Schematic representation of one full unit cell of a perfect spinel, highlighting one of the four primitive rhombohedral cells. The spinel structure has the symmetry group $Fd\bar{3}m$ with three ion sites: tetrahedral (A), octahedral (B) cation positions and the anion (X) position.

Structural aspects of FeM_2X_4 (thio)spinels have been reported extensively in the literature, sometimes also addressing their influence on the magnetic and electronic properties. For example, these studies include: (1) the mixing, non-stoichiometry (Andersson and Stanek, 2013) and magnetic properties as a function of the cation site distribution of the Fe_3O_4-$FeCr_2O_4$ system (Robbins *et al.*, 1971); (2) the magnetic ordering of $FeCr_2O_4$ (Bacchella and Pinot, 1964; Bordács *et al.*, 2009; Klemme *et al.*, 2000; Kocsis *et al.*, 2013) and $FeMn_2O_4$ (Van Landuyt *et al.*, 1972) upon crystal symmetry lowering; (3) the relevance of the electronic structure to the magnetic

properties of $FeCr_2X_4$ (Ohgushi *et al.*, 2008); (4) the transport properties based on the half-metallic electronic structure of $FeCr_2S_4$ (Park *et al.*, 1999); (5) the magnetic structures in $FeCr_2X_4$ (Shirane *et al.*, 1964) and the colossal magnetoresistance in $FeCr_2S_4$ (Ramirez *et al.*, 1997); (6) the degree of inversion in $FeMn_2O_4$ (Boucher *et al.*, 1969; Buhl, 1969; Kulkarni and Darshane, 1985; Sinha *et al.*, 1957) and $FeCo_2O_4$ (Ferreira *et al.*, 2003; Le Trong *et al.*, 2008; Liu *et al.*, 2013); (7) the structural phase stability and magnetism in $FeCo_2O_4$ (Muthuselvam and Bhowmik, 2009); (8) the structural and magnetic properties of $FeNi_2O_4$ (Shafer, 1962), as well as (9) the thermodynamic stability (Haider *et al.*, 2012) and cation distribution of $FeNi_2S_4$ (Tenailleau *et al.*, 2006; Waldner, 2009). Nevertheless, in compounds such as these (thio)spinels, where the other transition metal's atomic number differs only by 1 from Fe, the X-ray diffraction intensities are very similar for any inversion degree, which makes it difficult experimentally to differentiate the location of the cations in the structure.

Owing to the experimental limitations for the determination of the cation arrangement in FeM_2X_4 (thio)spinels, in the present work we have used DFT+U calculations to investigate systematically how modifying the spinel composition affects the equilibrium inversion degree and how this determines the magnetic and electronic properties at a given composition. We study the influence of the nature of the M and X ions (M = Cr, Mn, Fe, Co, Ni and X = O, S) on these properties, a type of investigation that has been undertaken previously for other groups of oxide spinels (Szotek *et al.*, 2006) and Heusler alloys (Balke *et al.*, 2008; Galanakis *et al.*, 2002)

with potential application in spintronic devices. We will discuss from a thermodynamic point of view the equilibrium cation distribution of these (thio)spinels and the role of the ions' sizes and crystal field stabilization effects. We will also analyze the dependence of the electronic and magnetic structure on the degree of inversion for the normal and completely inverse systems.

3.2 Computational methods

3.2.1 Calculation details

We have carried out spin-polarized quantum mechanical calculations using density functional theory (DFT) as implemented in the Vienna *Ab-initio* Simulation Package (VASP) (Kresse and Furthmüller, 1996a, 1996b; Kresse and Hafner, 1994, 1993). The Perdew-Burke-Ernzerhof functional revised for solids (PBEsol) (Perdew *et al.*, 2008) was the version of the generalized gradient approximation (GGA) used as exchange-correlation functional for all geometry optimizations and for the calculation of all density of states (DOS), because PBEsol provides a better description of the structure of solids than its parent functional (De La Pierre *et al.*, 2011).

The semiempirical method of Grimme (D2) was also included in our calculations for modelling the long-range van der Waals interactions (Grimme, 2006). Even when these interactions are not expected to affect significantly the bulk properties of the hard solids investigated here, we have included the D2 correction at this stage because in future work we expect to study the surfaces of these solids and their interactions

with adsorbates, where dispersion effects may play a significant role (Dzade *et al.*, 2014, 2013; Haider *et al.*, 2014; Irrera *et al.*, 2013; Santos-Carballal *et al.*, 2014; Tafreshi *et al.*, 2014). The projector augmented wave (PAW) pseudopotential method (Blöchl, 1994; Kresse and Joubert, 1999) was used to describe the core electrons and their interaction with the valence electrons, *i.e.* those in level 4*d* for Fe, Co and Ni, 3*p*4*d* for Cr and Mn, 2*s*2*p* for O and 3*s*3*p* for S. The kinetic energy cutoff for the plane-wave basis set expansion was set at 520 eV for the geometry optimizations in order to avoid the Pulay stress arising from the cell shape relaxations. A Monkhorst-Pack grid of $7\times7\times7$ *Γ*-centred *k*-points (Baldereschi, 1973; Chadi and Cohen, 1973; Monkhorst and Pack, 1976) was used for all calculations. During relaxation, Feynman forces on each atom were minimized until they were less than $0.01\ \mathrm{eV}\cdot\mathrm{Å}^{-1}$. For the calculation of the DOS we applied the tetrahedral method with Blöchl corrections. Atomic charges and atomic spin moments were analyzed using the Bader partition methodology (Bader, 1990) in the implementation of Henkelman and collaborators (Henkelman, Arnaldsson, & Jónsson, 2006; Sanville, Kenny, Smith, & Henkelman, 2007; Tang, Sanville, & Henkelman, 2009).

In order to improve the description of the highly correlated 3*d* electrons in the spinels under study, we have included the Dudarev *et al.* (1998) approach for the *d* orbital correction within the DFT + *U* method (Anisimov *et al.*, 1992). We report in **Table 3.1** the values used for the on-site Coulomb interaction term of *d* Fe and *d M*. These values were determined by fitting the calculated positions of the *d* band centers to those obtained from calculations using the screened hybrid functional of Heyd-

Scuseria-Ernzerhof (HSE06) (Heyd and Scuseria, 2004a, 2004b; Heyd *et al.*, 2006, 2005, 2003; Krukau *et al.*, 2006; Peralta *et al.*, 2006), which provides band gaps of better quality than semilocal functionals (Henderson *et al.*, 2011). The HSE06 is made from the Perdew-Burke-Ernzerhof functional (PBE) (Perdew *et al.*, 1997, 1996a) exchange and correlation components mixed with 25% of short-range Hartree-Fock (HF) exchange (Heyd *et al.*, 2003). The Coulomb potential exchange is replaced by a screened potential (with screening parameter $\omega = 0.207$ Å^{-1}) in order to define the separation between the short- and long-range components of the HF exchange (Krukau *et al.*, 2006). While the amount of short-range HF is a constant determined by perturbation theory, making HSE06 an adiabatic connection functional in this part of the potential (Perdew *et al.*, 1996b), its screening parameter is a reasonable system-averaged value across a wide variety of systems, giving better agreement with experiments in the case of semiconductors than for metals or insulators (Henderson *et al.*, 2011).

For the fitting, we carried out single-point calculations with both PBEsol + *U* and HSE06, using unrelaxed structures with normal cation distributions (a_0 and u_0 were taken from experiment for these calculations, values are listed in **Table 3.2**). In a first step, we determine U_{eff} for Fe, by considering the Fe_3O_4 and Fe_3S_4 electronic structures (which have been studied before) (Devey *et al.*, 2009; Haider *et al.*, 2012; Roldan *et al.*, 2013). We then keep these values for Fe and perform a set of DFT + *U* calculations where the effective Hubbard parameter (U_{eff}) of the *M* ion was changed in steps of 0.5

eV from 0 to 6.0 eV. In all the HSE06 calculations, we used the same settings as for the PBEsol simulations.

Table 3.1. Summary of the optimum effective Hubbard parameter (U_{eff}) in eV used through this work for the spinel oxides and sulfides.

	Cr	Mn	Fe	Co	Ni
FeM_2O_4	4.0	3.5	4.0	1.5	5.5
FeM_2S_4	2.0	2.5	3.5	0.5	4.5

We found that the optimum U_{eff} values for the Cr, Mn and Fe ions in the spinel oxides are within 0.5 eV of the ones previously found for PBE + *U* by Wang *et al.* (2006) via comparison of experimental and theoretical formation energies of metal oxides. The two exceptions are the U_{eff} values for Co and Ni which differ, according to our methodology, by 1.8 and 0.9 eV respectively from the ones reported by Wang *et al.* (2006) The smaller U_{eff} values of the thiospinels, compared to their oxide counterparts, reflect their more covalent character. The U_{eff} for Mn-based thiospinel compares well with the value reported by Rohrbach *et al.* (2003), while, according to our methodology, the one for Fe is 1.5 eV above the one used by the same authors. Hence, in general our U_{eff} are similar to previously employed values, with some small differences which can be expected from the use of a different starting functional (PBEsol in our case), the implementation of the method, different compound or different fitting procedure.

All the calculations were performed in the rhombohedral primitive unit cell of the FeM_2X_4 spinels, which comprises 14 atoms, see **Figure 3.1**. For each composition of $\left(\mathrm{Fe}_{1-x}M_x\right)_{\mathrm{A}}\left(\mathrm{Fe}_xM_{2-x}\right)_{\mathrm{B}}X_4$, we considered three values of x (0, 0.5 and 1.0). When using this cell, the site occupancy artificially lowers the symmetry from space group $Fd\bar{3}m$ (No. 227) in the normal spinel to *R3m* (No. 160) in the half-inverted and to *Imma* (No. 74) in the fully-inverted spinel (Fritsch and Ederer, 2010). The use of the primitive cell ensures that there is a single cation configuration for each of these three degrees of inversion, which simplifies the simulations, allowing us to scan a wide range of FeM_2X_4 compositions in the present study. This approximation follows previous work where the use of the primitive cell model has been found to adequately describe experimental properties of half- and fully-inverted spinels (Fritsch and Ederer, 2011a, 2010; Seminovski *et al.*, 2012; Walsh *et al.*, 2007; Wei and Zhang, 2001). However, we cannot rule out that the use of larger supercells could actually lead to cation configurations with lower energies for the same inversion degree, *e.g.* as found in a recent study of $CoFe_2O_4$ (Fritsch and Ederer, 2011b).

Following the collinear Néel model, the initial magnetic moments of the atoms within each sublattice were set parallel among themselves and antiparallel to those of the other sublattice. For each inversion degree, we run several calculations specifying different initial magnetic moments, corresponding to different combinations of low- and high-spin states for the transition metal ions in each sublattice, in order to find the ground state. The magnetic moments were allowed to relax during each of the calculations. It should be noted that the magnetic structure with antiparallel

sublatticesis not strictly valid in the case of $FeCr_2O_4$, which is known to have a spiral magnetic structure (Shirane *et al.*, 1964). However, for the sake of comparison with the other spinel systems, we have not considered its different magnetic structure in this study.

The experimental lattice (a_0) and anion (u) parameters (defining the anion position in the crystal) of the spinels are shown on **Table 3.2**. These were used as the starting structures for our simulations, where a_0 and the internal coordinates were allowed to relax fully for each inversion degree. We kept the cell shape perfectly rhombohedral in such a way that the conventional cell was always cubic. As $FeMn_2S_4$ and $FeCo_2S_4$ spinels have not been characterized so far, we postulated an initial hypothetical structure for both. For the Mn- and Co-based thiospinels, we kept the same initial anion parameter as in their oxide counterparts and scaled up their initial lattice parameter according to the equation:

$$a_0\left(\mathrm{Fe}M_2\mathrm{S}_4\right)=\frac{a_0\left(\mathrm{Fe}_3\mathrm{S}_4\right)\cdot a_0\left(\mathrm{Fe}M_2\mathrm{O}_4\right)}{a_0\left(\mathrm{Fe}_3\mathrm{O}_4\right)} \tag{3.1}$$

which gives the estimates shown in **Table 3.2**.

Table 3.2. Summary of the initial unit cell lattice (a_0) and anion (u_0) parameters of FeM_2X_4 spinels used in this work. The relaxed *a* and *u* are also reported for x = 0, 0.5 and 1. Note that the origin is the center of symmetry.

Structure	Experimental		$x = 0$		$x = 0.5$		$x = 1$	
	a_0 (Å)	u	a (Å)	u	a (Å)	u	a (Å)	u
$FeCr_2O_4$[A]	8.38	0.261	8.351	0.261	8.372	0.261	8.392	0.265
$FeCr_2S_4$[A]	10.00	0.259	9.830	0.258	9.855	0.262	9.898	0.260
$FeMn_2O_4$[B]	8.51	0.250	8.420	0.256	8.436	0.265	8.446	0.267
$FeMn_2S_4$[C]	10.04	0.250	9.911	0.255	9.949	0.260	9.983	0.263
Fe_3O_4[D]	8.390	0.255	8.345	0.254	--	--	--	--
Fe_3S_4[E]	9.88	0.251	9.764	0.255	--	--	--	--
$FeCo_2O_4$[F]	8.24	0.259	8.196	0.256	8.168	0.259	8.119	0.271
$FeCo_2S_4$[C]	9.73	0.259	9.363	0.263	9.286	0.260	9.297	0.250
$FeNi_2O_4$[G]	8.29	0.258	8.124	0.259	8.123	0.260	8.133	0.255
$FeNi_2S_4$[H]	9.47	0.257	9.463	0.260	9.438	0.257	9.396	0.251

[A] Shirane *et al.* (1964)

[B] Montoro (1938)

[C] Experimental information is not available. Parameters are obtained by scaling the values for the corresponding oxides.

[D] Wright *et al.* (2002)

[E] Skinner *et al.* (1964)

[F] Ferreira *et al.* (2003)

[G] Shafer (1962)

[H] Tenailleau *et al.* (2006)

3.2.2 Configurational free energy of inversion

The calculation of the inversion degree in spinels containing two different cations is based on the thermodynamic considerations of Navrotsky and Keppla (1967), which have proved to agree well with experiments (Ndione *et al.*, 2014; Palin *et al.*, 2008; Seko *et al.*, 2010; Seminovski *et al.*, 2012; Tielens *et al.*, 2006). This methodology is based on the treatment of the spinels' cation distribution as a chemical equilibrium. We calculated the configurational free energy of inversion per formula unit ΔF_{config} as,

$$\Delta F_{\text{config}} = \Delta E_{\text{config}} - T \cdot \Delta S_{\text{config}} \tag{3.2}$$

where ΔE_{config} is the inversion energy per formula unit, T is the temperature and ΔS_{config} is the ideal configurational entropy also per formula unit, which is calculated as,

$$\Delta S_{\text{config}} = -R\left[x\ln x + (1-x)\ln(1-x) + x\ln {}^{x}\!/_{2} + (2-x)\ln\left(1-{}^{x}\!/_{2}\right)\right] \tag{3.3}$$

where R is the ideal gas constant. ΔS_{config} = 0 and 11.59 $J{\cdot}mol^{-1}{\cdot}K^{-1}$ for x = 0 and 1 respectively, while it reaches the maximum value 15.88 $J{\cdot}mol^{-1}{\cdot}K^{-1}$ for the complete random distribution at x = 2/3. The above expression means that we have only considered ideal contributions to the configurational entropy, in line with previous work (Seko *et al.*, 2010; Seminovski *et al.*, 2012; Tielens *et al.*, 2006). We are also ignoring vibrational contributions to ΔF, as their contributions are typically small compared to configurational energies and entropies (Seminovski *et al.*, 2012; Tielens *et al.*, 2006).

3.3 Equilibrium structures

Table 3.2 shows the optimized *a* and *u* for the three inversion degrees considered (*x* = 0, 0.5 and 1.0). In general, the optimized lattice parameter is within 2% from the experimental value, where this is available. However, the relaxed lattice parameter for $FeCo_2S_4$, in the best case (*x* = 0), is 3.8% away from the initial estimated value, which may be an artefact due to the assumption of linearity between the lattice constants of Fe_3O_4, $FeCo_2O_4$ and their sulfide counterparts. After relaxation of the structures, *u* was still different from the value of ¼ that it has in the perfect spinel. This deviation reflects the displacement, in the (111) direction, of the anion from its ideal position in order to accommodate cations of specific volume. The biggest deviation in *u* in comparison with the experimental value was for the inverse Mn- and Co-based oxide spinels, **Table 3.2**. We see that in general, *u* and *a* values are sensitive to the cation distribution, although no systematic rule can be derived from their dependence.

3.4 Equilibrium inversion degrees

The configurational inversion energy per formula unit (ΔE_{config}) was fitted *versus* the degree of inversion (*x*) using a quadratic regression curve, see **Figure 3.2 (a)**. More details regarding the empirical relationship (Kriessman and Harrison, 1956) and theoretical justification (O'Neill and Navrotsky, 1983) of the above fitting in terms of *x*, *a* and *u* can be found elsewhere. In this fitting, we defined the normal spinel as the standard state for a given condition of temperature and pressure.

Using the quadratic equation for ΔE_{config}, it is possible to interpolate the inversion energy for any value of x between 0 and 1. Based on this protocol, we have also estimated the configurational free energy of inversion for a typical firing temperature of 1000 K (Muthuselvam and Bhowmik, 2009; Ohgushi *et al.*, 2008; Shafer, 1962; Tenailleau *et al.*, 2006) (among the known cases in this study, $FeNi_2S_4$ is an exception, as it is usually prepared at 573 K (Tenailleau *et al.*, 2006; Townsend *et al.*, 1977) because it decomposes at 734 K (Craig, 1971)) by using equations (3.2) and (3.3). Compounds are usually quenched after synthesis at the firing temperature, retaining the equilibrium cation distribution. We analysed the ΔE_{config} dependence with x and provided the equilibrium values of x, *i.e.* the ones that satisfy $\partial F_{\text{config}} / \partial x = 0$ at 1000 K, see **Figure 3.2 (b)**.

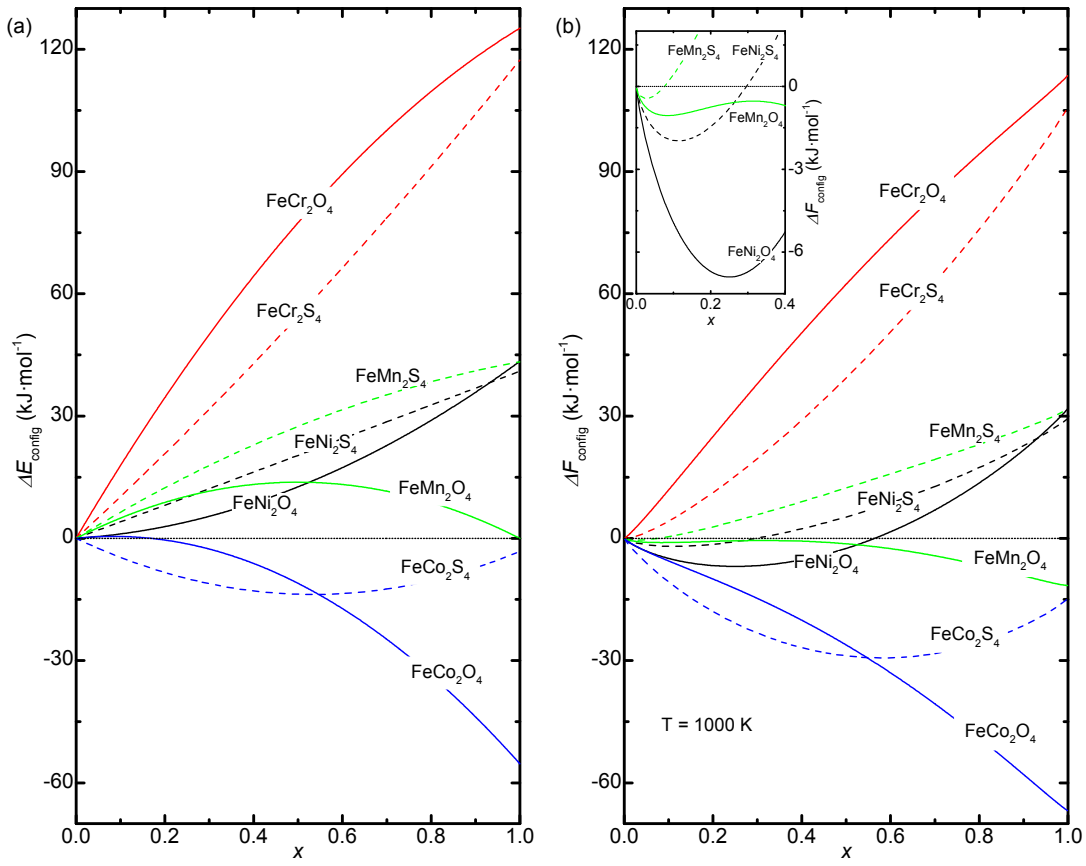

Figure 3.2. (a) Configurational inversion energy (ΔE_{config}) and (b) configurational inversion free energy (ΔF_{config}) as a function of the inversion degree for FeM_2X_4 spinels. Inset shows enlargement of ΔF_{config} for the $FeMn_2X_4$ and $FeNi_2X_4$ (thio)spinels.

We found the minimum of ΔE_{config} to correspond to a normal distribution of cations, with the exception of Co-based systems and $FeMn_2O_4$, **Figure 3.2 (a)**. The lowest value of ΔE_{config} for $FeCo_2O_4$ spinel is found to be an inverse cation distribution, whereas for $FeMn_2O_4$, both normal and inverse cation distribution structures lie at similar energies, while the intermediate degree of inversion (x = 0.5) is only ~14 $kJ \cdot mol^{-1}$ above the ground state. $FeCo_2S_4$ is an atypical thiospinel in this study, in the

sense that it shows a critical point of low energy with intermediate cation distribution, at $x = 0.53$.

$FeCr_2X_4$. From **Figure 3.2 (b)**, we deduced that at 1000 K, the Cr-based (thio)spinels are normal under equilibrium conditions, as a result of a highly endothermic process of inversion. This normal cation distribution of $FeCr_2X_4$ is supported by powder neutron diffraction intensities (Shirane *et al.*, 1964) at room temperature and for the oxide by Mössbauer measurements (Robbins *et al.*, 1971) and DFT calculations (Andersson and Stanek, 2013), see **Table 3.3**.

Table 3.3. Summary of equilibrium inversion degree (x) of FeM_2X_4 (thio)spinels from previous reports and this work.

	x	x at 1000 K
$FeCr_2O_4$	~ 0.0[A]	0.00
	0.00[B]	
$FeCr_2S_4$	~ 0.0[C]	0.00
$FeMn_2O_4$	0.5[D]	0.10 and 1.00
	0.91[E]	
$FeMn_2S_4$	--[F]	0.03
$FeCo_2O_4$	0.52[G]	1.00
	0.54[H]	
	0.565[I]	
	0.605[J]	
	0.7[K]	
	1.0[L]	
$FeCo_2S_4$	--[F]	0.48
$FeNi_2O_4$	--[F]	0.25
$FeNi_2S_4$	~ 0.05[M]	0.12
	0.82 or 1.00[N]	
	1.00[O]	

[A] Andersson and Stanek (2013) and Shirane *et al.* (1964)

[B] Robbins *et al.* (1971)

[C] Shirane *et al.* (1964)

[D] Kulkarni and Darshane (1985) and Sinha *et al.* (1957)

[E] Boucher *et al.* (1969) and Buhl (1969)

[F] Experimental information is not available.

[G] Smith *et al.* (1978)

[H] Ferreira *et al.* (2003)

[I] Liu *et al.* (2013)

[J] Takahashi and Fine (1972)

[K] Murray and Linnett (1976)

[L] Blasse (1963) and Lotgering (1956)

[M] Cemič and Kleppa (1987)

[N] Vaughan and Craig (1985)

[O] Charnock *et al.* (1990), Tenailleau *et al.* (2006) and Waldner (2009)

$FeMn_2X_4$. At 1000 K, the scenario for $FeMn_2O_4$ is unique in this study, as in addition to the global minimum of ΔF_{config} at $x = 1$, it has a local one at $x = 0.1$. The local minimum is within a portion of shallow inversion free energy ($0 < x < 0.3$), which may lead to a metastable inversion degree anywhere within this range, for this spinel's equilibrium structure, see **Figure 3.2 (b)**. The behaviour of this thermodynamic property in $FeMn_2O_4$ can be rationalized in terms of the small change of ΔE_{config} with x as well as in $E_{x=0} \approx E_{x=1}$. The upper limit ($x = 0.3$) of the shallow inversion free energy that we predicted agrees semiquantitatively with the experimental inversion degree ($x = 0.5$) found for $FeMn_2O_4$ in a conductivity and thermopower (Kulkarni and Darshane, 1985) investigation, as well as inferred from the study of a series of spinels (Sinha *et al.*, 1957), see **Table 3.3**. The inversion degree has also been found in neutron diffraction experiments to be at $x = 0.91$ (Boucher *et al.*, 1969; Buhl, 1969) which is in reasonably good agreement with the global minimum calculated here. We speculate that the two inversion degrees of $FeMn_2O_4$ may be hampered by kinetic control by a barrier that is just around 4 kJ·mol^{-1} below $2k_BT$ (when $T = 1000$ K), which explains the different cation arrangements described in the literature. According

to our calculations, samples of $FeMn_2O_4$ synthesized above 1150 K can only have inverse cation distribution, as the metastable inversion degree vanishes. $FeMn_2S_4$, on the other hand, is predicted to be mostly normal (x = 0.03) under equilibrium conditions, **Figure 3.2 (b)**.

$FeCo_2X_4$. $FeCo_2O_4$ is the only completely inverse spinel under equilibrium conditions, due to the highly exothermic process of inversion, which agrees with experimental evidence (Blasse, 1963; Lotgering, 1956). Nevertheless, our results for the Co-based oxide disagree with the equilibrium inversion degree of x = 0.565 and 0.605 obtained by means of fitting the dependence of the magnetic moment with x (Liu *et al.*, 2013; Takahashi and Fine, 1972) and the similar values within the range $0.52 \leq x \leq 0.7$ derived from Mössbauer spectra (Ferreira *et al.*, 2003; Murray and Linnett, 1976; Smith *et al.*, 1978), see **Table 3.3**. Its sulfide counterpart, which has not been studied experimentally, shows an equilibrium inversion degree of x = 0.48 in our calculations.

$FeNi_2X_4$. $FeNi_2O_4$ (and to a lesser extent $FeNi_2S_4$) is predicted to have an intermediate distribution of the cations under equilibrium conditions of around x = 0.25 (x = 0.12 for the thiospinel case). Our results agree with suggestions of partially inverted $FeNi_2S_4$, based on a high temperature calorimetry study of natural samples (Cemič and Kleppa, 1987), see **Table 3.3**. However, they disagree with the more recent description of synthetic $FeNi_2S_4$ samples as completely inverse spinel based on a neutron powder diffraction measurements at temperatures between 100 and 573 K (Tenailleau *et al.*, 2006), thermodynamic-based modelling (Waldner, 2009), EXAFS experiment (Charnock *et al.*, 1990) and Mössbauer data (Vaughan and Craig, 1985). Based on our

calculations and the fact that synthetic $FeNi_2S_4$ samples cannot be annealed to temperatures higher than 734 K (Craig, 1971), as they decompose, we propose a rationalization of the different cation arrangements found in natural and synthetic samples of this mineral. We suggest that synthesis produces a kinetic product (with $x \sim 1.00$) and that these conditions cannot reproduce the hypogene processes occurring in the ores deep below the Earth's surface that lead to the thermodynamic product found in natural samples ($x \sim 0$).

3.5 Size of ions and crystal field stabilization effects

We analyze now the effect of cation size and crystal field stabilization energy on the distribution of cations under equilibrium conditions.

Assuming the hard-sphere model, where the ions are spherical, rigid and in contact, the ratio between the tetrahedral (R_A) and octahedral (R_B) bond distances will depend solely on u. The tetrahedral holes are smaller than the octahedral ones for $u < 0.2625$ (Hill *et al.*, 1979). Taking into account that for most systems under study here, u is below that value (with a few exceptions in the relaxed structures, see **Table 3.2**), we can consider that $R_A < R_B$ is expected for a stable spinel.

According to the Shannon effective radii (Shannon, 1976), which depend on the coordination number and oxidation state, Fe_A^{2+} cation has bigger radius than Cr_B^{3+}, Co_B^{3+} and Ni_B^{3+} leading to an inverse cation distribution. This agrees very well with our thermodynamic DFT + U calculations for $FeCo_2O_4$ and moderately with the

partially inverse (x = 0.48) $FeCo_2S_4$ spinel. However, we found the opposite equilibrium distribution for the $FeCr_2X_4$ system and a very small inversion degree (x < 0.25) for the $FeNi_2X_4$, indicating that this factor is not the key parameter governing the inversion degree in these compounds. On the other hand, the Mn_B^{3+} Shannon radius is bigger than that of Fe_A^{2+}, predicting a normal (thio)spinel. Yet, whereas the sulfide compound is a completely normal spinel, the oxide has a local minimum for $0 < x < 0.3$ and the global one at $x = 1$.

Since we are dealing with open shell *d* transition metals, the crystal field is also an important effect to consider. McClure (1957), and independently Dunitz and Orgel (1957), derived the crystal field stabilization energy for ions (in oxides) with tetrahedral and octahedral environments, to estimate the relative stability of normal and inverse spinels. Subtracting the tetrahedral stabilization energy from the octahedral one (octahedral site preference energy − OSPE) gives an idea of the octahedral site preference. The OSPE for Fe^{2+} (16.3 kJ/mol) is smaller than for the rest of the cations under consideration here, *i.e.* 195.4 kJ/mol for Cr^{3+}, 105.9 kJ/mol for Mn^{3+}, 79.5 kJ/mol for Co^{3+} and 95.4 kJ/mol for Ni^{2+} (note that to date no estimation of OSPE for Ni^{3+} is reported). These OSPEs clearly show the preference for normal spinels.

The ambiguities in our results are probably not surprising, because earlier attempts to correlate cation distribution with their size and crystal field effects were also not

successful, or at least, unable to provide a complete prediction of the degrees of inversion (Cormack *et al.*, 1988).

3.6 Atomic spin moments and charges

In this and the next section we analyze the electronic and magnetic properties of the spinel materials for the extreme cases of $x = 0$ and $x = 1$.

The total magnetization of saturation (M_S) is defined experimentally as the maximum magnetic moment per formula unit of a compound under an increasing magnetic field. This magnitude can also be calculated according to the Néel model as the sum of the atomic spin densities (m_s) in the tetrahedral and octahedral sublattices per formula unit (Néel, 1948). **Table 3.4** shows the atomic spin densities for all the compounds under study here. When $x = 0$ in the oxide spinels, $m_s(Fe_A)$ is around 4 μ_B/atom, which is in good agreement with a high-spin electronic distribution for $Fe_A^{2+}: e_\uparrow^2 e_\downarrow^1 t_{2\uparrow}^3$, with the exception of the deviation in the Cr-based compound. For the normal thiospinels there is more consistency in the $m_s(Fe_A)$ values, as they lie in the range −3.41 and −3.53 μ_B/atom and only in semiquantitative agreement with the Néel model. For the *M* cation in the normal Cr- and Mn-based (thio)spinels, the atomic spin densities are also in good agreement with high-spin electronic distributions. We found that our DFT+*U* calculations underestimated the atomic spin moment of $FeCo_2O_4$ (when $x = 0$) by 1.28 μ_B/atom compared with the one expected from the Néel model for the high-spin distribution of $Co_B^{3+}: t_{2g\uparrow}^3 t_{2g\downarrow}^1 e_{g\uparrow}^2$. In its sulfide counterpart with normal distribution, our

calculated value compares well with the one predicted from a low-spin distribution of Co_B^{3+}, which renders the ions as non-magnetic. In the case of Ni_B^{3+}, we also found it to be low spin $t_{2g\uparrow}^3 t_{2g\downarrow}^3 e_{g\uparrow}^1$, although our results overestimated by 0.39 μ_B/atom and underestimated by 0.10 μ_B/atom the expected value for the oxide and sulfide respectively. This agrees with the low-spin cation occupying the octahedral positions in violarite, interpreted previously as Fe^{2+} (Vaughan and Craig, 1985).

Table 3.4. Atomic spin density per atom (m_s) and total spin magnetization of saturation per formula unit (M_S) both calculated by means of a Bader analysis and in μ_B.

Spinel	x	m_s				M_S	m_s				M_S
		A	B1	B2	X = O		A	B1	B2	X = S	
$FeCr_2X_4$	0	−3.72	2.92	--	−0.03	2.00	−3.46	2.95	--	−0.11	2.00
$FeCr_2X_4$	1	−3.50	2.82	4.09	0.15	4.00	−3.28	2.86	3.79	0.16	4.00
$FeMn_2X_4$	0	−3.97	4.16	--	−0.09	4.00	−3.53	4.03	--	−0.13	4.00
$FeMn_2X_4$	1	−4.49	3.73	4.17	0.15	4.00	−4.17	3.94	3.84	0.10	4.02
Fe_3X_4	--	−4.04	3.91	--	0.05	4.00	−3.44	3.43	--	0.04	3.60
$FeCo_2X_4$	0	−3.95	2.72	--	0.13	2.00	−3.45	−0.04	--	−0.08	−3.87
$FeCo_2X_4$	1	−2.44	0.01	4.11	0.08	2.00	−0.91	0.03	3.32	0.00	2.46
$FeNi_2X_4$	0	−4.04	1.39	--	−0.18	−2.00	−3.41	0.90	--	−0.02	−1.69
$FeNi_2X_4$	1	−1.89	1.59	4.10	0.05	4.00	−0.52	0.86	3.50	0.04	4.00

In the inverse (thio)spinels, the calculated spin densities for Fe_{B2}^{2+} were slightly overestimated in the oxides compared with the Néel model, while they were more moderately underestimated in the sulfides considering a high-spin electronic

distribution of $t_{2g\uparrow}^3 t_{2g\downarrow}^1 e_{g\uparrow}^2$ for these ions, see **Table 3.4**. The calculated atomic spin densities of the inverse Cr- and Mn-based (thio)spinels agree better, especially in the cations occupying the octahedral (B1) positions, with the high-spin electronic distribution for these ions, as described for the normal spinels. However, in the Co- and Ni-based inverse compounds, we found low-spin densities for these atoms in the B1 positions, where the nearly diamagnetic Co_{B1} in the inverse $FeCo_2O_4$ agrees with experiments (Blasse, 1963; Lotgering, 1956). Notable exceptions are the Co_A^{3+} in the thiospinel and Ni_A^{3+} in both oxide and sulfide compounds, where our calculations shift m_S by more than 1 μ_B/atom with the expected value (in the best case) from a low-spin electronic distribution for these atoms.

There is a disagreement between the Fe_3X_4 atomic spin moment expected from the Néel model and the one obtained from our DFT + *U* calculations. Assuming an inverse cation distribution, for Fe_A^{3+}, the high spin electronic distribution $e_\uparrow^2 t_{2\uparrow}^3$ predicts an atomic spin density of 5 μ_B, which is approximately 1 and 1.6 μ_B underestimated by our calculations for the oxide and sulfide respectively. The spin density of the Fe_B ions is also underestimated from a high spin intermediate between Fe^{2+} and Fe^{3+}. An excellent agreement is found for Fe_3O_4, as the calculated M_S = 4.00 μ_B/f.u. is equal to the one found previously (Roldan *et al.*, 2013; Santos-Carballal *et al.*, 2014; Zhang and Satpathy, 1991). Although the magnetization of saturation of Fe_3S_4 should be treated more cautiously, as different values have been found depending on the method used (2.0 (Coey *et al.*, 1970), 3.44 (Roldan *et al.*, 2013), 3.13 μ_B/f.u.(Chang *et al.*,

2008)), our calculated value compares well with reference (Roldan *et al.*, 2013). For Fe_3X_4, the calculated spin magnetization of saturation also fits the model of inverse spinels with the highest charged Fe filling the tetrahedral positions (Spender *et al.*, 1972; Vaughan and Ridout, 1971; Zhang and Satpathy, 1991).

The most stable normal cation distribution of $FeCr_2O_4$ gave the closest M_S to the experimental one, although still overestimated by 1.35 μ_B/f.u., as this measurement was carried out at a temperature in which the spins are not collinear anymore (Shirane *et al.*, 1964). In the case of its normal sulfide counterpart, the difference in spin magnetization of saturation with the experiments is smaller (0.41 μ_B/f.u.) (Shirane *et al.*, 1964).

The Ni-based (thio)spinels are found experimentally to be paramagnetic (Shafer, 1962; Townsend *et al.*, 1977; Vaughan and Craig, 1985). In the oxide this has been explained as being due to high-spin Fe^{3+} ions exclusively localized on the A sublattice whose spins compensate completely the [$Ni^{2+}Ni^{3+}$] occupying the octahedral positions (Shafer, 1962). In the sulfide this has been rationalized on the basis of an A sublattice filled by Ni^{3+} and low-spin Fe^{2+} occupying octahedral positions (Vaughan and Craig, 1985). Here, based on our calculated spin magnetization of saturation and assuming intermediate degrees of cation distribution, we present a fresh explanation for the paramagnetism of $FeNi_2X_4$. Considering that M_S changes linearly with x, we may postulate that the oxide and sulfide will be paramagnetic when x = 0.33 and 0.30 respectively. Although this suggestion agrees with the oxide and sulfide equilibrium inversion degree calculated in section 3.1, it shows that paramagnetism in these

compounds may be due not to the canonical inverse spinel structure with integer oxidation numbers, but to intermediate inversion degrees.

To the best of our knowledge, there is no experimental determination of the saturation magnetization of either $FeCo_2S_4$ or $FeMn_2S_4$. Although we found both compounds to be ferrimagnetic, the measurement of M_S for $FeCo_2S_4$ may be essential to determine the inversion degree of this spinel, as our calculation of the normal and inverse cation distributions show different magnetizations of saturation. Our results agree with the ferrimagnetic behaviour described for Fe_3O_4 (Verwey, 1939), Fe_3S_4 (Chang *et al.*, 2009, 2008; Coey *et al.*, 1970; Dekkers *et al.*, 2000; Devey *et al.*, 2009; Spender *et al.*, 1972; Vandenberghe *et al.*, 1991; Vaughan and Tossell, 1981), $FeCo_2O_4$ (Kawano *et al.*, 1976) and $FeMn_2O_4$ (Van Landuyt *et al.*, 1972), below the Curie (Néel) temperature.

Table 3.5 shows the charges (q) gained or lost by an atom with respect to the neutral atom in the FeM_2X_4 spinels. We clearly appreciate, that charges are systematically underestimated for all the FeM_2X_4 (thio)spinels. For Fe_3S_4 as well as the Cr- and Mn-based (thio)spinels, q_A is frankly smaller than q_B for any inversion degree and also for the inverse $FeCo_2O_4$. However, for the Co- and Ni-based systems, the relative charges of the atoms in the tetrahedral and octahedral positions is different in the oxide and sulfide. In the spinel oxides, together with Fe_3O_4 and the normal Co- and Ni-thiospinels, q_A is bigger than q_B, while in the inverse thiospinels, it is the other way round.

Table 3.5. Calculated Bader charges in the FeM_2X_4 spinels.

Spinel	x	A	B1	B2	X = O	A	B1	B2	X = S
$FeCr_2X_4$	0	1.33	1.75	--	−1.21	0.92	1.22	--	−0.84
$FeCr_2X_4$	1	1.47	1.76	1.58	−1.20	1.11	1.22	1.12	−0.86
$FeMn_2X_4$	0	1.50	1.56	--	−1.16	0.95	1.18	--	−0.83
$FeMn_2X_4$	1	1.41	1.69	1.68	−1.20	1.08	1.21	1.17	−0.86
Fe_3X_4	--	1.65	1.51	--	−1.16	0.93	1.00	--	−0.73
$FeCo_2X_4$	0	1.52	1.34	--	−1.05	0.86	0.54	--	−0.49
$FeCo_2X_4$	1	1.30	1.31	1.68	−1.07	0.46	0.60	0.95	−0.50
$FeNi_2X_4$	0	1.61	1.18	--	−0.99	0.86	0.57	--	−0.50
$FeNi_2X_4$	1	1.27	1.16	1.67	−1.03	0.26	0.61	0.99	−0.46

3.7 Electronic density of states

3.7.1 $FeCr_2X_4$

The density of states (DOS) in **Figure 3.3** show that at x = 0, $FeCr_2X_4$ is half-metallic, which we confirmed by the integer value of total spin magnetization (M_S = 2.00 μ_B/f.u.), see **Table 3.4**. An integer value of the total spin magnetization discriminates half-metals and insulators from metals. The total number of electrons of any stoichiometric system is integer (n) and if it has a band gap at least in one spin channel, there is an integer number of electrons (n') there too. This makes the difference ($n'' = n - n'$), which is the number of electrons on the band that crosses the Fermi level also integer. Therefore, the magnetization of saturation, *i.e.* the difference of n' and

n'', is also integer (Coey and Chien, 2011; Coey and Sanvito, 2004; Coey and Venkatesan, 2002; Coey *et al.*, 2001).

The DOS shows a sharp peak of the partially-occupied *e* level of Fe_A ions in the majority spin channel (α) crossing the Fermi energy, which is weakly hybridized with the empty Cr e_g level in the oxide spinel, while the minority spin channel (β) shows a gap near E_F. There is a nearly equally intense band due to the occupied Cr_B t_{2g} level in the majority channel of the spins at −3.0 eV in the oxide (−1.75 eV in the sulfide), which suggests that the half-metallic properties do not involve the sublattice B. In the oxide, the other valence bands of the Fe_A ions (t_2 and *e* levels) appear in the minority channel of the spins below −2.5 eV, always strongly hybridized with the O 2*p* orbitals. However, the Cr t_{2g} level, together with a small contribution from the e_g orbitals, in the valence part of the majority spin channel are weakly hybridized with the O 2*p* orbitals. The unoccupied t_2 bands of Fe_A appear at 3.0 eV in the majority channel of the spins while Cr_B has the unoccupied t_{2g} band in the majority channel of the spins (1.5 eV) and the t_{2g} and e_g levels in the minority channel of the spins (2.5 and 4.0 eV).

The inversion of half of the Cr cations to the tetrahedral positions in $FeCr_2X_4$, generates four non-equivalent types of atoms (B1 and B2 are the two types of atoms occupying B positions), see **Figure 3.3** right panels. With this cation distribution, the (thio)spinel is still half-metallic (M_S = 4.00 μ_B/f.u., see **Table 3.4**), but unlike in the normal spinel structure, through the minority channel of the spins due to the partially-occupied t_2 level of the Cr_A ions. All the Cr_A bands are shifted towards higher energy values with respect to Fe_A in the normal (thio)spinel. The Cr_{B1} *d* bands appear roughly in the same

position as in the normal (thio)spinel, although less intense. The e_g and t_{2g} levels of Fe_{B2}, which lie very close, are around −8.0 and 1.5 eV in the α and β channel of the spins, respectively. As a result of the cations' shifted and split bands, there is less hybridization of the O 2*p* orbitals in the valence regions compared to the normal spinel, which are prominent in this section. The main difference, for any cation distribution, between the DOS of $FeCr_2S_4$ and its oxide counterpart is that all the bands in the sulfide are squeezed towards the Fermi energy.

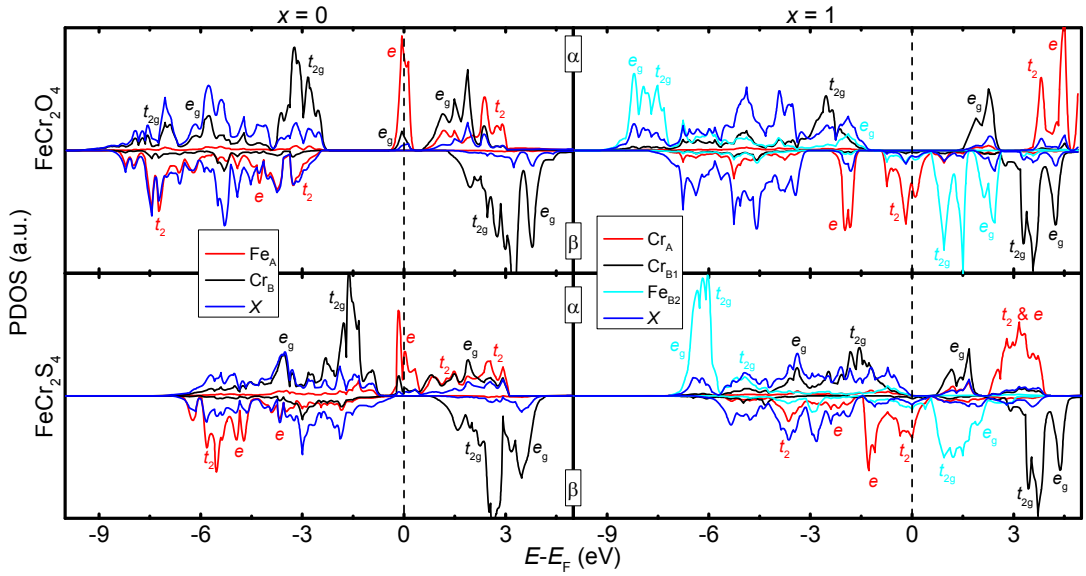

Figure 3.3. Atomic projections of the spin decomposed total density of states (PDOS) for $FeCr_2O_4$ and $FeCr_2S_4$. Fe and Cr contributions are from the 3*d* bands. O and S contributions are from the 2*p* and 3*p* orbitals respectively.

3.7.2 $FeMn_2X_4$

When the $FeMn_2X_4$ (thio)spinel is normal ($x = 0$), the Fe_A e and t_2 bands, which are hybridized, appear in the maximum of the valence and minimum of the conduction bands in the minority and majority channel respectively, see **Figure 3.4** left panels. The half-metallic character of the normal $FeMn_2X_4$ (thio)spinels is also confirmed by the spin density analysis, showing a spin magnetization per formula unit of $M_S = 4.00$ μ_B, see **Table 3.4**. At the Fermi energy, the spin up partially-occupied e_g band of Mn_B appears highly hybridized with the X p orbitals and with the Fe_A e and t_2 levels in the oxide and sulfide respectively, in agreement with the bigger atomic volume, enhancing orbital overlapping. The rest of the density of states is essentially the same as in the Cr-material, while in the Mn-based spinels the valence band is slightly shifted towards the Fermi energy and the Fe_A t_2 and e bands in the β channel of the spins appear more prominently. With the normal cation distribution, the bands of $FeMn_2S_4$ (**Figure 3.4** bottom-left panel), as in the case of $FeCr_2S_4$, are shifted towards the Fermi energy, except for the Mn_B t_{2g} and e_g bands in the α channel of the spins.

When $FeMn_2O_4$ is a completely inverse spinel ($x = 1$), the system becomes half-semiconductor with a negligible band-gap, which has also been found experimentally (Kulkarni and Darshane, 1985), see **Figure 3.4** top-right panel and also note in **Table 3.4** the integer $M_S = 4.00$ μ_B/f.u., typical of materials with band gaps. The partially-occupied and split Mn_{B1} e_g bands appear close to the Fermi energy in the majority channel of the spins, where the t_{2g} level, with a small contribution from the e_g level, in the conduction band is highly hybridized with the O p orbitals. The Mn_A t_2 and e levels

in the minority channel of the spins, are merged altogether and appear as a wide conduction band. In the inverse $FeMn_2S_4$ spinel, the bands are squeezed towards the Fermi energy, becoming a metal in both channels of the spins. The bands responsible for the conductivity properties are associated with the Mn_{B1} e_g level and with the Fe_{B2} t_{2g} level in the majority and minority channel of the spins respectively, see **Figure 3.4** bottom-rigth panel and the decimal M_S = 4.02 μ_B/f.u., typical of metals in **Table 3.4**. In general, we see that for any inversion degree, upon exchange of Cr by Mn cations, the bands responsible for the conduction properties are no longer the ones belonging to the atoms occupying the tetrahedral positions but those of $Mn_{B(1)}$.

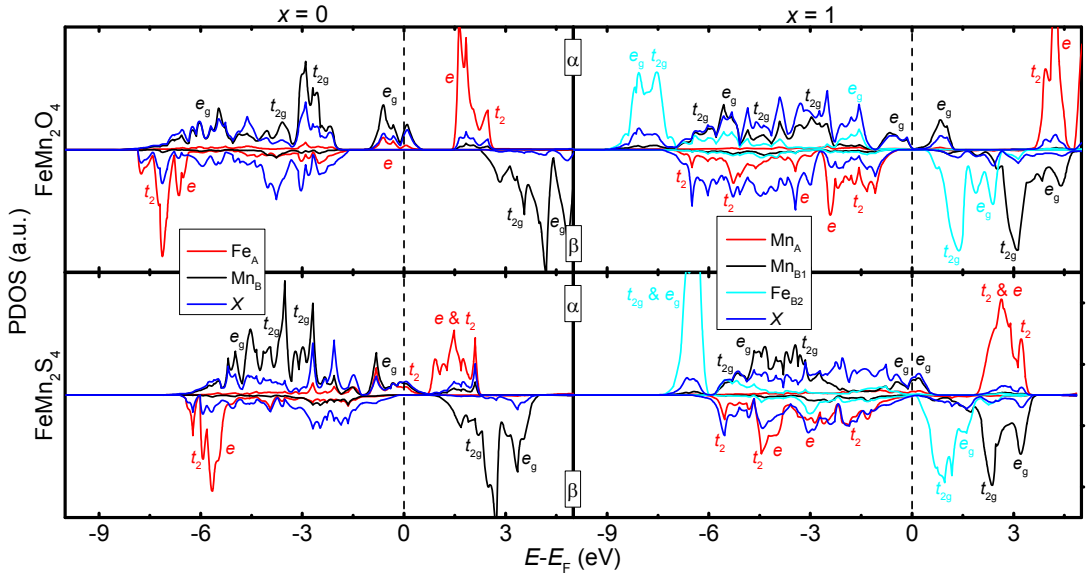

Figure 3.4. Atomic projections of the spin decomposed total density of states (PDOS) for $FeMn_2O_4$ and $FeMn_2S_4$. Fe and Mn contributions are from the 3*d* bands. O and S contributions are from the 2*p* and 3*p* orbitals respectively.

3.7.3 Fe_3X_4

The distribution of the bands in Fe_3O_4 and Fe_3S_4 are similar between them (see **Figure 3.5**). The Fe_B e_g bands in the majority spin channel appear at the low end energy of the valence band. Part of the Fe_B t_{2g} level in the conduction band and the minority spin channel is overlapped with the Fermi energy, giving the half-metallic properties to Fe_3O_4 (M_S = 4.00 μ_B), see **Table 3.4**. This supports the traditional explanation of electrons hopping from Fe^{2+} to Fe^{3+} in the octahedral sublattice, which renders all cations within this sublattice with the same charge and justifies the half-metallic properties of Fe_3O_4 (Zhang and Satpathy, 1991), which has led to its proposal for spintronic applications (Felser *et al.*, 2007). As a result of bands pushed towards E_F in Fe_3S_4, they overlap with the Fermi energy not only in the minority channel. In the majority spin, although weakly, S *p* orbitals also cross the E_F which are hybridized with the Fe_A *d* bands, giving the characteristic metallic decimal magnetization of saturation (M_S = 3.60 μ_B), **Table 3.4**. This result disagrees with previous of evidence of Fe_3S_4 having half-metallic (Devey *et al.*, 2009) or semiconducting (Vaughan and Tossell, 1981) properties.

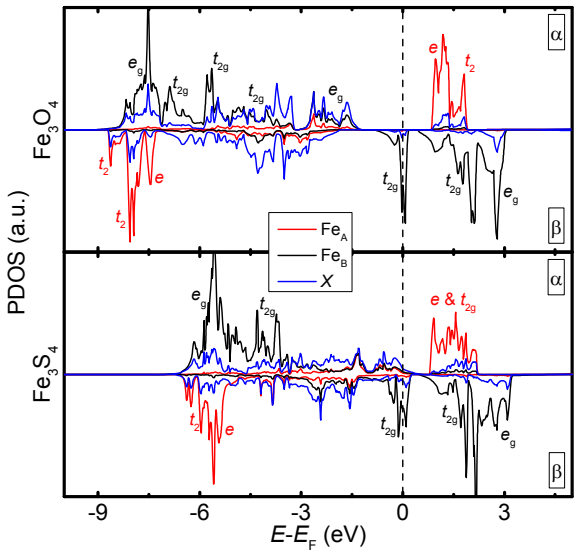

Figure 3.5. Atomic projections of the spin decomposed total density of states (PDOS) for Fe_3O_4 and Fe_3S_4. Fe contributions are from the 3 *d* bands. O and S contributions are from the 2*p* and 3*p* orbitals respectively.

3.7.4 $FeCo_2X_4$

When $FeCo_2O_4$ has a normal distribution, all the bands are pushed slightly towards the Fermi energy and especially those due to Co_B, see **Figure 3.6** top-left panel. As a result, the partially-occupied Co_B t_{2g} band that crosses the Fermi energy has a minimal band gap in the minority channel of the spins, making the normal $FeCo_2O_4$ spinel almost a half-metal, see also the integer value of the spin magnetization of saturation in **Table 3.4**. On the other hand, the sulfide counterpart has all the bands closer to the Fermi energy with symmetrical Co_B bands in the minority and majority spin channels (**Figure 3.6** bottom-left panel), due to the fully-occupied t_{2g} level which indicates non-magnetic behaviour for this atom (see **Table 3.4**). There is a peak at the Fermi energy,

in the majority spin channel, with contributions from the partially-occupied Fe_A *e* and Co_B e_g levels. In the minority spin channel, the normal $FeCo_2S_4$ spinel is weakly conducting, as there is a small Co_B fully-occupied t_{2g} band strongly hybridized with S *p* orbitals that ends shortly after the Fermi energy in the conduction band side. Overall, the sulfide counterpart is metallic which is confirmed by a decimal spin magnetization of saturation, **Table 3.4**.

When the Co-based (thio)spinels have an inverse cation distribution, all the bands are slightly pushed away from the Fermi energy compared to the normal cation distribution, especially in the oxide, see **Figure 3.6** right panels. Fe_{B2} *d* bands appear in the typical range described so far for both oxide and sulfide spinels. For the oxide, Co_A valence *d* bands are in both spin channels, while in the α spin channel the partially-occupied t_2 level appears exclusively in the conduction part. The fully-occupied Co_{B1} valence t_{2g} bands are nearly symmetrically placed in both spin channels, rendering this atom as non-magnetic, see m_S in **Table 3.4**. The inverse cation distribution of the oxide has insulating properties, see also M_S in **Table 3.4**. Although the sulfide counterpart has the Co_A and Co_{B1} bands symmetrically placed in both channels of the spins, the bands crossing the Fermi energy give it metallic properties (see the decimal value of the spin magnetization of saturation M_S = 2.46 μ_B/f.u. in **Table 3.4**, typical of metals). These properties are due to the hybridized partially-occupied Co_A t_2 and fully-occupied Co_{B1} t_{2g} levels and to the merged Co_A t_2, Co_{B1} t_{2g} and Fe_{B2} t_{2g} levels in the majority and minority channel of spins, respectively.

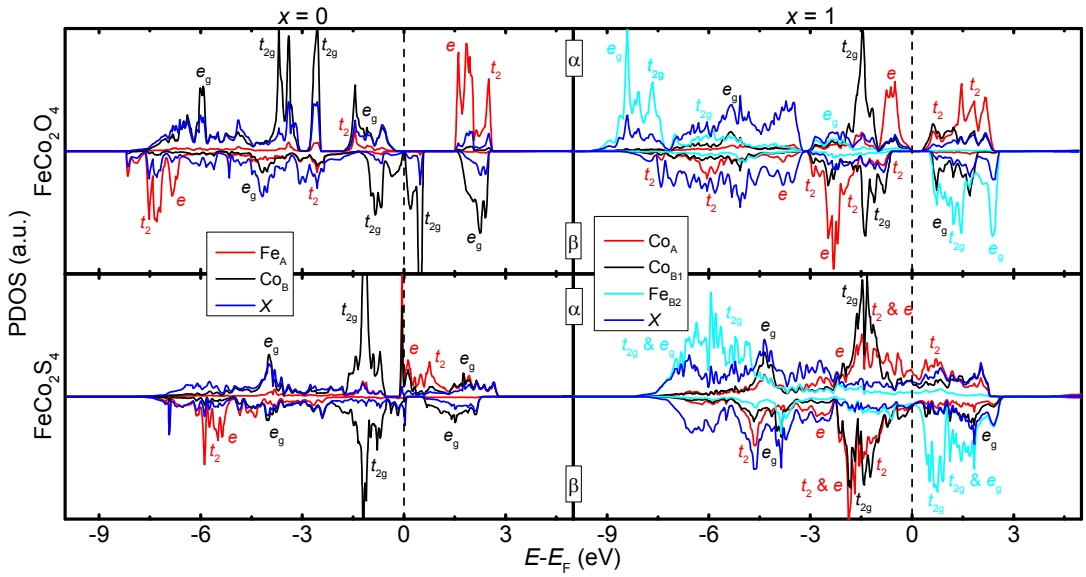

Figure 3.6. Atomic projections of the spin decomposed total density of states (PDOS) for $FeCo_2O_4$ and $FeCo_2S_4$. Fe and Co contributions are from the 3*d* bands. O and S contributions are from the 2*p* and 3*p* orbitals respectively.

3.7.5 $FeNi_2X_4$

For both Ni-based (thio)spinels, when $x = 0$, the bands' pattern is similar and follows the same distribution as described in previous cases, see **Figure 3.7** left panels. The oxide is half-metal due to a strong hybridization of the partially-occupied Ni_B e_g bands with the O *p* orbitals that cross the Fermi energy in the majority channel of the spins, see also the integer value of M_S in **Table 3.4**. The main difference between oxide and sulfide lies in the fact that bands in the latter are closer to the Fermi energy in both spin channels, thus becoming a metallic system. The thiospinel's metallic character is given by the S *p* orbitals with a small hybridization (only in the majority channel of

the spins) with the partially-occupied Fe_A *e* and t_{2g} levels bands, see the decimal M_S in **Table 3.4**.

When Ni is filling the A sublattice, the Ni-based spinel becomes half-semiconductor with a band gap of 0.20 and 2.05 eV in the majority and minority channels of the spins, respectively, see **Figure 3.7** top right panel. While the position and distribution of the bands due to the ions occupying different positions is equivalent to what we have presented in previous cases, for inverse $FeNi_2O_4$ spinel, nonetheless, this is not the case for the sulfide counterpart. In the inverse $FeNi_2S_4$ system, the Ni_A and Ni_{B1} ions are less magnetic than expected and the valence and conduction bands are merged together, making this compound metallic for any inversion degree. The inverse Ni-based (thio)spinels have integer values of M_S (see **Table 3.4**) regardless of whether they are insulator or metal. Note that in the case of the metal inverse $FeNi_2S_4$ spinel, the decimal number in $M_S = 4.00\ \mu_B$/f.u. is a special case. In $FeNi_2S_4$, for any inversion degree, the metallic character agrees with the experimental findings (Townsend *et al.*, 1977; Vaughan and Craig, 1985).

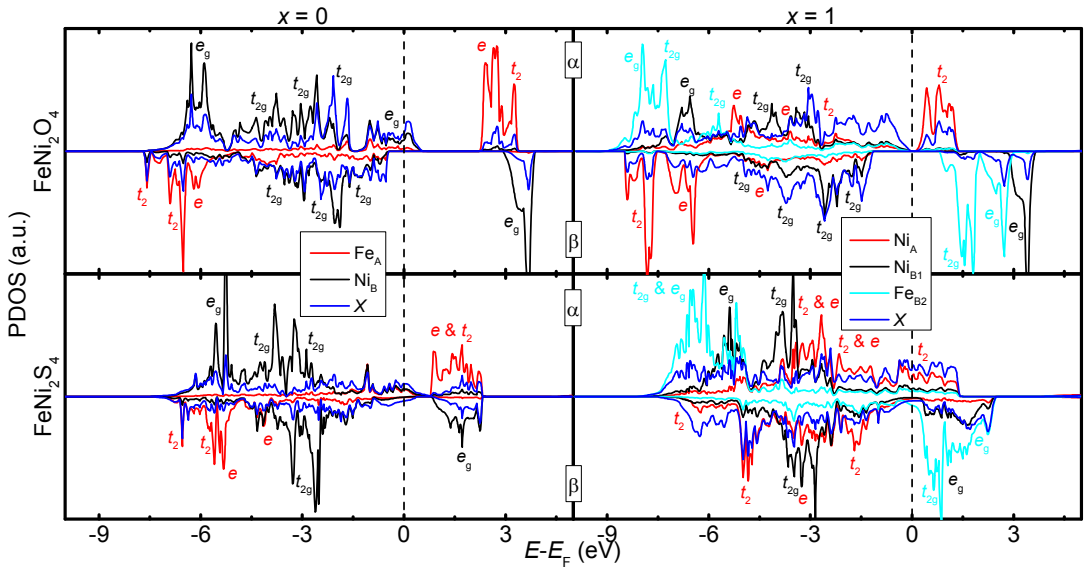

Figure 3.7. Atomic projections of the spin decomposed total density of states (PDOS) for $FeNi_2O_4$ and $FeNi_2S_4$. Fe and Ni contributions are from the 3*d* bands. O and S contributions are from the 2*p* and 3 *p* orbitals respectively.

3.8 Chapter conclusions

We have performed systematic electronic structure calculations for a series of (thio)spinels, which elucidate the cation distribution as well as the magnetic and electronic properties of these materials.

We have determined the thermodynamic inversion degree for the FeM_2X_4 (thio)spinels at temperatures used typically in their synthesis, which agrees reasonably well with available experimental evidence. More quantitative results could be expected if additional values of inversion degrees and different cations arrangements to those explored in this work are considered for the spinel compositions, although we do not expect this to change the trend of our results. We have found that FeM_2X_4 spinels are

more likely to have a normal distribution of cations when *M* is one of the two atoms to the left of Fe in the periodic table. $FeMn_2O_4$ has a metastable intermediate inversion degree that could only be found by considering entropic factors, which also agrees with experiment. It may be that the global minimum, *i.e.* the inverse spinel, is difficult to attain due to kinetic control. When *M* is one of the two atoms to the right of Fe in the periodic table, with the exception of $FeCo_2O_4$, the spinels have an intermediate inversion degree ranging between 10 to 50%. Finally, the oxidic spinel of Co and Fe has a completely inverse distribution of the cations. The small equilibrium inversion degree of $FeNi_2S_4$ agrees acceptably well with the one found in natural samples. Fitting the experimental spin magnetization of saturation of $FeNi_2X_4$ to the ones calculated for the normal and inverse structures gives inversion degrees with a similar trend to those calculated using thermodynamic arguments. This procedure could also be applied to $FeCo_2S_4$ and $FeNi_2O_4$ if the magnetizations of saturation are known experimentally.

No single factor among those analyzed, *i.e.* neither crystal field stabilization effects nor the size of the cations, can account by themselves for the equilibrium inversion degree.

For the two extreme scenarios, namely the completely normal and inverse spinels, we have calculated the electronic and magnetic properties of the metal atoms as well as the electronic properties of the bulk phase. We found that the majority of the spinels for any extreme inversion degree are half-metals in the ferrimagnetic state. Notable exceptions are the inverse Co and Ni oxide spinels, which are insulators, and their

sulfide counterparts that are metallic for any inversion degree, together with the inverse $FeMn_2S_4$. Notably, we found that hard anions stretch the band structure, giving the biggest band gaps and therefore the best half-metallic properties.

Finally, we have proposed a theoretical structure for $FeMn_2S_4$ and $FeCo_2S_4$ and have predicted their electronic and magnetic properties and equilibrium inversion degree.

4

Mechanical properties of magnetite

4.1 Introduction

Iron is the third most abundant element on the earth's surface and it is present as iron oxide minerals in nearly every type of rock and soil (Cornell and Schwertmann, 2003). These minerals have been known and used as a source of colouring agents (Hofmann, 1962; Middleton, 1987; Noll, 1980; Pomiès *et al.*, 1999; Rigby *et al.*, 1989) and metallic iron since ancient times and in the modern world they are used additionally as ores for the steel industry. It is estimated that currently more than 99 % of the total iron oxides mined worldwide are used in the iron and steel industry (Cornell and Schwertmann, 2003). Most of the iron oxide phases, in very small amounts, are also part of the biominerals in living organisms, where they are metabolic byproducts or have functions such as magnetotaxis, teeth hardening, navigation or iron storage (Addadi and Weiner, 1992; Bazylinski and Moskowitz, 1998; Frankel, 1991; Kirschvink *et al.*, 1985; Konhauser, 1998). Presently, for instance, as rocks containing iron oxides are weathered to form soils, iron is channelled into the global cycle of the elements (Cornell and Schwertmann, 2003). Oxides of iron occur frequently with Fe in different oxidation states, yielding various types of natural iron oxides. In general, iron oxide minerals display interesting magnetic and electrical properties, which are

strongly related to the stoichiometric ratio between Fe and O atoms and their crystalline structure. These minerals are classified according to their Fe:O ratio as wüsite ($0.83 < Fe:O < 0.95$), magnetite (Fe_3O_4) as well as the polymorph hematite α-, maghemite γ-, β- and ε- phases of Fe_2O_3.

Magnetite, together with hematite, is one of the most thermodynamically stable and therefore widely distributed iron oxide phases (Cornell and Schwertmann, 2003). Fe_3O_4 is formed as the final product in the mild reduction of akaganéite (β-FeOOH) (Blesa *et al.*, 1986) or hematite (Sapieszko and Matijević, 1980) with hydrazine or via combination in solution of lepidocrocite (γ-FeOOH) (Tamaura *et al.*, 1983) or ferrihydrite (Mann *et al.*, 1989; Sugimoto and Matijević, 1980) with Fe^{2+} ions, proceeding all the reactions through a dissolution-recrystallization mechanism. It is of significant research interest that Fe_3O_4 is a common inverse spinel mineral. Its cubic unit cell consists of eight Fe_3O_4 subunits with a lattice parameter of ~8.390 Å (Wright *et al.*, 2002). The inverse spinel arrangement is reflected by the formula $Fe^{3+}(Fe^{3+}Fe^{2+})O_4$, where there are two possible locations for the Fe ions: the tetrahedral sites, filled by Fe^{3+} ions, and the octahedral sites, where both Fe^{3+} and Fe^{2+} ions reside. The spins in tetrahedral and octahedral Fe are aligned antiparallel with respect to each other, indicating ferrimagnetic (Néel, 1948; Shull *et al.*, 1951) and half-metallic properties (Zhang and Satpathy, 1991). Fe_3O_4 magnetization of saturation, as well as the *Curie* temperature, have been reported to be 4.00 μ_B/f.u. (Zhang and Satpathy, 1991) and 858 K (Mulakaluri *et al.*, 2009; Pentcheva *et al.*, 2005) respectively for both natural and synthetic samples. In addition, the particle size is important for magnetism measurements, as it determines the contribution of the

external shell in relation to the bulk-core, where ultrafine magnetic particles produce superparamagnetic behaviour (Néel, 1954).

In this chapter, we have used DFT + *U* methodology to report intrinsic and mechanical properties of Fe_3O_4, including its elastic constants, and compared these with the same properties reported of Fe_3S_4. The elastic constants provide important information concerning the nature of the forces operating in the solids and form a link between mechanical and dynamical properties. These properties predict a more ionic character for Fe_3O_4 than for its isostructural sulfide counterpart Fe_3S_4. The results presented in this chapter have been published (Roldan *et al.*, 2013).

4.2 Computational details

We have used the VASP code to carry out spin-polarized calculations within the usual Kohn-Sham (KS) implementation of density functional theory (DFT) (Kresse and Furthmüller, 1996a, 1996b; Kresse and Hafner, 1994, 1993). The generalized gradient approximation (GGA) was employed with the PW91 functional (Perdew *et al.*, 1993, 1992), with the spin interpolation formula of Vosko *et al.* (1980) and long-range dispersion interactions correction via the semiempirical D2 method of Grimme (2006). The inner electrons consisting of orbitals up to, and including, the 3*p* levels for Fe and the 1s for O, were described by the projector augmented wave (PAW) method (Blöchl, 1994). KS valence states were expanded in a plane-wave basis set with a cut off at 520 eV for the kinetic energy. This high value ensured that no Pulay stresses occurred within the cell during relaxations. An energy threshold defining the self-consistency

of the electron density was set to 10^{-5} eV. In order to improve the convergence of the Brillouin-zone integrations, the partial occupancies were determined using the tetrahedron method with Blöchl corrections. The optimization of the structures was conducted via a conjugate gradients technique, which uses the total energy and the Hellmann-Feynman forces on the atoms, where in this chapter the break condition for the ionic relaxation loop was set at 0.01 eV/Å. Spin-orbit coupling was not considered as its influence is negligible on the atomic magnetic moments (Zhang *et al.*, 2012).

Within the VASP code, it is possible to assign an initial spin population and orientation at each atom, where the system will converge to the ground state spin configuration, but keeping the same orientation on the spins. Thus, the initial magnetic moment was described by a high spin ferrimagnetic distribution on both types of Fe. However, to describe the magnetic behaviour properly, an accurate treatment of the electron correlation in the localized *d*-Fe orbitals is crucial. Hence, we have used the Hubbard approximation (Anisimov *et al.*, 1992; Dudarev *et al.*, 1998) to improve the description of localized states in this type of system, where standard LDA and GGA functionals fail (Moreira *et al.*, 2002). The disadvantage of this approximation is the rather empirical character of the U_{eff} parameter choice, a feature that also appears when using hybrid functionals since the amount of Fock exchange is system-dependent (Ciofini *et al.*, 2004; Corà, 2005; Illas and Martin, 1998; Moreira *et al.*, 2002; Muñoz *et al.*, 2004). We fitted the U_{eff} *versus* the band gap in the low-symmetry unit cell of Fe_3O_4, below the Verwey temperature (Wright *et al.*, 2002), which presents some insulating character shown by a small band gap of ~0.14 eV (Chainani *et al.*, 1995; Park *et al.*, 1997, 1998). As we found that U_{eff} = 3.8 eV opens a band gap of 0.14 eV,

we have considered this value in the calculations of the 56 atoms high-symmetry unit cell.

Bulk calculations were carried out on a spinel cubic cell containing 56 atoms, of which 24 were Fe atoms and 32 were O atoms. All atoms were fully relaxed until the required accuracy was reached. Calculations were carried out in the reciprocal space of the cell and were described by a Monkhorst-Pack grid (Monkhorst and Pack, 1976) of $4\times4\times4$ Γ-centred *k*-points, which ensures the electronic and ionic convergence. Higher numbers of *k*-points were tested but these led to an energy difference of less than 0.01 eV.

The elastic tensors were determined using the standard finite difference technique, where the calculation of the second order elastic constants is achieved through the description of a linear elastic strain response of the material as it opposes to a certain stress. Each elastic constant (C_{ij}) is a component of a matrix, denoted by Voigt notation as subscript. We have derived each C_{ij} via the second-order Taylor expansion of the total energy with respect to the applied distortion, equation (4.1), where E is the total energy of the stressed cell, ε is the component of the applied strain and V is the equilibrium volume (Ainsworth *et al.*, 2011; Devey *et al.*, 2008).

$$C_{ij} = \frac{1}{V}\frac{\partial^2 E}{\partial\varepsilon_i \partial\varepsilon_j} \tag{4.1}$$

We have optimized both the lattice parameters and the internal atomic coordinates to avoid residual stresses, which is essential in the performance of an accurate comparison. The strain applied was up to ± 0.4 % of the cell parameter keeping a

constant volume as described by Ainsworth *et al.* (2011). Due to the crystal symmetry, the minimum linearly independent sets of strains to determine the elastic constants are two, leading to the C_{11}, C_{12} and C_{44} matrix components. For less symmetric crystals, such as orthorhombic, monoclinic or triclinic, space groups up to six sets need to be determined.

4.3 Structural properties

After geometry optimisation, the calculated cubic cell parameter for Fe_3O_4 is 8.390 Å while the experimental value is 8.390405 Å (Wright *et al.*, 2002). The optimized lattice parameter is in good agreement with the experiment considering that GGA functionals typically underestimate the structural properties of strongly correlated magnetic systems, such as metal oxides, due to the underestimation of exchange-splitting (Hafner, 2008). The mean distance between octahedral Fe and surrounding O atoms is $d(Fe_{Oh}\text{-}O)$ = 2.05 Å, which is slightly larger than for tetrahedral Fe $d(Fe_{Td}\text{-}O)$ = 1.89 Å, with both distances differing less than 0.01 Å from reported measurements (Fleet, 1982). As expected, both distances are shorter in magnetite than in its isostructural sulfide counterpart greigite, where the reported mean distances are $d(Fe_{Oh}\text{-}S)$ = 2.37 Å and $d(Fe_{Td}\text{-}S)$ = 2.18 Å (Roldan *et al.*, 2013). We carried out Bader analysis to obtain the arrangement of charge and spin densities along the unit cells, which, considering the electron delocalisation by using DFT, do not provide enough information to determine the electronic structure and supplementary techniques as density of states are required. Structural data of Fe_3O_4 and its isostructural sulfide

counterpart Fe_3S_4 is summarised on **Table 4.1**. We have also carried out a DFPerturbation theory (Wu *et al.*, 2005) calculation with fully relaxed cell vectors and ionic coordinates to obtain the phonon vibrations, where the 3N vibrational frequencies range between 674−142 cm^{-1} for Fe_3O_4 which are, as expected from more polar bonds, considerably higher than 385−59 cm^{-1} for its isostructural sulfide counterpart Fe_3S_4 (Roldan *et al.*, 2013).

Table 4.1. Summary of geometric and electronic properties of bulk Fe_3O_4. The properties listed are the mean value of the first-neighbours distance (d), the charge (q) and the spin densities (m_s). The minus sign in the spin density represents the antiparallel alignment in the ferrimagnetic spinels. Previously reported values of its isostructural sulfide counterpart greigite (Fe_3S_4) are shown for comparison.

	Fe_3O_4 bulk	Fe_3S_4 bulk[A]
$d(Fe_{Td})$ (Å)	1.890	2.180
$d(Fe_{Oh})$ (Å)	2.050	2.370
d(O/S) (Å)	2.010	2.323
$q(Fe_{Td})$ (e^-)	1.8	1.1
$q(Fe_{Oh})$ (e^-)	1.7	1.0
q(S) (e^-)	-1.3	-0.8
$m_s(Fe_{Td})$ (μ_B)	-4.0	-2.8
$m_s(Fe_{Oh})$ (μ_B)	3.9	3.0
m_s(O/S) (μ_B)	0.1	0.1

[A] Roldan *et al.* (2013)

4.4 Mechanical properties

An accurate experimental determination of elastic constants needs large pure single crystals that are difficult to obtain, and it is hence not surprising that there are relatively few reports about the mechanical properties of Fe_3O_4 available in the literature (Alexandrov and Ryzhova, 1961; Hearmon, 1984; Isida *et al.*, 1996; Moran and Lüthi, 1969; Reichmann and Jacobsen, 2004; Siratori and Kino, 1980). We have derived the elastic constants C_{11}, C_{12} and C_{44} of the Fe_3O_4 cubic cell. These elastic constants, summarised in **Table 4.2**, quantify the response of the crystal to external forces, and are related to macroscopic parameters obtained from an average of randomly oriented polycrystals.

The elastic constant C_{11} (and equivalent: C_{22} and C_{33}) measures the response of the cell to a pressure applied perpendicular to each cell face. C_{11} is calculated at 242 GPa for Fe_3O_4 (**Table 4.2**). The calculated value of C_{11} is clearly higher for Fe_3O_4 than for Fe_3S_4 (Roldan *et al.*, 2013), with the C_{11} of Fe_3O_4 fairly close to the accepted experimental value of 260.5 GPa (Reichmann and Jacobsen, 2004). This early result corroborates the suggestion that oxide is harder to compress than the sulfide. A distortion along two different axes leads to C_{12}, C_{21}, C_{23} and C_{32}, which are equivalent elastic constants. The calculated C_{12} for Fe_3O_4 differs less than 19 GPa from the experimental value (Reichmann and Jacobsen, 2004) while it is 118.1 GPa smaller than $C_{12}(Fe_3S_4)$ (Roldan *et al.*, 2013). For the last independent elastic constant, C_{44}, we obtain a value of 55 GPa for Fe_3O_4 which is just 16 GPa above $C_{44}(Fe_3S_4)$ (Roldan *et al.*, 2013). The calculated elastic constants for Fe_3O_4 compare well with the

experimental benchmark (Reichmann and Jacobsen, 2004) with a maximum discrepancy of 13 %.

Table 4.2. Physical properties of Fe_3O_4 derived from the elastic constants (C_{ij}): bulk modulus (B), shear modulus (G), B/G ratio, Young's modulus (Y), Poisson's ratio (σ) and anisotropy factor (A). The optimized lattice parameter of Fe_3O_4 is 8.390 Å. Previously reported Fe_3O_4 and Fe_3S_4 values are shown for comparison.

	Fe_3O_4	Fe_3O_4 (Experimental)	Fe_3S_4[B]
C_{11} (GPa)	242.3	260.5 ± 1.0[A]	104.7
C_{12} (GPa)	159.9	148.3 ± 3.0[A]	41.8
C_{44} (GPa)	55.0	63.3 ± 1.5[A]	39.0
B (GPa)	187.4	185.7 ± 3.0[A]	62.8
G (GPa)	49.5	60.3 ± 3.0[A]	36.0
B/G	3.8	3.1	1.7
Y (GPa)	136.5	163.5	90.6
σ	0.40	0.36	0.29
A	1.34	1.13	1.24

[A] Reichmann and Jacobsen (2004)

[B] Roldan *et al.* (2013)

We have calculated the Fe_3O_4 bulk and shear moduli by equating the uniform strain in the crystal aggregates to the external isostrain in the Voigt approximation (Voigt, 1928). Further, we have derived other elastic properties such as the Young's modulus, the Poisson's coefficient and the shear anisotropy factor (Wu and Hu, 2007). The elastic moduli, thus, are useful in predicting the structural stability of materials: the

bulk modulus (B), from equation (4.2), represents the resistance to fracture, while the shear modulus (G), equation (4.3), measures the resistance to a plastic deformation.

$$B = \frac{C_{11} + 2C_{12}}{3} \tag{4.2}$$

$$G = \frac{C_{11} - C_{12} + 3C_{44}}{5} \tag{4.3}$$

The calculated bulk modulus for Fe_3O_4 is 124.6 GPa, which is 62.8 GPa bigger than its sulfide analogue (Roldan *et al.*, 2013), whereas it differs by only 1.7 GPa from the reported value (Reichmann and Jacobsen, 2004). The shear modulus is also bigger in Fe_3O_4 than in the sulfide by 13.5 GPa (Roldan *et al.*, 2013). These values already depict a Fe_3O_4 less deformable than Fe_3S_4, which can also be explained by the relationship between B and G, which provides information about the material's fragility/ductility. A ratio of $B/G > 1.75$ is associated with ductility, whereas a lower value corresponds to a brittle material (Pugh, 1954). Given a B/G ratio of 3.8 for Fe_3O_4 (or 3.1 as derived from Reichmann and Jacobsen (2004)) and 1.74 for Fe_3S_4 (Roldan *et al.*, 2013), our calculations show that the anionic species in the iron spinels have a significant effect on their properties. Fe_3O_4 is softer but less liable to break or shatter compared to the same structure with sulfur as its anion, which is less ductile.

The Young's modulus and Poisson's ratio (equations (4.4) and (4.5) respectively) are characteristic properties of a material, related to its elasticity, and are often used to provide a measure of the stiffness of a solid.

$$Y = \frac{9BG}{3B + G} \tag{4.4}$$

$$\sigma = \frac{C_{12}}{C_{11} + C_{12}} \tag{4.5}$$

The Fe_3O_4 Young's modulus is bigger than the one of Fe_3S_4 by 45.9 GPa (Roldan *et al.*, 2013), showing that the Fe_3O_4 structure is less susceptible to physical changes than the sulfide, which is a metastable iron sulfide phase (Lennie *et al.*, 1997). Poisson's ratio (σ) measures the stability of the crystal to shear and provides more information about the interatomic forces than any other elastic property. A Poisson's ratio above 0.25 means that the interaction between atoms is mainly through central forces (with ionic character); whereas lower values indicate that large volume changes occur during uniaxial deformation. A Poisson's ratio below 0.1 is characteristic of covalent materials (Shein and Ivanovskii, 2008), this ratio is therefore a measure of bond-covalency. The values of $\sigma(Fe_3O_4) = 0.40$ and $\sigma(Fe_3S_4) = 0.29$ (Roldan *et al.*, 2013) show that the governing force between Fe−O atoms in Fe_3O_4 is more ionic than in greigite. This result is in full agreement with the little Fe−O orbital overlap observed in the density of states, see Chapter 3, indicating a lower degree of covalency in Fe_3O_4 compared to Fe_3S_4.

Elastic anisotropy (A) (equation (4.6)) of a crystal is correlated with the tendency of the material to form micro-cracks. While a perfectly isotropic crystal would have A = 1, we calculate a value $A(Fe_3O_4) = 1.34$, which is just 0.10 above the reported value of $A(Fe_3S_4)$ (Roldan *et al.*, 2013) indicating that Fe_3O_4 behaviour slightly depends more on the stress direction than Fe_3S_4.

$$A = \frac{2C_{44}}{C_{11} - C_{12}} \tag{4.6}$$

The overall description derived from the elastic properties is that magnetite is less liable to deformations than Fe_3S_4 (large elastic moduli and anisotropy values) and the forces between the ions are more localised in the oxide comparing with a softer anion such as in the sulfide greigite (large Poisson's ratio). As we have shown in Chapter 3, the present mechanical description agrees with the description derived from the electronic structure.

4.5 Chapter conclusions

In the present work, we have used the DFT + U approach (U_{eff} = 3.8 eV) to carry out a systematic study of the properties of magnetite (Fe_3O_4) and compare them with experiments and greigite (Fe_3S_4). The calculated first neighbour distances in the Fe_3O_4 material differ by less than 0.01 Å from previous reports. However, the average distance between the Fe and the corresponding anion is different enough (~0.3 Å) to provide a clear differentiation between the pure oxide and the sulfide compound, hardly distinguishable in synthetic samples. Furthermore, we have derived a number of mechanical properties from the independent elastic constants C_{11}, C_{12} and C_{44} corresponding to Fe_3O_4. The ratio of the bulk to shear moduli allowed us to evaluate the effect of the anionic species in the material, *i.e.* magnetite is harder than greigite, but less liable to fracture and Fe−O interaction has a more ionic character than Fe−S in the sulfide.

5

Structures, stabilities and redox behaviour of the major surfaces of Fe_3O_4

5.1 Introduction

Magnetite, Fe_3O_4, is of significant importance as the main component of industrial catalysts in, for example, the dehydrogenation of ethylbenzene (Weiss and Ranke, 2002) which is used as the primary feedstock for the production of 85% of commercial styrene (Chen and Updated by Staff, 2006; James and Castor, 2012). Fe_3O_4 is also used as a catalyst for the water gas shift (WGS) reaction, where molecular hydrogen is formed from carbon monoxide and water (Campbell *et al.*, 1970; Gonzalez *et al.*, 1986; Rethwisch *et al.*, 1985), the Fischer-Tropsch synthesis of hydrocarbons (Li *et al.*, 2001) and the Haber-Bosch process for the production of ammonia (Bond, 1974; Bridger and Snowden, 1970; Somorjai and Salmeron, 1986; Topham, 1985). The high stability and catalytic activity as well as its low cost make Fe_3O_4 the catalyst of choice for these heterogeneous processes (Cornell and Schwertmann, 2003). Furthermore, Fe_3O_4 is important in other applications, such as groundwater remediation (dos Santos Coelho *et al.*, 2008), and potentially in spintronic devices due to the conducting

properties of only one channel of spins (Roldan *et al.*, 2013; Zhang and Satpathy, 1991).

Above 120 K, Fe_3O_4 crystallizes in the spinel structure (Hill *et al.*, 1979) with space group $Fd\bar{3}m$ (cubic) (Wright *et al.*, 2002), but when cooled below that temperature, it undergoes a phase transition known as the Verwey transition, where the space group changes to $P2/m$ (monoclinic) (Wright *et al.*, 2002). Thus, at room temperature, Fe_3O_4 has the spinel face-centred cubic unit cell, on which we will focus in this chapter. In this structure, the oxygen ions are regularly close packed along the [111] direction, separating layers of Fe ions, which appear in two different alternate arrangements. One is composed of Fe ions occupying two types of positions (octahedral (Fe_B) and tetrahedral (Fe_A)) and the other one has only Fe_B, shown in the scheme in **Figure 5.1**. The experimental lattice constant for Fe_3O_4 is a = 8.390 Å (Wright *et al.*, 2002) and each unit cell is composed of eight formula units (four rhombohedral primitive cells). Unlike the rest of the iron oxides, Fe_3O_4 has Fe ions in mixed valence states, with the chemical formula often written as $Fe_A^{3+}\left[Fe^{2+}Fe^{3+}\right]_B O_4$, where A and B represent the tetrahedral and octahedral sites, respectively. The distribution where the 3+ cations occupy the A sites, while the B sites contain a mixture of 2+ and 3+ cations, is called *inverse* (in contrast with the *normal* spinel where the 2+ cations are all located in the A site).

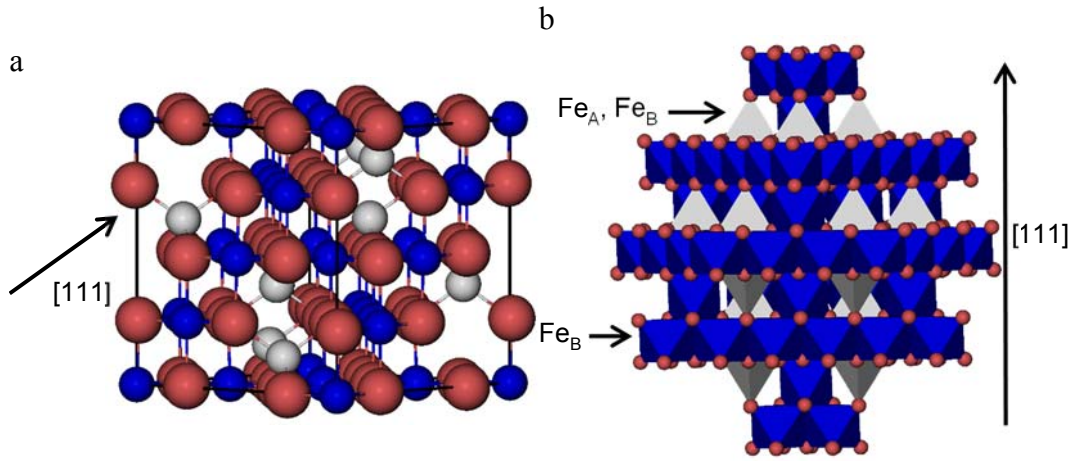

Figure 5.1. View of the bulk structure of Fe_3O_4: (a) ball and stick model of the cubic unit cell and (b) polyhedral model showing the alternating layers of Fe_B and Fe_A-Fe_B ions separated by O ions. Fe_A ions are in grey, Fe_B ions are in blue and O ions are in red.

Biological (Faivre and Schüler, 2008; Lins *et al.*, 2007), extra-terrestrial (Bradley *et al.*, 1996; McKay *et al.*, 1996) and synthetic (Faivre *et al.*, 2005; Zhao *et al.*, 2008) Fe_3O_4 crystals have been described by several authors. Among all the crystal habits in which this mineral has been found, the three most common are the octahedral morphology enclosed by (111) surfaces; a truncated octahedron by adding the (001) plane and as twinning on the (111) surface (Cornell and Schwertmann, 2003; Zhao *et al.*, 2008). Zhao *et al.* (2008) synthesized Fe_3O_4 under a systematic range of conditions using a polyol process, where the crystals obtained ranged from cubic, truncated octahedral to octahedral shapes, depending on pH.

The stacking sequence of the atomic planes perpendicular to the [001] direction can be represented as Fe_A-(O-Fe_B) (atoms inside brackets are within the same layer), leading in principle to two different bulk-like terminations for the (001) surface, which

are both polar. There are also two possible non-dipolar reconstructions of this surface, *i.e.* when the slab is terminated by either 0.5 mono layers (ML) Fe_A or 0.5 ML O-Fe_B in both the top and bottom surface. Experimentally, this surface has been found to have a $\left(\sqrt{2}\times\sqrt{2}\right)R45^{\circ}$ reconstruction for which different rationalizations have been given. Studies combining low-energy electron diffraction (LEED), X-ray photoelectron spectroscopy (XPS), X-ray photoelectron diffraction (XPD) and scanning tunnelling microscopy (STM) (Chambers *et al.*, 2000), as well as another work combining LEED with low-energy ion scattering (LEIS) (Mijiritskii and Boerma, 2001), have suggested a (001) surface terminated by the reconstructed non-dipolar 0.5 ML of Fe_A. On the other hand, a different study, combining STM, LEED, LEIS and XPS, has suggested a surface terminated by the reconstructed charge-compensated O-Fe_B with one oxygen vacancy per unit cell (Stanka *et al.*, 2000). Meanwhile, Voogt *et al.* (1999) were unable to differentiate them based on reflection high-energy electron diffraction (RHEED) and LEED, suggesting as possible terminations: the reconstructed non-dipolar 0.5 ML Fe_A layer or the reconstructed charge-compensated O-Fe_B layer with oxygen vacancies or hydroxyl groups (Voogt *et al.*, 1999). More recently, Parkinson *et al.* (2011) have identified experimentally, using STM and LEED images, that the (001) surface terminations are temperature dependent. The 0.5 ML O-Fe_B termination or one with *wavelike* structure and small defects, such as hydroxyl groups, is thermodynamically more stable at 923 K, while at lower temperatures (623 K) the surface terminated by 0.5 ML of Fe_A is observed, although some point-defects may stabilise other terminations (Parkinson *et al.*, 2011).

To date, most computational efforts have concentrated on explaining the stability of the bulk-like dipolar O-Fe_B termination, leaving largely ignored the reconstructed non-dipolar 0.5 ML Fe_A termination. Pentcheva *et al.* (2005) have studied the stability under varying redox conditions of one ideal and reconstructed stoichiometric (0.5 ML Fe_A) and several non-stoichiometric terminations using spin-polarised density functional theory (DFT) calculations. These authors found that the modified polar bulk-like O-Fe_B termination was the most stable for the whole range of chemical potential (Pentcheva *et al.*, 2005), which was validated by experimental X-rays diffraction (XRD) (Pentcheva *et al.*, 2005) and by the *wavelike* pattern along the [011] direction observed on experimental STM images (Fonin *et al.*, 2005). Further studies by Parkinson *et al.* (2012) of this surface termination using spin-polarized DFT + *U* calculations supported the Jahn-Teller distortion of this surface based on simulation of STM images of antiphase domain boundaries (APDBs) (Parkinson *et al.*, 2012).

In the [011] direction, Fe_3O_4 is composed of alternating layers of (Fe_A-Fe_B-O) and (Fe_B-O). After reconstruction, two non-dipolar terminations are possible: one terminated by the (Fe_B-O) layer with 0.25 ML Fe_A on top and another terminated by the (Fe_A-Fe_B-O) layer with 0.25 ML of Fe_A vacancies. Single crystal studies carried out on this surface, involving the use of STM, LEED, scanning tunnelling spectroscopy (STS) and Auger electron spectroscopy (AES), have found a one-dimensional reconstruction along the $[01\bar{1}]$ direction, which was concluded not to have a simple bulk iron-oxide termination (Jansen *et al.*, 1996, 1995). Subsequent studies, supported by atomically resolved STM (G. Maris *et al.*, 2006; Gabriela Maris

et al., 2006a, 2006b), suggested a model based on a surface terminated by a polar (Fe_A-Fe_B-O) bulk-like layer, in order to explain the atomic rows observed on the tops of ridges along the $[01\bar{1}]$ direction. However, the authors also left open the possibility of alternative models, including surface reconstruction, to interpret the STM images (G. Maris *et al.*, 2006).

The (111) surface is the dominant cleavage plane of Fe_3O_4, and the stacking of the atomic layers perpendicular to this surface is Fe_{A1}-Fe_{B1}-Fe_{A2}-O_1-Fe_{B2}-O_2. All of the six possible different bulk-like surface terminations are dipolar. Only two reconstructions lead to non-dipolar terminations, *i.e.* 0.5 ML Fe_{B1} or 0.5 ML Fe_{B2}. Several possible terminations have been described from LEED and STM results: one dipolar plane showing close packed features (due to 0.75 ML of Fe_{B2} and 0.25 ML of O_2 over a close packed O_1 layer) (Lennie *et al.*, 1996); a reconstructed non-dipolar honeycomb plane (due to 0.5 ML of Fe_{B1}), which was the most stable one (Lennie *et al.*, 1996); a reconstructed dipolar 0.25 ML Fe_{A1} plane (Ritter and Weiss, 1999); as well as a regular bulk-like dipolar Fe_{A1} termination and an intermediate case between the former two, which were obtained as a function of the annealing temperature (Berdunov *et al.*, 2004a). Again, most of the computational studies have been directed towards the dipolar bulk-like terminations of the (111) surface. Martin *et al.* (2009) used spin-polarized DFT calculations to study the dipolar non-stoichioimetric bulk-like Fe_{B1} and Fe_{A1} terminations of the (111) surface and they found Fe_{B1} to be the more stable of the two, which they validated through comparison with experimental STM images (Martin *et al.*, 2009). Berdunov *et al.* (2004b) used DFT to study the dipolar

non-stoichiometric bulk-like O_2 termination of the (111) surface which was also validated via comparison with experimental STM images (Berdunov *et al.*, 2004b). Kiejna *et al.* (2012) studied the non-stoichiometric bulk-like dipolar terminations of the (111) surface using DFT + *U*, and although they did not calculate the stoichiometric slab, they predicted the Fe_{A1} termination as the most stable for the whole range of chemical potential they considered (Kiejna *et al.*, 2012). Reduced surfaces of the Fe_3O_4(111) surface show superstructures with $Fe_{1-x}O$(111) islands (Condon *et al.*, 1997), which makes the surface even richer in possible terminations.

Following the seminal work by Tasker (1979) on the surface properties of ionic solids, in this chapter we have used DFT + *U* to investigate the non-dipolar stoichiometric terminations of the low Miller index surfaces of Fe_3O_4, in order to complement previous experimental and computational studies. We report the equilibrium morphology of the crystals enclosed by stoichiometric non-dipolar surfaces and the factors that govern the redox properties of the most common surfaces, (001) and (111), which are also the most prominent surfaces of Fe_3O_4 moieties (Gaines *et al.*, 1997; Kostov, 1968). We have also calculated the STM images of the different stoichiometric non-dipolar terminations of these surfaces to determine the most likely to appear in nanocrystals through comparisons with available experimental STM data. We have studied the redox processes by the systematic formation of single O vacancies and the adsorption of single O on the surface, as opposed to previous computational studies which have focused on bulk-like terminations and their modifications. This approach allows us to explore how these redox processes determine the surface

properties by finely tuning the conditions of temperature and oxygen partial pressure on the stoichiometric non-dipolar surfaces. The results presented in this chapter have been published (Santos-Carballal *et al.*, 2014).

5.2 Computational methods

5.2.1 Calculation details

We have used the Vienna *Ab-initio* Simulation Package (VASP) (Kresse and Furthmüller, 1996a, 1996b; Kresse and Hafner, 1994, 1993) to carry out quantum mechanical calculations within the usual Kohn-Sham (KS) implementation of DFT. The Perdew-Burke-Ernzerhof (PBE) (Perdew *et al.*, 1997, 1996a) version of the generalized gradient approximation (GGA) was employed as the exchange-correlation potential, together with the semiempirical method D2 of Grimme (2006) to model the long-range dispersion interactions. The core electrons, up to and including the 3*p* levels of Fe and the 1*s* of O, were frozen and their interaction with the valence electrons was described by the projector augmented wave (PAW) method (Blöchl, 1994; Kresse and Joubert, 1999). KS valence states were expanded in a plane-wave basis set with a cutoff of 400 eV for the kinetic energy. An energy threshold-defining self-consistency of the electron density was set to 10^{-5} eV and the optimization of the structures was conducted via a conjugate gradients technique, which stops when the Hellmann-Feynman forces on all atoms are less than 0.01 $\mathrm{eV \cdot Å^{-1}}$.

All calculations were spin-polarised, but spin-orbit coupling was not considered. Within the VASP code, it is possible to assign an initial spin population and orientation to each atom of the system, to converge to a particular spin configuration. Thus, the initial magnetic moments were set following a high-spin ferrimagnetic structure, *i.e.* with opposite spins in the tetrahedral and octahedral sites, in agreement with experiment (Néel, 1948; Shull *et al.*, 1951). In order to describe the electronic and magnetic behaviour properly, an accurate treatment of the electron correlation in the localized *d*-Fe orbitals is crucial. Hence, we have used the Dudarev *et al.* (1998) approach within the DFT + *U* (Anisimov *et al.*, 1992) for improving the description of these localized states. This is a correction typically used where standard LDA and GGA functionals fail to describe the electronic structure properly (Moreira *et al.*, 2002). The value for the on-site Coulomb interaction term in this study was U_{eff} = 3.7 eV, which was obtained following the procedure described in Chapter 4 but adjusted to a different DFT functional. The limitation of this approximation is the difficulty in choosing an adequate value for the U_{eff} parameter, which is usually property dependent (Grau-Crespo *et al.*, 2006a; Loschen *et al.*, 2007; Wang *et al.*, 2006). An alternative computational approach is the use of hybrid functionals, although in that case the calculated properties also depend on the fraction of the exact Hartree-Fock exchange that is added to the DFT exchange term (Ciofini *et al.*, 2004; Corà, 2005; Illas and Martin, 1998; Moreira *et al.*, 2002; Muñoz *et al.*, 2004), and the calculations are too computationally expensive to be applied to the large surface models employed in this study.

Bulk calculations were performed using the rhombohedral primitive unit cell containing 14 atoms (Fe_6O_8). Integrations in the reciprocal space were performed using a Monkhorst-Pack grid of $7\times7\times7$ Γ-centred *k*-points (Baldereschi, 1973; Chadi and Cohen, 1973; Monkhorst and Pack, 1976), which ensured electronic and ionic convergence. Test calculations with a higher number of *k*-points led to an energy difference smaller than 1 meV per cell. *k*-point grids for the surface calculations were chosen in such a way that a similar spacing of points in the reciprocal space was maintained.

Within this setup, we calculated a lattice constant for the bulk Fe_3O_4 unit cell of a = 8.398 Å, in excellent agreement with the experimental value of 8.390 Å (Wright *et al.*, 2002), and an equilibrium volume of V = 74.043 Å^3 per formula unit. The calculated total spin magnetization per formula unit, M_S = 4.00 μ_B lies very close to the 4.05 μ_B, measured experimentally at 4.2 K (Kąkol and Honig, 1989), and the atomic spin moments, $m_s(\mathrm{Fe_A}) = -4.03\mu_B$, $m_s(\mathrm{Fe_B}) = 3.91\mu_B$ and $m_s(\mathrm{O}) = 0.06\mu_B$ have the ferromagnetic orientation observed before (Roldan *et al.*, 2013; Shull *et al.*, 1951), following very closely the Néel model (Néel, 1948), where the electronic configurations are $e_\uparrow^2 t_{2\uparrow}^3$ for Fe_A and $t_{2g\uparrow}^3 t_{2g\downarrow}^1 e_{g\uparrow}^2$ as well as $t_{2g\uparrow}^3 e_{g\uparrow}^2$ for Fe_B. Calculated charges for Fe_A, Fe_B and O atoms are 1.59, 1.52 and −1.16 e^- respectively.

5.2.2 Surface models

In order to build slab models of the Fe_3O_4 surfaces, two models are used in the literature to explain the reconstructions found in polar surface terminations: the

electron-counting (Pashley, 1989) and the dipole method (Tasker, 1979). Both models are based on the condition that the net surface charge or dipole perpendicular to the surface, respectively, must be zero.

A surface structure satisfies the model of electron-counting (*i.e.*, it is charge- or auto-compensated) if all the partially filled dangling bonds in the cations are empty and the partially filled dangling bonds in the anions are full. It assumes that the atomic orbitals are in the conduction or valence band respectively. To achieve this, the model postulates that a stable surface structure will be the one that (after reconstruction) is able to accommodate exactly all the electrons of the partially filled orbitals of the cations (in the conduction band) into the partially filled orbitals of the anions (valence band). However, the disadvantage of this approach is that this condition directly links to the conducting properties of the material under investigation. If the surface satisfies this model, it will be a semi-conductor; otherwise the remnant electrons will lead to a metallic surface.

The dipole method for reconstructing dipolar surfaces is a more robust option, at least with half-metallic materials like Fe_3O_4 (Roldan *et al.*, 2013), because it is not connected to the conducting properties of the structure. This method, pioneered by Tasker (1979), considers the crystal as a stack of planes, where three possibilities can arise. In type 1, each plane has overall zero charge because it is composed of anions and cations in stoichiometric ratio which makes it non-dipolar, whereas in type 2 the stacking of three symmetrically charged planes cancels out the dipole moment perpendicular to the surface. In type 1 and 2, no reconstruction of the surface is needed

because the repeat unit is non-dipolar perpendicular to the surface. However, in type 3 surfaces, alternating charged planes stack in a sequence that produces a dipole moment perpendicular to the surface, but the surface can be reconstructed through moving half of the ions with the same charge from the top to the bottom of the slab. This method also guarantees that the surface does not generate an electrical field within the crystal and therefore the potential felt at each ion site reaches the constant bulk value, a condition that is not necessarily satisfied by the electron-counting model.

All the surfaces in this study were created by cutting the geometry optimised bulk using the dipole method implemented in METADISE (Watson *et al.*, 1996). The resulting slabs are represented by keeping fixed the bottom atoms at their *ab-initio* relaxed bulk positions to simulate the bulk phase of Fe_3O_4 and by relaxing the rest of the slab during the optimization, giving a single relaxed surface. The slabs comprise 56 atoms (8 formula units), with 24 Fe and 32 O atoms. The Fe_3O_4 (001), (011) and (111) surfaces were modelled with slabs having surface areas of 70.5, 99.7 and 61.1 $Å^2$, respectively, and they were constructed of 9, 5 and 13 atomic layers, respectively. **Figures 5.2, 5.3 and 5.4 (c)** provide a representation of their stacking sequence in each direction. For the (001) and (111) surfaces, the simulation slabs were symmetrical along the *z* axis. Top species in the (001) surface were (0.5 ML) Fe_A atom and 2 Fe_B and 4 O atoms (equivalent to 0.5 ML for each of the ions) for terminations A and B respectively, see **Figure 5.2**. For the (111) surface, terminations A and B were terminated by half of the $(Fe_B)_6$ and $(Fe_B)_2$ bulk layers respectively. However, the simulation slabs for the (011) surface were asymmetrical along the *z* axis, with

complementary top and bottom layers. Top layer of termination A was a single (0.25 ML) Fe_A atom above a bulk-like O-Fe_B layer, while its bottom layer was a bulk-like Fe_A-Fe_B-O layer with one (0.25 ML) Fe_A vacancy. For termination B, top and bottom layers were the other way round.

In every simulation cell, a vacuum region of 12 Å was added perpendicular to the surface to avoid interaction between the periodic slabs. Different slab and vacuum thicknesses as well as numbers of relaxed layers were tested until convergence within 1 meV per cell was achieved. Since we are going to remove and add O atoms to the surfaces at one side of the slab only, we applied dipole corrections perpendicular to all surfaces in the calculations to enhance the electronic convergence (Makov and Payne, 1995; Neugebauer and Scheffler, 1992). We have used Bader analysis (Bader, 1990) in the implementation of Henkelman and co-workers (Henkelman *et al.*, 2006; Sanville *et al.*, 2007; Tang *et al.*, 2009) to analyse the charge transfer around the defects introduced in the stoichiometric surfaces. We have chosen this methodology for partitioning atomic charges, as it is based upon the charge density, which is insensitive to the metal oxidation state and the basis set used, unlike wavefunction-based population schemes (Ángyán *et al.*, 1994; De Proft *et al.*, 2002; Wiberg and Rablen, 1993).

5.2.3 Calculation of surface energies

We have carried out energy minimisations of the (001), (011) and (111) slabs to obtain their surface energies. We derived the surface energy of the unrelaxed surface (γ_u)

from a single point calculation of the pristine symmetric stoichiometric slab before relaxation, via equation:

$$\gamma_{\mathrm{u}} = \frac{E_{\mathrm{slab,u}} - E_{\mathrm{bulk}}}{2A} \tag{5.1}$$

where $E_{\mathrm{slab,u}}$ is the total energy of the unrelaxed slab, E_{bulk} is the energy of the bulk containing the same number of formula units as in the slab and A is the surface area of one side of the slab. During relaxation, the top surface was allowed to relax and the bottom one was kept fixed. As this slab model does not provide an isolated relaxed surface and both sides of the symmetric stoichiometric slabs are considered in the calculation of the energy, their surface energies (γ_{r}) and (γ_{u}), for the relaxed and unrelaxed sides respectively, are related by equation (5.2), where $E_{\mathrm{slab,r}}$ is the slab total energy after relaxation.

$$\gamma_{\mathrm{r}} + \gamma_{\mathrm{u}} = \frac{E_{\mathrm{slab,r}} - E_{\mathrm{bulk}}}{A} \tag{5.2}$$

At this point it is also worth noting that equations (5.1) and (5.2) are only useful for calculating the average surface energy of terminations A and B of (011), as the slabs are asymmetric and complementary. The cleavage energy ($E_{\mathrm{clev}} = 2 \cdot \gamma_{\mathrm{r}}$) is thus related to the energy required to create both top and bottom surfaces of the slab.

We have also calculated the degree of relaxation of each surface as a percentage (for (011) $\gamma_{\mathrm{r}} \sim E_{\mathrm{clev}}/2$):

$$\text{Relaxation} = \frac{\gamma_u - \gamma_r}{\gamma_u} \cdot 100 \quad (5.3)$$

The equilibrium morphology of a Fe_3O_4 crystal is determined by the surface free energies and the related growth rates of the various surfaces, which provides a measure of the relative stabilities of the surfaces. The morphology is constructed according to Wulff's theorem (Wulff, 1901), where the distance from the centre of the particle to the surface is proportional to the surface energy. It is based on the Gibbs approach (Gibbs, 1928), who proposed that under thermodynamic control the equilibrium form of a crystal should possess minimal total surface free energy for a given volume. Previous studies have shown (Cooper and de Leeuw, 2006; de Leeuw and Cooper, 2007) that using surface energies to calculate crystal morphologies provides good agreement with experiment as the difference in entropy between bulk and surface is small.

5.2.4 Redox processes of the (001) and (111) surfaces

We have also examined the redox properties of the most common Fe_3O_4 surfaces, the (001) and (111), by removing or adding O atoms to form non-stoichiometric compositions of the top atomic layer. We have based the discussion of the stabilities of the non-stoichiometric terminations on the *ab-initio* thermodynamics formalism (Wang *et al.*, 1998) where the surface free energy (σ) is calculated according to the equation:

$$\sigma(T,p) = \gamma_{\mathrm{r}} + \Delta\sigma(T,p)$$
$$\Delta\sigma(T,p) = \frac{E_{\mathrm{slab,r}}^{\Gamma_{\mathrm{O}}\neq 0} - E_{\mathrm{slab,r}}^{\Gamma_{\mathrm{O}}=0}}{A} - \frac{\Gamma_{\mathrm{O}}}{A}\cdot\mu_{\mathrm{O}} \tag{5.4}$$

where $\Delta\sigma(T,p)$ is the difference between the surface energy of the stoichiometric surface and the surface free energy of the non-stoichiometric plane and Γ_{O} is the excess of O ions at the top surface of the slab expressed in equation (5.5) (N_{O} and N_{Fe} are the number of O and Fe ions in the slab model respectively).

$$\Gamma_{\mathrm{O}} = N_{\mathrm{O}} - \frac{4}{3}N_{\mathrm{Fe}} \tag{5.5}$$

It is possible to express the chemical potential of molecular O_2 (μ_{O}) in the gas phase as:

$$\mu_{\mathrm{O}}(T,p) = \frac{1}{2}\left(E_{\mathrm{O_2}} + \Delta g_{\mathrm{O_2}}(T,p_0) + k_{\mathrm{B}}T\ln\frac{p}{p_0} \right) \tag{5.6}$$

Here the first term within the bracket is the DFT energy of the O_2 molecule. The second term is the difference in the Gibbs free energy per O_2 molecule at p_0 = 1 bar between 0 K and T, which in this study has been extracted from thermodynamic tables (Chase, 1998) to avoid its calculation in the gas phase (Grau-Crespo *et al.*, 2007; Reuter and Scheffler, 2001). The last term represents the change in free energy of the O_2 gas (assuming ideal gas behaviour) at constant temperature (T) when its partial pressure changes from p_0 to p.

We express μ_O with respect to half the energy of the O_2 molecule. The above convention makes μ_O a function of only experimental quantities. For consistency in the evaluation of the slab energies, we must subtract half of the energy of the O_2 molecule for each O atom in the slab. Expressing μ_O as described, it is possible to plot the surface free energies given by equation (5.4) for different surface compositions as a function of μ_O, and discuss the redox behaviour of the surface (Grau-Crespo *et al.*, 2007; Reuter and Scheffler, 2001).

Finally, for the calculation of the energy required to create an O atom vacancy or to add the atom on the surfaces, we need the energy of the O_2 molecule. However, it is known that GGA calculations fail in the description of the binding energy for this particular molecule, as is shown in the (over)binding of the O_2 molecule (Perdew *et al.*, 1996a).

According to our calculations, the O_2 triplet ground state has an equilibrium bond length of 1.23 Å and a binding energy of −6.08 eV (with respect to triplet oxygen atoms), comparing well with previous computational studies (Grau-Crespo *et al.*, 2006b; Mellan and Grau-Crespo, 2012; Wang *et al.*, 2006). However, this value lies 0.91 eV below the experimental binding energy (−5.17 eV) (Haynes, 2012). Therefore, we have considered that half of the over-binding of the O_2 molecule, 0.46 eV, will be added to correct the adsorption or vacancy formation energies with respect to one O atom. The redox processes in the following sections are all reported with respect to the corrected value.

5.2.5 Calculation of scanning tunnelling microscopy (STM) images

The STM images were simulated according to the basic formulation of the Tersoff-Hamann approach (Tersoff and Hamann, 1985) where the STM tip was approximated to an infinitely small point source. The tunnelling current between the surface and the tip in the STM experiments is proportional to the local density of the states (LDOS) integrated between the Fermi energy and the sample bias. We have used the program HIVE (Vanpoucke and Brocks, 2008) for the production of our STM topographic images, where the DFT-based partial charge density was integrated from −2.5 eV to the Fermi energy. In the constant current mode, the tip of the STM is moved across the surface where its height varies to keep the charge density at a constant value, which is given by a constant LDOS. We map the simulated STM images by means of the heights as a function of the position of the tip over the surface. More details about the method can be found elsewhere (Irrera *et al.*, 2013).

5.3 Stoichiometric surfaces

We have modelled different terminations of the three lowest Miller index surfaces of Fe_3O_4, shown in **Figures 5.2, 5.3 and 5.4**, whereas **Table 5.1** summarises their surface energies before and after energy minimization. Before relaxation, the order of increasing surface energies, and therefore decreasing stability, is (001) < (111) < (011), which remains the same after relaxation. Note that this order was established by taking into account only the most stable termination (with lowest γ) per surface, as these terminations would be the most likely to appear for each plane.

Table 5.1. Calculated surface energies before (γ_u) and after (γ_r) relaxation for the different terminations of the three lowest Miller index surfaces of Fe_3O_4.

Surface	γ_u ($J \cdot m^{-2}$)	γ_r ($J \cdot m^{-2}$)	Relaxation (%)
(001) termination A	1.45	0.96	34.2
(001) termination B	3.28	2.17	33.9
(011) terminations A and B*	2.13	1.37	35.5
(111) termination A	2.75	1.09	60.3
(111) termination B	1.58	1.10	30.4

* Note that for the (011) surface it is only possible to report the average surface energy, as terminations A and B are complementary.

Before geometry optimisation, termination A of the (001) slab was terminated by 0.5 ML of 2-coordinated Fe_A ions occupying a bridge site (above two O ions) with a $\left(\sqrt{2}\times\sqrt{2}\right)R45°$ symmetry according to Wood's notation (Wood, 1964), which is a vectorial description of the surface structure. Beneath the surface, the slab shows a bulk structure consisting of single rows in the [110] direction of 5-coordinated Fe_B ions alternating every two single rows of O ions with cubic packing, see **Figure 5.2**. During energy minimization, the protruding Fe_A ions move 0.53 Å towards the bulk, *i.e.* they experienced ~50 % inward relaxation based on ~1.05 Å as the layer interspacing, thereby becoming closer to the nearest two O (0.25 ML of the 2nd layer), which displace 0.35 Å to the surface to accommodate this relaxation, see **Table 5.2**. The relaxation pattern of the top atomic layer of the surface slab agrees semi-quantitatively with the ~40 % inward relaxation reported for the topmost layer of this

termination based on LEIS analysis (Mijiritskii and Boerma, 2001), which is generally regarded to fit better than the more complex relaxation pattern reported before for this surface termination by Chambers *et al.* (2000). Previous studies, purely theoretical (Rustad *et al.*, 1999) or combined with experiments (Spiridis *et al.*, 2006), have concluded that the Fe_3O_4(001) surface terminates with Fe ion dimers with $\left(\sqrt{2}\times\sqrt{2}\right)R45°$ symmetry. The second Fe may migrate from a sub-surface layer (Rustad *et al.*, 1999) or from a dipolar bulk-like Fe_A terminated (001) surface (Spiridis *et al.*, 2006). However, we have not included dimers here as this lies outside the scope of the present study. The surface energy of termination B of the (001) surface is also reported in **Table 5.1**, but we do not consider this plane for further analysis because of its high surface energy, which makes it very unlikely to appear in the Fe_3O_4 crystal morphology.

Table 5.2. Perpendicular movement (Δd_z) of the Fe_3O_4 surface species on the most stable (001) termination after relaxation. Note that a negative value indicates a movement towards the bulk. Distances are given in Å.

(001) termination A		
layer	**Species**	**Δd_z**
1st	Fe_A	−0.53
2nd	O 0.50 ML	0.02
	Fe_B	−0.05
	O 0.25 ML	0.35
	O 0.25 ML	−0.08
3rd	Fe_A	0.11
4th	O	−0.03
	Fe_B	0.03
	O	0.05
5th	Fe_A	−0.01
Blulk		

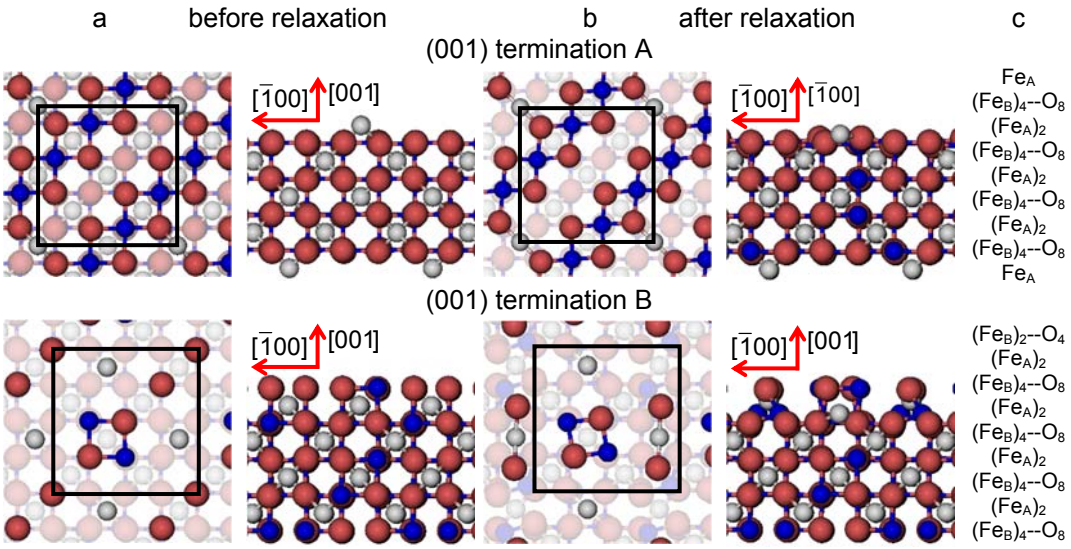

Figure 5.2. Top and side view of the simulation slabs for terminations A and B of Fe_3O_4(001) surface. The surfaces are shown (column a) before, (column b) after relaxation and (column c) their stacking sequence. For the colour code see **Figure 5.1**. Layers with atoms with dangling bonds are highlighted. The crystallographic direction for the top view of (001) surface terminations is [100] for the abscissae towards the right.

The stacking sequence of the Fe_3O_4(011) surface is shown in **Figure 5.3** and the vertical shifts of the ions towards the vacuum after energy minimization are listed in **Table 5.3**. One of the two lowest energy surface terminations, termination A, terminates with 0.25 ML of mono-coordinated Fe_A at the surface, followed by a bulk-like structure consisting of single rows of 4-coordinated Fe_B ions shifted 25% in the $[01\bar{1}]$ direction and alternating with single rows of O ions with cubic packing. During energy minimisation, the protruding Fe_A ions move 0.98 Å towards the bulk, thereby compressing the surface layer atoms underneath which move horizontally to accommodate this relaxation. Termination B has essentially the same relaxed surface

energy as termination A but it differs in its structure. It is terminated with a bulk-like structure consisting of a single row of 4-coordinated Fe_B ions between two rows of O ions. The latter O atoms are in cubic packing and alternate with double rows of 3-coordinated Fe_A ions in rhombohedral packing along the $[01\bar{1}]$ direction. The double row of Fe_A ions is partially vacant by 0.25 ML with $p(1\times2)$ symmetry. During energy minimization, the top Fe_A and Fe_B ions shift towards the bulk by 0.27 Å and 0.11 Å respectively which generates a 0.23 Å movement towards the surface of the Fe_B ions in the sub-surface layer. Based on the similarity between the relaxed structure of termination B, differing only by 0.25 ML Fe_A vacancy from the bulk-like Fe_A-Fe_B-O termination proposed in ref 34, we can still compare some structural characteristics between them. The calculated Fe_B-Fe_B or O-O distance of the atoms lying in the same row along the $[01\bar{1}]$ direction is 2.77 Å in termination B, which agrees well with their reported 3.0 ± 0.3 Å (G. Maris *et al.*, 2006). Moreover, along the [001] direction, the calculated Fe_B-O distance of 1.92 Å also compares well with 2.1 ± 0.3 Å from STM experiments (G. Maris *et al.*, 2006).

Table 5.3. Perpendicular movement (Δd_z) of the Fe_3O_4 surface species on the most stable (011) terminations after relaxation. Note that a negative value indicates a movement towards the bulk. Distances are given in Å.

(011) termination A			(011) termination B		
layer	**Species**	**Δd_z**	**layer**	**Species**	**Δd_z**
1st	Fe_A	−0.98		Fe_A	−0.27
	O	−0.02	1st	Fe_B	−0.11
2nd	Fe_B	−0.11		O	0.08
	O	−0.03		O	−0.06
	Fe_A	−0.04	2nd	Fe_B	0.23
3rd	Fe_B	0.06		O	−0.04
	O	0.01		Fe_A	0.02
			3rd	Fe_B	0.00
	Bulk			O	0.00
				Bulk	

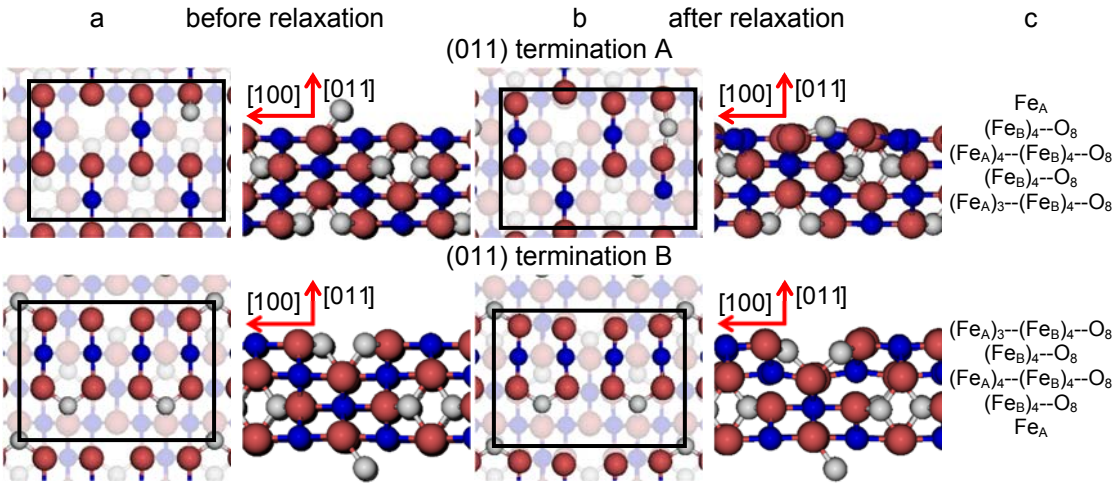

Figure 5.3. Top and side view of the simulation slabs for terminations A and B of $Fe_3O_4(011)$ surface. The surfaces are shown (column a) before, (column b) after relaxation and (column c) their stacking sequence. For the colour code see **Figure 5.1**. Layers with atoms with dangling bonds are highlighted. The crystallographic direction for the top view of (011) surface terminations is $[0\,\bar{1}\,1]$ for the abscissae towards the right.

Finally, the bottom two panels of **Figure 5.4** represent the stacking sequence of the $Fe_3O_4(111)$ surface terminations, while the vertical displacement of the ions in the surface regions during the optimisation are listed in **Table 5.4**. One of the two lowest energy terminations, termination A, contains 0.5 ML of 3-coordinated Fe_B ions with $c(2\times4)$ symmetry, occupying hexagonal close packed (*hcp*) hollow positions in the top layer. The next layer has a bulk-like structure consisting of rows of O ions along the $[0\,\bar{1}\,1]$ direction with rhombohedral packing. The percentage relaxation experienced by this surface termination is the largest of this study. During its geometry optimisation, the top Fe_B ions move towards the bulk by 0.59 Å, causing 0.25 ML of the O in the layer underneath to move towards the surface by 0.62 Å. As we can see

in **Table 5.4**, the fourth and fifth atomic layers are also affected by the surface relaxation. Termination B terminates with 0.5 ML of 3-coordinated Fe_B with $p(1\times2)$ symmetry, where these ions occupy hcp hollow sites, followed by a bulk-like structure consisting of rows of Fe_A alternating along the $[0\bar{1}1]$ direction with two rows of O ions with rhombohedral packing. During energy minimization, the top Fe_B and Fe_A ions move towards the bulk by 0.09 Å and 0.31 Å respectively. The mean Fe_A-Fe_B distance in the surface layer of the relaxed structure is 3.55 Å (as opposed to the calculated bulk value of 3.48 Å), which is in excellent agreement with 3.6 ± 0.4 Å, the experimental distance reported between the two features (Fe_A and Fe_B) from an STM image (Lennie *et al.*, 1996).

Table 5.4. Perpendicular movement (Δd_z) of the Fe_3O_4 surface species on the most stable (111) terminations after relaxation. Note that a negative value indicates a movement towards the bulk. Distances are given in Å.

(111) termination A				(111) termination B		
layer	**Species**		**Δd_z**	**layer**	**Species**	**Δd_z**
1st	Fe_B		−0.59	1st	Fe_B	−0.09
2nd	O	0.75 ML	−0.10	2nd	Fe_A	−0.31
		0.25 ML	0.62	3rd	O	−0.03
3rd	Fe_A		0.09	4th	Fe_B	0.06
4th	Fe_B		0.41	5th	O	0.03
5th	Fe_A		−0.21	6th	Fe_A	0.02
6th	O		−0.08	7th	Fe_B	0.03
7th	Fe_B		0.00			
Bulk				Bulk		

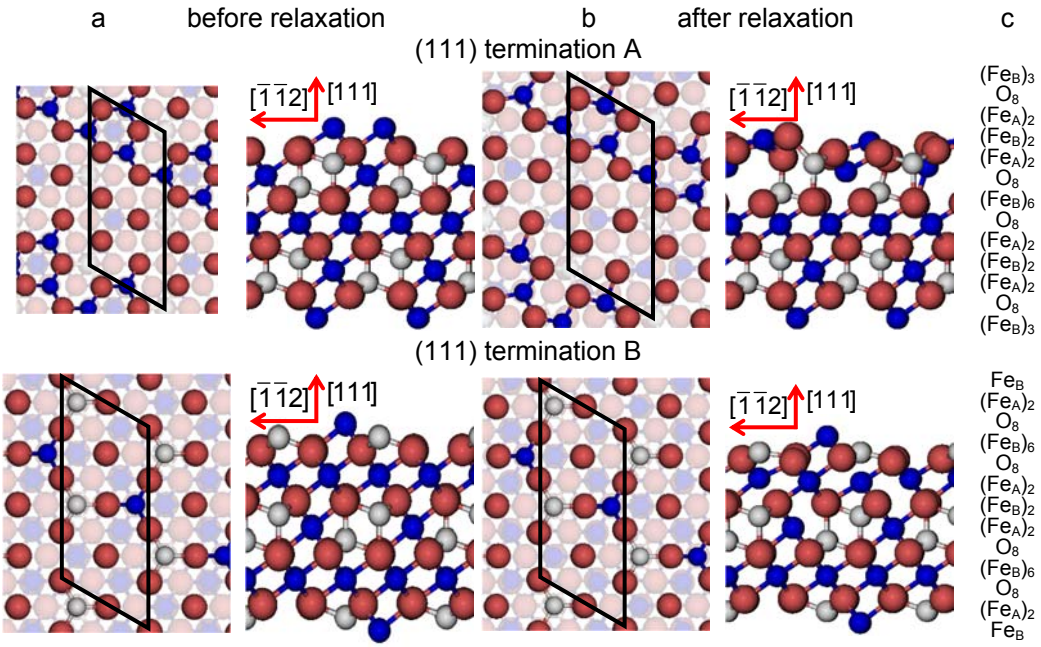

Figure 5.4. Top and side view of the simulation slabs for terminations A and B of Fe_3O_4(111) surface. The surfaces are shown (column a) before, (column b) after relaxation and (column c) their stacking sequence. For the colour code see **Figure 5.1**. Layers with atoms with dangling bonds are highlighted. The crystallographic direction for the top view of (111) surface terminations is $[0\,\bar{1}1]$ for the longest axis towards the top.

5.3.1 Morphology

Since the morphology of Fe_3O_4 crystals has been studied experimentally, we compare our results with those reported for synthetic Fe_3O_4 crystals (Zhao *et al.*, 2008). We have derived a Wulff (1901) crystal morphology of pristine Fe_3O_4 using the lowest surface energies for each Miller index. Its calculated equilibrium morphology is then expressed as a cubic shape with truncated corners, **Figure 5.5 (a)**. As expected, the (001) plane dominates the morphology, followed by the (111) surface truncating the corners of the cube. The (011) surface does not appear in the morphology of Fe_3O_4

due to the mathematical relation between the energy of the surfaces and their position in the crystal (Mellan and Grau-Crespo, 2012). Despite the (011) surface having a surface energy of the same order of magnitude as the others, it is not expressed in the Wulff construction due to competition with the (001) surface. The ratio between their surface energies: $\gamma(011)/\gamma(001) = 1.43 > \sqrt{2}$, see **Figure 5.5 (b)**, and, as shown in **Figure 5.5 (d)**, the (011) surface would only become present in the crystal morphology if $\gamma(011)/\gamma(001) < \sqrt{2}$.

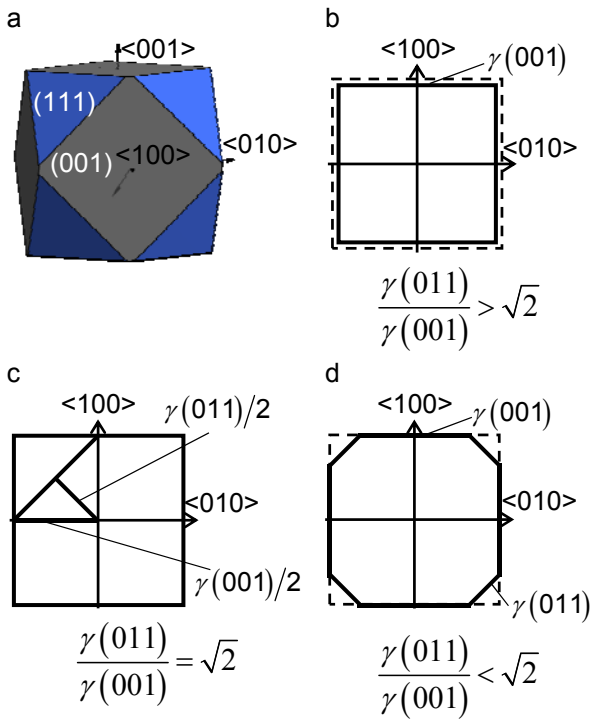

Figure 5.5. (a) Equilibrium morphology for a Fe_3O_4 crystal derived from a Wulff construction. (b) – (d) Schemes of the crystal cross-sectional planes along the <100> and <010> axes for different ratios of stabilities of the lateral surfaces, which illustrate why the (011) surface is absent in the equilibrium morphology.

There are many ways to modify the shape of nanoparticles, such as solvent, media, capping agents, temperature or viscosity, but the Wulff morphology shown in **Figure 5.5 (a)** expresses a particle produced in conditions of perfect thermodynamic equilibrium, vacuum and at 0 K. Nevertheless, our results compare well with the morphologies of crystals synthesised by Zhao *et al.* (2008), who described the formation of Fe_3O_4 under different pH conditions. They increased the OH^- concentration and the resulting crystal shapes changed from cubic (or spherical – depending on other conditions-) at low pH via truncated octahedral to octahedral at high pH values. All their crystals showed mainly the (001) and (111) surfaces but, in some cases, a little (011) surface was expressed due to certain conditions which may modify the surfaces' relative energies. The occasional appearance of the (011) surface is rationalised in terms of kinetically-controlled anisotropic growth of the Fe_3O_4 nanoparticles. Zhao *et al.* (2008) suggested that a high concentration of KOH in the solution can lead to selective adsorption of the hydroxyl anions to certain planes of the crystal, which slows down considerably their growth process. Therefore, the presence of these ions can affect the relative stabilities of the different crystal surfaces. The inversion of the nature of the inequality $\gamma(011)/\gamma(001) > \sqrt{2}$, which already lies close to $\sqrt{2}$, will cause the (011) plane to show up in the morphology.

5.3.2 Scanning tunnelling microscopy images simulation

From the optimised structures of the planes and terminations that are expressed in the morphology, *i.e.* termination A of (001) and terminations A and B of (111) surfaces, we have derived the topographical STM images. These images provide information

about the spatial distribution of the valence band states in the vicinity of the Fermi energy (E_F). The above is particularly useful for systems where atoms (in our case O atoms) can be added or removed from many different positions on the surface. Modelled STM images may help to clarify experimental ones by direct comparison, for instance to identify between the two possible terminations of (111) surface, whose surface energies are very close, and also to validate the most stable termination of the (001) surface. The model also avoids any external perturbations, like the electric field of an STM experimental tip, which can influence the position of atomic species adsorbed on a surface (Irrera *et al.*, 2013).

The STM images in **Figure 5.6** are calculated on pristine Fe_3O_4(001) and (111) surfaces. **Figure 5.6 (a)** shows the STM image of the Fe_3O_4(001) surface, termination A, acquired at a distance (d) of 1.90 Å to the tip and at a density (ρ) of 0.0059 $e \cdot Å^{-3}$. This image resolves the protruding 2-coordinted Fe_A as the brightest spots with $\left(\sqrt{2} \times \sqrt{2}\right) R45°$ symmetry. The O ions from the layer below are also clearly well-defined circles forming rows along the [110] direction and with cubic packing. The STM image of termination A of the (001) surface does not show the atomic positions of the Fe_B placed in the same layer as the O ions due to their low partial charges at this bias. We observed the reproduction of the Fe_A ions in the same symmetry in the STM image obtained from annealed Fe_3O_4 at 623 K (Parkinson *et al.*, 2011).

The STM image of the Fe_3O_4(111) surface termination A is shown in **Figure 5.6 (b)** acquired at a density of 0.0055 $e \cdot Å^{-3}$ and a distance of 1.50 Å to the tip**.** The image resolves the protruding Fe_B as the brightest spots along rows in the $[1\bar{1}0]$ direction

and as dots in between these rows. The undulation of the rows is due to the 0.25 ML of O atoms in the 2nd layer that have moved towards the surface after minimization. From the modelled STM, we can even observe the rhombohedral packing of the sub-layer O ions.

The last STM image in **Figure 5.6 (c)** corresponds to termination B of the $Fe_3O_4(111)$ surface obtained with a density of 0.0276 $e \cdot Å^{-3}$ and the tip at 0.70 Å from the highest atom. The image acquired resolves the protruding Fe_B as the brightest spots in the STM image with a $p(1\times 2)$ symmetry and the Fe_A ions from the layer below which are always bonded to three O atoms immediately underneath. This atomic arrangement forms a pattern of incomplete hexagons (with Fe atom vacancies in one vertex of the imaginary hexagon) which can be seen as a thermally equilibrated structure with vacancies evenly distributed. Details of the layers further below are also visible in our STM image. Experimental studies of the $Fe_3O_4(111)$ surface (Lennie *et al.*, 1996) have shown that among the two different terminations considered there, the one with 0.50 ML of Fe atoms is more stable than the one with 0.75 ML of Fe atoms and 0.25 ML of O atoms, agreeing well with our model of termination B of the (111) surface, whose simulated STM is shown in **Figure 5.6 (c)**. The calculated vertical distance between the Fe_A in the vertex of the hexagon and the O ion in its centre is 0.50 Å, which also agrees well with the value reported experimentally, 0.5 Å (Lennie *et al.*, 1996). This experimental termination shows regions with full hexagons and others with incomplete hexagons (due to Fe vacancies). This atomic rearrangement may be a consequence of the high temperatures to which the surface was exposed.

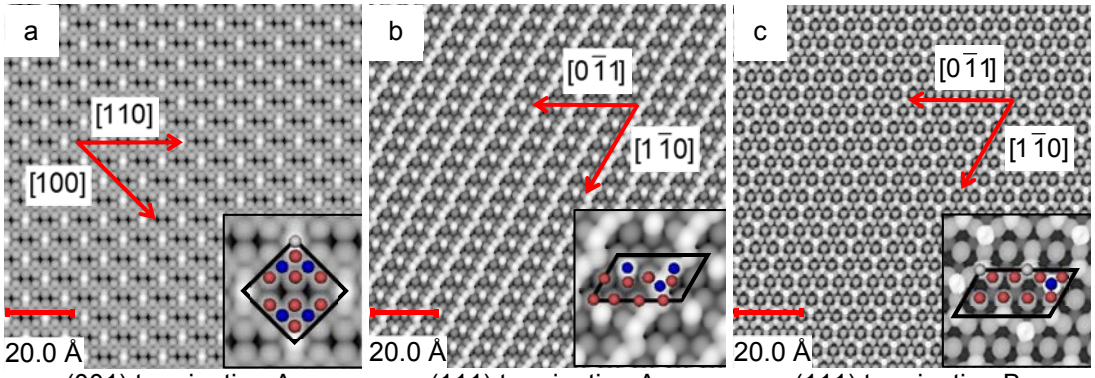

(001) termination A ρ= 0.0059 $e \cdot Å^{-3}$, d = 1.90 Å

(111) termination A ρ= 0.0055 $e \cdot Å^{-3}$, d = 1.50 Å

(111) termination B ρ= 0.0276 $e \cdot Å^{-3}$, d = 0.70 Å

Figure 5.6. Simulated STM images of (a) termination A of (001), (b) termination A of (111) and (c) termination B of (111) surfaces obtained using a bias of −2.5 eV. Density (ρ) and tip distance (d) are also indicated. Insets show enlargements of the STM images. In the inset, Fe_A ions are in grey, Fe_B ions are in blue and O ions are in red.

5.4 Redox behaviour

We have studied the redox properties of the most stable terminations, A and B, of the Fe_3O_4(001) and (111) surfaces, respectively, by comparing the surface free energies corresponding to different O to Fe ratios at the surface. We maintained the number of Fe atoms in the slab as in the stoichiometric surface, but we modified the number of O atoms in the top layer by Γ (given by equation (5.5)), as we were interested in studying the effect of different temperature and oxygen pressure on the stoichiometric non-dipolar surfaces. Because of the size of our supercells, and assuming that O atoms occupy bulk-like positions around the surface Fe atoms, 17 values of Γ are possible if we constrain the calculations to a maximum of one ML of adatoms or vacancies. However, due to the complexity of the (001) and (111) surfaces and in order to reduce

the number of Γ to small values that reflect realistic μ_O, we have used only five values of Γ: Γ = 0 is the stoichiometric surface, Γ = +1, +2 are the partially oxidized surfaces, and Γ = −1, −2 are the partially reduced surfaces. We have represented all of them schematically in **Figures 5.7** and **5.8**.

5.4.1 Reduction of the (001) surface

We discuss the first reduction process Γ = −1 by removing one O atom at the top surface of the slab, which leads to a 0.125 ML of O vacancies, with a vacancy formation energy (E_{vac}) calculated as

$$E_{vac} = \frac{E_{O_2}}{2} + E_{slab,r}^{\Gamma=i-1} - E_{slab,r}^{\Gamma=i} \quad (5.7)$$

where *i* takes values 0 and −1 in the first and second reduction respectively. At the surface there are three different types of O depending on the distance to the protruding 2-coordinated Fe_A ion, see **Figure 5.7**. Thus, the energy required to remove the first O from the surface is 2.60 eV for the atom furthest removed from this Fe_A (see **Figure 5.7** for Γ = −1) and 3.28 eV for the one at intermediate distance. The vacancy created at the third type of O position has an even bigger energy and is therefore very unlikely. The comparison of these energies with the vacancy formation energy in the Fe_3O_4 bulk (2.12 eV), suggests that under thermodynamic equilibrium any surface vacancies will migrate towards the bulk, a phenomenon that has also been observed to occur in another transition metal oxide VO_2 (Mellan and Grau-Crespo, 2012). The tendency of the vacancy to migrate towards the bulk might seem contradictory with the fact that surface oxygen has a lower coordination number than bulk oxygen. However, this can

be rationalized in terms of the oxygen vacancy-containing bulk material undergoing a different degree of relaxation than the oxygen vacancy in the surface slab, thereby driving the creation of the oxygen vacancy in the bulk.

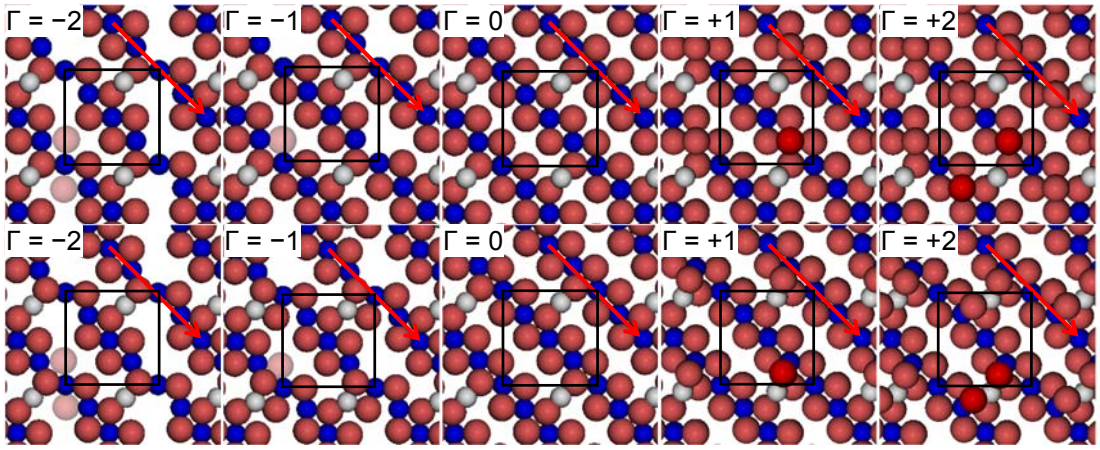

Figure 5.7. Top view of the schematic representation of the Fe_3O_4(001) surface before (top panels) and after relaxation (bottom panels) with different Γ. Stoichiometric (Γ = 0); partially reduced (Γ = −1, −2) and partially oxidized (Γ = +1, +2). Fe_A ions are in grey, Fe_B ions are in blue and O ions are in red, removed O ions are in pale red and added O atoms are in dark red. Only the closest defects are highlighted indicating their relative position, while all of them are shown. The arrows indicate the [110] direction. Black lines indicate the surface unit cell.

We proceed with the second reduction of Fe_3O_4(001) leading to Γ = −2. We removed an O located in the pristine row along the [110] direction, see **Figure 5.7** for Γ = −2, which is at intermediate distance to Fe_A. This second vacancy is 3.23 eV less favourable than the previous state but it is just more likely than removing a more distant O ion from the row where the vacancy is now being created, 3.31 eV. This indicates that although the first vacancy is created preferentially in a position far away

from the 2-coordinated Fe_A, the second reduction might lead to a vacancy in the following O row at an intermediate distance from Fe_A. As the energies to create the second vacancy in the two positions already described are within the DFT error, it might also be possible to find vacancies in the O positions further away from the row where the vacancy is now being created.

We have characterised the $\Gamma = -1$ surface by means of a Bader analysis and compared the atomic charges with those on the pristine surface. The positive charge of the protruding Fe_A ion was increased by a negligible amount ($< 0.05\ e^-$), where this small variation can be accounted for by the defect that was created at the farthest O location. The surface Fe_B ions, however, are reduced, especially the ones closest to the vacancy with a variation in charge of $0.25 - 0.37\ e^-$. This can be interpreted in terms of the number of O ions directly coordinated to the Fe_B ions, see **Figure 5.7** for $\Gamma = -1$, where just over 80 % of the electron density is transferred to the Fe_B ions after removing the O atoms.

5.4.2 Reduction of the (111) surface

We have also explored different positions for the creation of the O ($\Gamma = -1$) vacancies in the Fe_3O_4(111) surface to find the lowest-energy configuration for this particular surface. We found that the process is thermodynamically even more unfavourable than on the (001) surface by 0.24 eV. The most likely vacancy is created in the centre of an incomplete Fe-hexagon, see **Figure 5.8** for $\Gamma = -1$. To remove an O atom coordinated to the 3-coordinated Fe_A (opposite to the missing Fe in the incomplete hexagon)

requires an energy of 3.56 eV. As in the (001) surface, any vacancy created in the (111) surface will be thermodynamically prone to migrate towards the bulk.

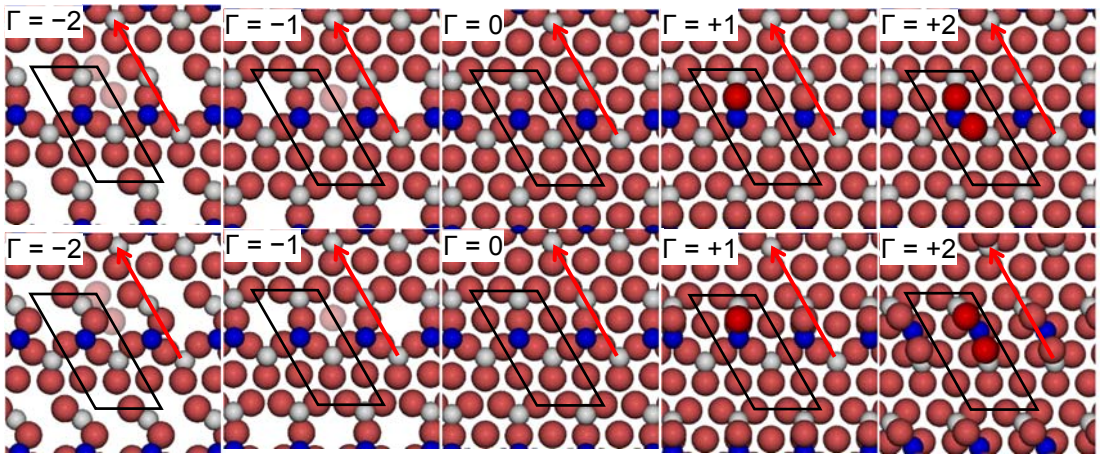

Figure 5.8. Top view of the schematic representation of the Fe_3O_4(111) surface before (top panels) and after relaxation (bottom panels) with different Γ. Stoichiometric (Γ = 0); partially reduced (Γ = −1, −2) and partially oxidized (Γ = +1, +2). Fe_A ions are in grey, Fe_B ions are in blue and O ions are in red, removed O ions are in pale red and added O atoms are in dark red. Only the closest defects are highlighted indicating their relative position, while all of them are shown. The arrows indicate the $[0\,\bar{1}\,1]$ direction. Black lines indicate the surface unit cell.

Creating a second vacancy among the atoms coordinated to the 3-coordinated Fe_A, **Figure 5.8** for Γ = −2 costs 3.45 eV, which is less costly by 0.19 eV than removing the left O within the hexagon. These energies provide information about the consecutive reduction mechanism, where the first O vacancy is created in the centre of the incomplete Fe-hexagons and the next in one of the atom positions coordinated to the 3-coordinated Fe_A.

The Bader analysis indicates that upon vacancy formation on the Γ = −1 surface, charge transfer on the Fe_A is negligible and the protruding 3-coordinated Fe_B is only slightly reduced. However, the Fe_B ions whose charge is affected more are those in the 4th atomic layer (see **Figure 5.4**) below the removed O atom to which they were previously directly coordinated. Altogether, the charge on those three Fe_B is reduced by ~0.89 e^-, *i.e.* they have accepted 78.5 % of the electron density previously held by the removed O.

5.4.3 Oxidation of the (001) surface

Another process we have studied is the surface oxidation by adsorption of one O atom leading to 0.125 ML of adatoms (Γ = +1). This process involves an adsorption energy per adatom derived from the equation,

$$E_{ads} = E_{slab}^{\Gamma=j+1} - E_{slab}^{\Gamma=j} - \frac{E[O_2]}{2} \quad (5.8)$$

(where j takes values 0 and +1 in the first and second oxidation respectively). For j = 0, E_{ads} is calculated at −1.87 eV. We considered that the O adatom is located similarly to the bulk structure, interacting simultaneously with the protruding 2-coordinated Fe_A and one of the 5-coordinated surface Fe_B, see **Figure 5.7** for Γ = +1. Other configurations, like the one with the O adatom interacting only atop the protruding 2-coordinated Fe_A, release less energy per adatom, −1.14 eV. The bond distance between the added O atoms and the Fe ions (1.87 Å for Fe_A and 1.83 Å for Fe_B) is shorter than the first neighbour distance to both types of Fe in the bulk (1.89 Å for Fe_A and 2.05 Å for Fe_B) (Roldan *et al.*, 2013), as is expected due to contraction of the top atomic

surface layers after relaxation. The strongly exothermic adsorption suggests a favourable oxidation process, but as it is affected by μ_O, its evaluation requires a complete analysis of the gas partial pressure in equilibrium with the surface.

Adding a second O atom ($\Gamma = +2$) is also an exothermic process, releasing 0.96 eV per adatom. The second O atom preferentially coordinates the protruding Fe_A and a 5-coordinated Fe_B, forming another O bridging structure colinear with the $[\bar{1}10]$ direction, **Figure 5.7** for $\Gamma = +2$. As for $\Gamma = +1$, the top atomic contraction leads to short Fe−O distances, 1.85 Å. Another conformation for the second O adsorption is coordinating equivalent atoms but forming a V-shaped structure, leading to a weaker adsorption (E_{ads}= −0.80 eV).

At this point, it is worth mentioning that although we started from the ideal terminations similar to the bulk when we added the first and second oxygen atom, this did not prevent them to relax to a different position. In fact, we can see in **Figure 5.7** for $\Gamma = +1$ (and +2), that after surface relaxation, the added oxygen has moved from its bulk site to another position, closer to the protruding Fe_A. This finding agrees with the work of Reuter and Scheffler (2001), who found for RuO_2(110) that terminations at positions different from the bulk can be important in non-stoichiometric compositions.

The Bader analysis on the density of the ($\Gamma = +1$) oxidised (001) surface shows the oxidation of the top layer Fe_B by 0.60 e^- while the protruding 2-coordinated Fe_A ion only donates 0.04 e^- to the newly added O atom. Hence, the O adatom gains 1.00 e^-

mainly from the surface metals whereas the charge of the surface anions (all of them more negative than the adatom) change by about 0.02 e^-.

5.4.4 Oxidation of the (111) surface

On the (111) surface, the adsorption of one O atom ($\Gamma = +1$) led to the formation of a bridging structure between the protruding Fe_B and one of the three closest 3-coordinated Fe_A (see **Figure 5.8** for $\Gamma = +1$) releasing 3.00 eV. A less stable configuration is the one where the O-adatom is sitting atop the protruding Fe_B providing an E_{ads} of −2.04 eV.

The addition of a second O-adatom coordinating the protruding Fe_B and one of the other two closest unoccupied 3-coordinated Fe_A releases 2.30 eV; see the schematic representation in **Figure 5.8** for $\Gamma = +2$. During the optimisation, this second oxygen pushes the protruding 3-coordinated Fe_B out of its equilibrium position in the stoichiometric surface, thereby forming a Fe_A-O-Fe_B-O-Fe_A row of atoms along the $[0\,\bar{1}\,1]$ direction. The equilibrium bond lengths, Fe_A-O and Fe_B-O are 1.86 Å and 1.80 Å respectively, which compares well with values reported before (between 1.80 – 1.85 Å) for the Fe-O distance at the Fe_3O_4(111) surface (Martin *et al.*, 2009). In the next most favourable conformation the second O is located atop one surface O coordinating only the Fe_A, but this process is endothermic by 0.43 eV. The calculations thus show that both the first and second adsorbed O preferentially coordinate the protruding 3-coordinated Fe_B and two of its Fe_A neighbours with a resulting bridging structure in the $[0\,\bar{1}\,1]$ direction.

Unlike the (001) surface, where the added oxygen atoms moved during the energy minimization, in the (111) we observed instead that the protruding Fe_B ion moved from its bulk position after the addition of two defects ($\Gamma = +2$), see **Figure 5.8**. This validates in our methodology the possibility of exploring non-bulk-like relaxed positions for any atom in the surface of our slab, as long as all non-equivalent bulk-like positions for the defects are carefully investigated.

The Bader analysis indicates that in the preferred structure for $\Gamma = +1$, the adatom gains 1.04 e^-, where the charge of the other surface O atoms decreased as little as in the (001) surface. Amongst the two Fe ions coordinated to the added O atom, Fe_B increases its charge by 0.08 e^-, but Fe_A by 0.39 e^-. The charge on other surface Fe_A and Fe_B ions upon addition of the O atom changed by an average of 0.03 e^- and −0.01 e^- respectively.

5.5 Temperature and pressure effects

In this section, we discuss the thermodynamics of the redox processes at the (001) and (111) surfaces as a function of temperature and O_2 partial pressure in the gas phase. We express these macroscopic parameters by μ_O.

In **Figure 5.9 (a)**, we have plotted μ_O in terms of temperature and the log p, along abscissas for easy comparison with the plots in **Figures 5.9 (b)** and **(c)**. All the information used for the construction of **Figure 5.9 (a)** comes from experiment (Chase, 1998) and is independent from the calculations (see Computational Methods section

on Chapter 5). Variations in T and p are necessary to modify the value of μ_O as required and to reflect different reducing or oxidising conditions. For example, the oxygen chemical potential is −0.3 eV (which is a typical oxidising value) at ambient conditions, *i.e.* at the intercept of T = 298.15 K and p = 0.21 bar, while more reducing conditions (lower values of μ_O) can be achieved by increasing T while keeping the pressure constant (*i.e.* horizontal solid line in **Figure 5.9 (a)**).

The area between the two vertical dashed lines (μ_O from −3.13 to −2.44 eV) in **Figure 5.9** corresponds to the conditions where the Fe_3O_4 bulk material is thermodynamically stable with respect to both FeO and Fe_2O_3 bulk. We have derived these conditions (μ_O) from the experimental formation enthalpy of the three oxides (Haynes, 2012) and their increasing oxidation from FeO to Fe_2O_3, see equation (5.9). Under normal conditions, Fe_2O_3 is the thermodynamically stable bulk phase, while the synthesis of Fe_3O_4 requires high temperatures or a low pressure of O_2 (which ultimately can lead to FeO).

$$\begin{aligned} 3\ FeO + \frac{1}{2}\ O_2 &\rightleftharpoons Fe_3O_4 \\ 2\ Fe_3O_4 + \frac{1}{2}\ O_2 &\rightleftharpoons 3\ Fe_2O_3 \end{aligned} \qquad (5.9)$$

Figures 5.9 (b) and **(c)** show the variation of the surface free energies ($\Delta\sigma$) of each surface composition versus μ_O. Note that we have only used the most stable configuration for Γ = –2, –1, 0, +1, +2. Further degrees of reduction/oxidation ($\Gamma = \pm 3$) could also be investigated but instead of exploring many different positions where to remove or add the O atoms, we have linearly fitted the intercept of the linear

regressions in **Figure 5.9** as a function of Γ for inferring the intercepts of further oxidation/reduction of these surfaces. We have limited this treatment to three defects, as a higher number can lead to the formation of molecular oxygen in the case of oxidation or a new oxide phase in the case of reduction.

At μ_O = −0.3 eV (ambient conditions), the (Γ = +3) oxidation of the Fe_3O_4(001) surface will take place, see **Figure 5.9 (b)**. For the conditions where bulk Fe_3O_4 is the most stable oxide, the (Γ = +3) oxidized (001) remains the most stable surface up to μ_O = −1.25 eV, from where the surface experiences a progressive reduction. In the early stages of this reduction, the unit cell loses two O atoms and remains so until μ_O = −1.85 eV. Beyond that chemical potential and until μ_O = −2.60 eV, which is just beyond the conditions in which the phase transition from Fe_2O_3 to Fe_3O_4 takes place, the most stable surface is the stoichiometric one. At lower values of μ_O = −3.00 eV (but still within the conditions in which Fe_3O_4 is the most stable phase), the (Γ = −3) reduced surface is the favoured system, until reaching the conditions where the reduced bulk phase of FeO is the most stable oxide. A recent publication by Nie *et al.* (2013) reports that the Fe_3O_4(001) surface is oxidised under exposure to 4×10^{-9} bar of oxygen at 923 K. They used low-energy electron microscopy (LEEM) and Raman spectroscopy to prove that Fe_3O_4 grows at the expenses of Fe ions migrating from the bulk towards the surface. The Fe ion vacancies in the bulk, in turn, transform it into α-Fe_2O_3 (hematite), which is the equilibrium iron oxide phase at the temperature and pressure of the experiment. Our results hence agree well with these experimental

findings, although they are close to the limit in which the stoichiometric surface is the most stable one. The experimental conditions described above correspond to μ_O = −1.75 eV according to equation (5.6), a value at which the Fe_3O_4(001) surface is prone to suffer oxidation (see **Figure 5.9 (b)**), by adding one O atom per surface unit cell around the protruding Fe_A. Our results, however, agree partially with those reported in a DFT study by Pentcheva *et al.* (2005) as those authors found that the modified non-stoichiometric polar bulk-like Fe_3O_4(001) surface (Fe_B-O layer) is the most stable under any chemical potential. However, the surface proposed by Pentcheva *et al.* (2005) is a generic oxidised (001) surface, created from a bulk-like termination, whereas our surface is gradually oxidised or reduced. However, regardless of terminations and reconstructions, we also predict our non-dipolar surface to be (Γ = +3 and +1) oxidized up to μ_O = −1.85 eV, but from this value of chemical potential onwards, our results predict a gradual reduction, which no longer agrees with the work by Pentcheva *et al.* (2005) as they predict the same oxidized surface for any value of μ_O.

The redox behaviour of the Fe_3O_4(111) surface is shown in **Figure 5.9 (c)**. It indicates that the redox properties of the (111) surface are similar to the (001) surface, although the oxidized character extends to lower chemical potentials. The surface tends to be (Γ = +3) oxidised under the condition where Fe_2O_3 is the most stable phase and up to μ_O = −2.45 eV, which is within the region where Fe_3O_4 is the thermodynamically most stable iron oxide. From here, the surface loses two O atoms for a very short range of chemical potential, until μ_O = −2.95 eV, from where the surface loses a further two

more O atoms, becoming now reduced up to $\mu_O = -3.25$ eV. From this final value of the chemical potential, the surface becomes reduced ($\Gamma = -3$). In a previous DFT + *U* study, Kiejna *et al.* (2012) studied the redox properties of the $Fe_3O_4(111)$ surface. They only studied the non-stoichiometric dipolar bulk-like terminations and found that the Fe_{A1} surface, which corresponds with a generic oxidized one, is the most stable one up to $\mu_O = -2.6$ eV, from which point their surfaces started to reduce gradually. Although we cannot make a direct comparison of our results due to the different terminations considered in both works, owing to our gradual redox processes, our results show the same trend.

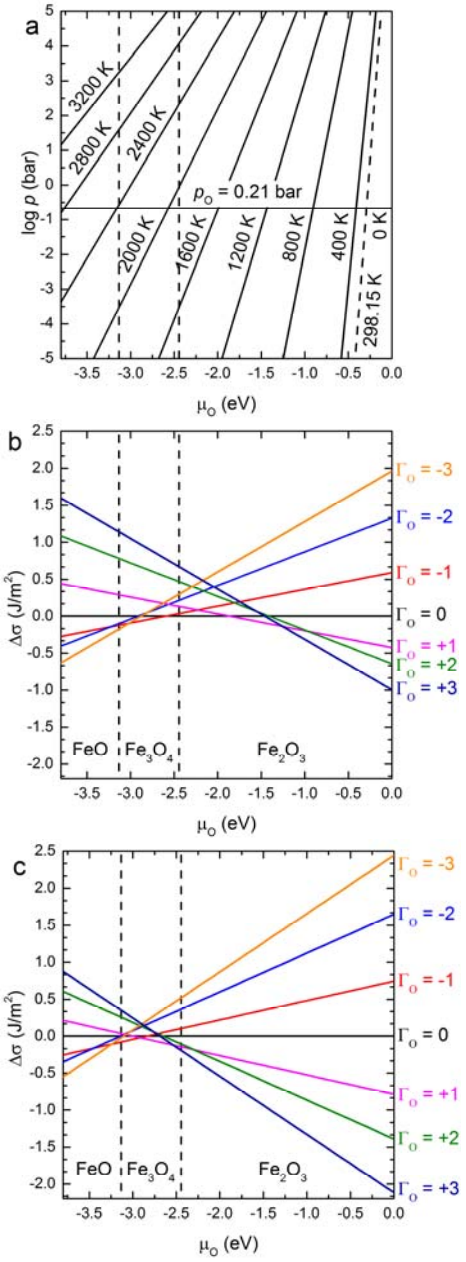

Figure 5.9. (a) μ_O in the gas phase as a function of the temperature and the logarithm of the oxygen partial pressure and relative surface free energies (Δσ) for the Fe_3O_4 (b) (001) and (c) (111) surfaces as a function of the oxygen chemical potential (μ_O). The areas corresponding to μ_O smaller than −3.13 eV, bigger than −2.44 eV and between these two values represent the approximate conditions under which bulk FeO, Fe_2O_3 and Fe_3O_4 respectively are the stable oxides.

Comparing both ($\Gamma = +3$) oxidised surfaces, the (111) is lower in energy than the (001) for the whole μ_O scale considered. Therefore the (111) surface will remain oxidised even at μ_O where Fe_3O_4(001) is not. We suggest then, from **Figure 5.9**, that under the conditions in which the bulk Fe_3O_4 is the most stable oxide, the phase transformation of the reduction of Fe_3O_4 towards FeO will start from the (001) surface. On the other hand, Fe_3O_4 oxidation to Fe_2O_3 would take place initially on the (111).

5.4 Chapter conclusions

In this chapter, we have modelled three different surface orientations of Fe_3O_4 crystals by using DFT methods within the GGA + *U* approximation. We have investigated the stabilities of their multiple (reconstructed) non-dipolar stoichiometric surface terminations and studied the redox properties of the most prominent surfaces. We have modified the redox conditions by creating O vacancies or adding O atoms to the most stable non-dipolar stoichiometric surface termination, under a wide range of chemical potentials, including ambient conditions and those conditions where bulk Fe_3O_4 is the thermodynamically most stable oxide. In the initial stages of oxidation, the excess O atoms form bridging structures with the Fe ions at the surface, and in particular the Fe ions protruding from the surface. We found that some oxidised (non-stoichiometric) structures relaxed in such a way that it broke the bulk-like termination.

We conclude that the Fe-terminated (001) and (111) planes are the most stable Fe_3O_4 surfaces, in agreement with previous experiments as shown by STM images. The

equilibrium morphology of Fe_3O_4 was found to be cubic with truncated corners, which means that (001) and (111) are the main surfaces exposed in the crystals. Although both (001) and (111) surfaces will be oxidized under ambient conditions, both surfaces suffer a gradual reduction, that starts at lower chemical potentials for the (001) surface including the stoichiometric plane.

The reduction of the (001) and (111) surfaces is thermodynamically favourable at the low end of the μ_O values in the region where Fe_3O_4 is the most stable oxide. We found that, in both cases, the O vacancies are likely to migrate towards the bulk, thereby changing the phase structure.

6

Early oxidation stages of greigite Fe_3S_4(001) surface by water

6.1 Introduction

The extremely acidic sulfur-rich wastewaters are a current worldwide problem. The thereafter called acid mine drainage (AMD) or acid rock drainage (ARD) is associated with natural weathering of rock formations (Joeckel *et al.*, 2005) and, in particular, aggravated by existing and historic human activities such as the mining industry (Banks *et al.*, 1997; Bowen *et al.*, 1998; Younger, 2002). Once the mining or processing operations expose the metal sulfide compounds, in particular pyrite FeS_2, to weathering elements (Johnson, 2003) such as O_2 and H_2O as well as certain microorganisms (Fowler *et al.*, 2001, 1999; Schippers and Sand, 1999), the minerals steadily oxidize. This results in reduction of the water pH (Hammarstrom *et al.*, 2003) and potentially high concentrations of toxic metallic and metalloid elements in these solutions (Matlock *et al.*, 2002), depending on the initial composition of the exposed minerals.

The chemical reactions leading to the oxidation and dissolution of metal sulfides have been studied and several types of mechanisms were suggested, depending on the minerals and the oxidizing agent present. In the polysulfide mechanism, characteristic of acid-soluble sulfides, *e.g.* sphalerite (ZnS), protons attack the mineral and produce H_2S. Sulfur-oxidizing bacteria further oxidizes the H_2S to SO_4^{2-} and regenerates the protons (Schippers and Sand, 1999). In the thiosulfate mechanism, characteristic of non-acid-soluble sulfides, *e.g.* pyrite (FeS_2) (Vaughan and Craig, 1978), initially aqueous iron(III) ions attack the metal sulfide mineral generating protons, thiosulfate ($S_2O_3^{2-}$) and iron(II). Secondly, this iron(II) is re-oxidized by iron-oxidizing bacteria, while following several steps, $S_2O_3^{2-}$ decomposes into elemental sulfur and SO_4^{2-} ions (Fowler *et al.*, 2001, 1999; Schippers and Sand, 1999).

Iron sulfides are the most predominant sulfides found in anoxic marine sediments (Morse *et al.*, 1987) and therefore one of the main sources of AMD (Akcil and Koldas, 2006; Johnson and Hallberg, 2005; Johnson, 2003). Although FeS_2 is a stable mineral in these environments (Berner, 1984, 1970; Morse *et al.*, 1987), important research have been devoted to study its oxidation (Chandra and Gerson, 2010; Fowler *et al.*, 2001, 1999; Gartman and Luther, 2014; Lowson, 1982; McKibben and Barnes, 1986; Moses *et al.*, 1987; Rimstidt and Vaughan, 2003; Williamson and Rimstidt, 1994) overlooking other iron sulfide minerals. Among them, greigite (Fe_3S_4) is an intermediate in the formation of FeS_2 (Benning *et al.*, 2000; Dekkers and Schoonen, 1996; Hunger and Benning, 2007; Lennie *et al.*, 1997; Wilkin and Barnes, 1996), which has a long environmental persistence (Stolz *et al.*, 1986) and can also be found

in aquatic environments (Frank *et al.*, 2007; Jelinowska *et al.*, 1998, 1995; Roberts and Turner, 1993; Skinner *et al.*, 1964; Snowball, 1991), soils (Fassbinder *et al.*, 1990; Fassbinder and Stanjek, 1994) as well as in magnetotactic bacteria (Mann *et al.*, 1990) and gastropods (Goffredi *et al.*, 2004).

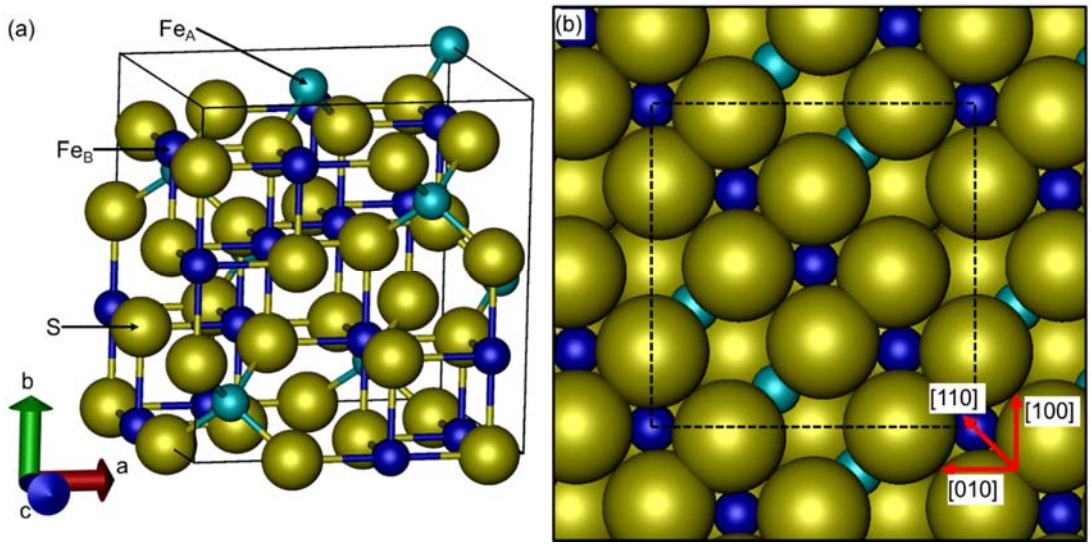

Figure 6.1. (a) Ball-and-stick model of the unit cell of Fe_3S_4 showing the cubic spinel crystal structure and (b) top view of the space-filling model of its (001) surface.

Taking into account the structural differences between FeS_2 and Fe_3S_4 and the decisive role of the persulfide group in dictating the mechanism of the oxidation reactions on metal sulfides (Schippers and Sand, 1999), we have used density functional theory (DFT) calculations to investigate the early oxidation processes of Fe_3S_4 *via* a polysulfide mechanism, in order to explain this mineral's lability on a disturbed aqueous medium. We propose three mechanisms to account for the replacement of one S by one O atom on the top layer of the Fe_3S_4(001) surface, which appears to be the most prominent one (Roldan and de Leeuw, 2015). In any of these pathways, H_2O

may oxidize the (001) surface with the resulting production of molecular H_2S. We have also applied thermodynamic arguments to examine the pH conditions or H_2S concentration, in aqueous solution, and temperatures at which these species are in equilibrium with the stoichiometric and oxidized Fe_3S_4(001) surface, which is relevant to the geochemical formation of AMD.

6.2 Computational methods

We have performed spin-polarized calculations with the Vienna *Ab-initio* Simulation Package (VASP) (Kresse and Furthmüller, 1996a, 1996b; Kresse and Hafner, 1994, 1993). All simulations were carried out within the periodic plane-wave DFT framework. The projector augmented wave (PAW) method was used to describe the electron-ion interaction (Blöchl, 1994; Kresse and Joubert, 1999). The frozen core of the Fe, S and O elements was defined up to and including the 3*p*, 2*p* and 1*s* electrons respectively. At the level of the generalized gradient approximation (GGA), the exchange-correlation in the form of Perdew-Wang 91 (PW91) (Perdew *et al.*, 1993, 1992) functional was used together with the spin interpolation of Vosko *et al.* (1980) The long-range dispersion interactions were added *via* the D2 semiempirical method of Grimme (2006), using the global scaling factor parameter optimized for the Perdew-Burke-Ernzerhof (PBE) (Perdew *et al.*, 1997, 1996a) functional, $s_6 = 0.75$, which has shown to be successful in the modelling of a number of iron minerals (Dzade *et al.*, 2013; Haider *et al.*, 2014; Irrera *et al.*, 2013). Brillouin zone integrations were performed using a Monkhorst-Pack grid (Monkhorst and Pack, 1976) of 4×4×1 *Γ*-

centred *k*-points. In order to increase the integration efficiency in the reciprocal space, the partial occupancies for all calculations were determined using the tetrahedron method with Blöchl corrections (Blöchl *et al.*, 1994). Kohn-Sham (KS) states were expanded in a plane-wave basis set with the kinetic energy's cut-off fixed at 600 eV. The DFT + *U* (Anisimov *et al.*, 1992) version of Dudarev *et al.* (1998) was used for the description of the localized and strongly correlated *d* Fe electrons. Based on previous works, we have chosen a U_{eff} of 1.0 eV (Devey *et al.*, 2009; Haider *et al.*, 2012; Roldan and de Leeuw, 2015; Roldan *et al.*, 2013). Electronic density optimization was stopped when the total energy difference between two consecutive self-consistent loop steps was below 10^{-5} eV. Atomic positions were relaxed to their ground state using the conjugates-gradient method and were considered converged when the Hellmann-Feynman forces on all atoms were smaller than 0.02 eV·Å^{-1}. The dimer method was used to search the transitions states (TS) (Henkelman and Jónsson, 1999; Heyden *et al.*, 2005), which were characterised by frequency calculations to confirm the existence of only one normal mode associated with an imaginary frequency corresponding to the reaction coordinate. Higher cut-off values and *k*-point grids as well as a lower self-consistent energy threshold were tested to ensure energies were converged within 1 meV per atom.

Greigite has a spinel crystal structure characterized by the space group $Fd\bar{3}m$ (Skinner *et al.*, 1964). The face-centred cubic unit cell is composed by 32 sulfur anions, which are nearly regularly close packed along the [111] direction. This S arrangement generates 8 tetrahedral (A) and 16 octahedral (B) holes per unit cell occupied by Fe cations, giving a total of eight formula units (f.u.), see **Figure 6.1 (a)**. Fe_3S_4 is a 2−3

type spinel, which is a classification based on the cation valency, that indicates the existence of one Fe^{2+} and two Fe^{3+} cations per formula unit. This spinel has an *inverse* cation distribution $Fe_A^{3+}\left[Fe^{2+}Fe^{3+}\right]_B S_4$, where half of the Fe^{3+} cations are filling the A positions and all the Fe^{2+} together with the rest of the Fe^{3+} ions are occupying the B holes (Chang *et al.*, 2009; Dekkers *et al.*, 2000; Surerus *et al.*, 1989; Vaughan and Craig, 1985; Vaughan and Tossell, 1981). Initial magnetic moments of the A and B sublattices were set antiparallely, in line with previous studies (Devey *et al.*, 2009; Roldan *et al.*, 2013).

Surface calculations were carried out using the (001) slab model, see **Figure 6.1 (b)**, defined in a previous study of the catalytic dissociation of H_2O on various Fe_3S_4 surfaces (Roldan and de Leeuw, 2015). The topmost layer of the (001) surface is finished with a bulk-like structure containing single rows in the [110] direction of 5-coordinated Fe_B ions alternating every two single rows of O ions with cubic packing. Beneath this layer, there are 1.5 monolayers (ML) of 4-coordinated Fe_A forming also rows parallel to the S ones. From this layer, 0.5 ML with a $\left(\sqrt{2}\times\sqrt{2}\right)R45°$ symmetry come from above the surface, which moved inward during relaxation. These slabs were composed by 8 formula units of Fe_3S_4 and separated by 12 Å of vacuum in the direction perpendicular to the surface. The bottom 5 atomic layers were kept frozen at their relaxed bulk positions, while the remaining top layers were allowed to relax. This computational setup of the Fe_3S_4 surfaces is equivalent to the one used before for the description of the non-dipolar stoichiometric surfaces of its oxide counterpart Fe_3O_4 (Santos-Carballal *et al.*, 2014), which provided an accurate and realistic means for

calculating the surface properties of this mineral. Convergence of the slab energy within 1 meV was further tested with different slab and vacuum thickness as well as number of relaxed layers. In order to enhance the electronic convergence, dipole corrections perpendicular to the surface were included in our simulations to account for the dipole created due to the chemical species added in the relaxed surface of the slab (Makov and Payne, 1995; Neugebauer and Scheffler, 1992).

A Bader analysis was used to partition the charge density grid into atomic charges (Henkelman *et al.*, 2006; Sanville *et al.*, 2007; Tang *et al.*, 2009). Charge density difference diagrams were constructed by subtracting from the electronic charge density of the total adsorbate-surface system, the sum of the charge densities of the isolated adsorbate and clean surface in the same geometry.

The energy of the system along the profile of the proposed mechanisms was calculated according to the following equation,

$$E_{\text{state}} = E_{\text{system}} - nE_{\text{H}_2\text{O}} - E_{\text{slab}} \tag{6.1}$$

where *n* represents the number of H_2O molecules and E_{system}, $E_{\text{H}_2\text{O}}$ and E_{slab} are the energy of the system, one isolated H_2O molecule in vacuum and the pristine stoichiometric relaxed Fe_3S_4(001) surface slab respectively.

6.3 Fe_3S_4(001) surface oxidation

We considered three main mechanisms for studying the oxidation of the Fe_3S_4(001) surface through the exchange of a S on the top layer by an O atom from the water

releasing one H_2S molecule, as shown in **Figures 6.3 (a)**, **6.5 (a)** and **6.7**. In these schemes, the numbers identify a particular state in the mechanism, E^i_{ads} is the adsorption energy, E^i_{diss} is the dissociation energy of the specie *i*, $E_{\text{A}j}$ is the activation energy of the step *j*, $E^{\text{SH}}_{\text{prot}}$ is the energy required to move one H atom from the H_2O to the SH group and $E^{\text{O}\rightarrow\text{S}}_{\text{exch}}$ is the total energy required to exchange one S atom in the mineral surface by an O atom from the water. In this paper, we do not analyse the dissociative adsorption of one or two H_2O molecules (where only one dissociates) or the OH group as they have already been discussed before (Roldan and de Leeuw, 2015). Therefore, we have chosen the most favourable mode of adsorption of these states as the initial configurations in this work.

6.3.1 Pathway 1

Dissociative adsorption on the (001) surface of one H_2O molecule is thermodynamically more favourable to happen with its O atom coordinating one of the Fe_B ions, at 1.83 Å of distance, see state 2 on **Table 6.1** and **Figure 6.3** (Roldan and de Leeuw, 2015). In the hydroxyl group, the O−H distance is 0.98 Å. Although all Fe_B are equivalent in this surface, the existence of the Fe_A ions and the newly absorbed H_2O molecule generates four non-equivalent types of S ions around the hydroxylated Fe_B ion. The dissociated H, in turn, is more probable to be found attached at 1.36 Å of distance to the S next to the hydroxylated Fe_B. The H atom now bounded to the mineral surface is located between three S atoms, at the tetrahedral cavity of the Fe_A row on the [110] direction. The charge analysis indicates that, after adsorption, there is a charge transfer mainly from the hydroxyl O and the protonated S to their

respective H, which indicates the covalent character interaction between these two pair of atoms. We have quantified the increase of charge of the O and S atoms as 1.0 and 1.1 e^- respectively, while the H atoms reduced their charge by an average of 1.3 e^-. This can be represented graphically in a charge density difference plot, illustrating density changes on the dissociative adsorption of one H_2O molecule, **Figure 6.2**, where we can see that charge is mostly localized on the O−H and S−H bonds. We found that configuration 2 is 0.34 eV above the energy of the pristine Fe_3S_4(001) and one isolated H_2O molecule. We also tested the possibility of the migration of the remaining H atom from the hydroxyl group to the protonated S atom, but several initial configurations led to OH + SH as O is more basic than SH. This agrees with the similar behaviour found for the (001) surface of $FeNi_2S_4$ (Haider *et al.*, 2014), an intermediate spinel between the one under study in this work and Ni_3S_4.

The reaction profile for the exchange of one S by one O atom on the Fe_3S_4(001) surface, according to mechanism 1, is shown in **Figure 6.3**, where only one H_2O molecule per surface unit cell is involved, equivalent to 0.25 ML of coverage. Note that we have defined a full ML as the amount of H_2O required to hydrate the four Fe_B ions per formula unit. The protonated S is the most available one to be exchanged by the OH group. In a concerted step, the SH group migrates to the top of the next Fe_B ion on the surface layer, while the OH group takes its place, increasing its coordination number with three Fe ions. This is an exothermic process with an $E_{\text{exch}}^{\text{O}\rightarrow\text{S}}$ of −0.24 eV and an activation energy (E_{A1}) of 0.80 eV. On the structure after the exchange of SH by OH, shown for the state 4 on **Figure 6.3**, the O atom lays at 0.63 Å below the average

position of the surface layer of S atoms, in part due to its smaller ionic radius with respect to the S ions. At the same state, the H of the hydroxyl is at 0.98 Å of the O atom, see **Table 6.1**, pointing upwards in such a way that it lies on the cavity of the Fe_A row along the [110] direction, at the same level of the top S layer. The S−H and Fe_B−S distances of the SH group are 1.35 and 2.27 Å respectively. The charge analysis shows that after the SH exchange by OH, the hydroxyl group has received 0.26 e^- (where 0.18 e^- were located on the O atom), donated by the H of the SH group (0.18 e^-) and the Fe_B binding it (0.11 e^-). The charge transfers associated with the exchange process explains the availability of a protonated S ion to exchange its place with the more nucleophilic OH group. **Figure 6.2** shows the charge transfer mechanism, at the state 4, with respect to the oxidized surface and the H_2S dissociative adsorption. While the electronic density located on the O−H bond comes primarily from the H, the S atom of the adsorbed SH gave its electrons to form the Fe_B−S bond and reinforce the S−H one, in agreement with the atomic electronegativities.

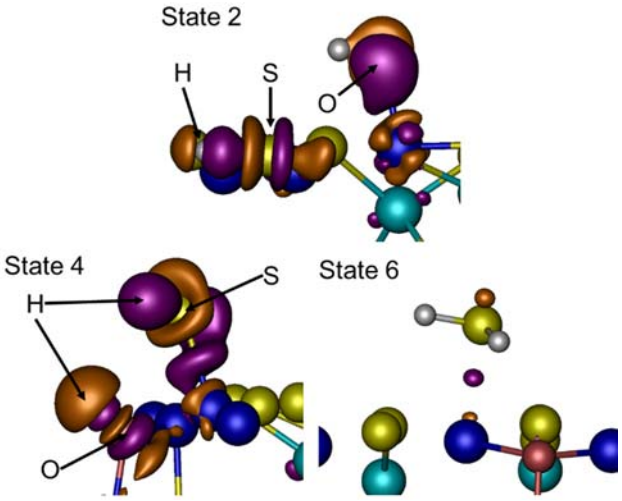

Figure 6.2. Charge density difference plot of the adsorption at different stages along the oxidation of the Fe_3S_4(001) surface following pathway 1. Isosurfaces of the difference density are displayed at a value of ±0.05 e·Å^{-3}, where purple and orange represent gain and lost electron density respectively. Light blue atoms represent Fe_A, dark blue for Fe_B, yellow for S, red for O and white for H.

Table 6.1. Calculated bond distances (Å) and angles (°) at different minima states along the Fe_3S_4(001) surface oxidation following pathway 1.

state	2	4	6
d(O−Fe_{B1})	1.83	--	--
d(S−Fe_{B2})	--	2.27	2.70
d(H_1−O)	0.98	0.98	
d(H_1−S)			1.35
d(H_2−S)	1.36	1.35	1.35
∠H_1−S−H_2	--	--	92.3

The next step in this mechanism is the generation of H_2S following the migration of the hydroxyl H, see state 6 on **Figure 6.3**. In the resulting structure, the O remains

slightly below the top S layer, but moved horizontally by 0.81 Å closer to the Fe_B ion holding the H_2S molecule. The H_2S molecule is adsorbed nearly vertically on top of the Fe_B, at 2.70 Å, see **Table 6.1**. The H atoms are equally separated from the S (1.35 Å), forming a bond angle of 92.3°, slightly bigger than for the isolated molecule (90°) related to a weak interaction with the oxidized surface. According to the charge analysis, the formation of the H_2S molecule is accompanied by an increase of the positive charge at the S atom (by 0.8 e^-), while the O atom reduces its negative charge by the same amount, followed by an electron rearrangement on the H_2S hydrogens. The state 6 is 0.45 eV above state 4 in the energy profile, which means that the migration of the H is less favourable than the introduction of the OH group at the surface. The activation energy of this step (E_{A2}) is 0.29 eV smaller than E_{A1} indicating that the exchange of the SH by OH group is the determinant step in this pathway. Moreover, the energies associated with the states 4, 5 and 6 show that the reverse process is thermodynamically and kinetically more favourable. Hence, in the reverse process, the dissociation of a H_2S molecule adsorbed on a partially oxidized Fe_3O_4(001) has an activation energy of 0.04 eV, just above the thermal energy ($2k_BT$) at 298 K.

H_2S desorption is an unfavourable process as state 7 is 1.06 eV above the reference. Although the H_2S desorption affects negligibly the surface structure, the charge analysis shows an increase of 0.9 e^- on the Fe_B atoms coordinated to the O, while the charge of the two S atoms, coordinated to the Fe_B site and the subsurface Fe_A, decreased by 0.6 e^-.

According to this pathway, the position for the S substitution was dictated by the most stable adsorption site of the H. Nevertheless, test calculations revealed that the substituted S atom is not the most thermodynamically prone to be substituted, but any two of them coordinating the Fe_A next to the cavity along the [110] direction. Therefore, we examined the possibility of the O diffusion towards the most stable substitution position. The solid state diffusion process stabilizes the surface slab by an additional 0.14 eV after overcoming a barrier of 2.14 eV. The high activation energy of the O diffusion suggests than this step is highly unlikely to happen in static conditions once the oxidation of the Fe_3S_4(001) surface has occurred. In the structure of this final configuration, the O atom moved outwards by 0.21 Å but still remained below the S top layer. The charge analysis of reveals that, after the O diffusion, the three surface Fe_B that were coordinating the O atom before and after this process reduce their overall charge by 0.7 e^-. This electronic transfer happens in such a way, that 0.6 e^- are drawn from two S atoms that become equally charged as the rest of the surface S atoms.

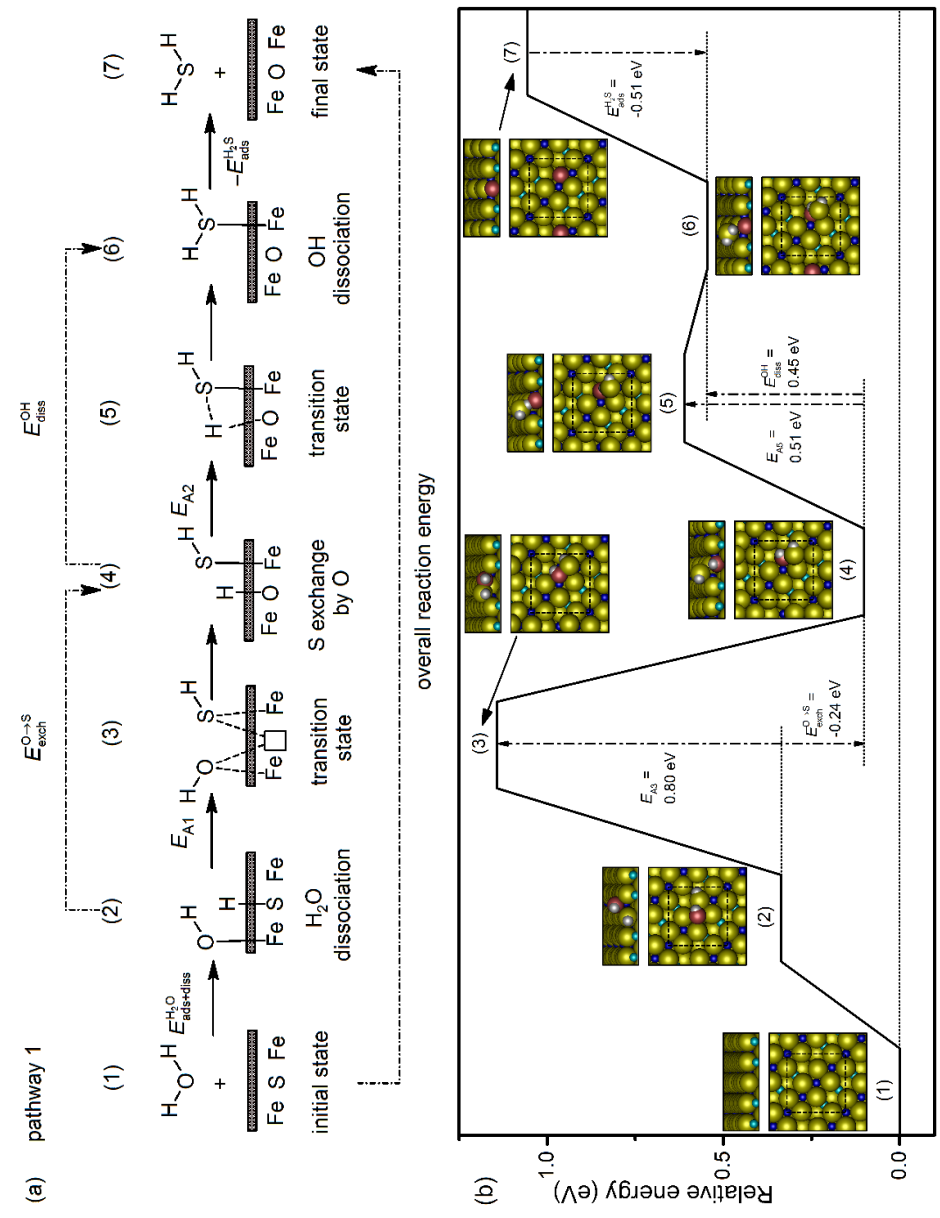

Figure 6.3. (a) Schematic representation and (b) reaction profile for the oxidation of the $Fe_3S_4(001)$ surface via pathway 1. Insets show side and top view of the structure of the numbered states. Only the surface and species adsorbed to it are shown. Light blue atoms represent Fe_A, dark blue for Fe_B, yellow for S, red for O and white for H.

6.3.2 Pathway 2

A sensible alternative of the discussed pathway is to consider the H migration away from the Fe_B−OH centre. This situation leads us to pathway 2, shown in **Figure 6.5**, which depicts the oxidation of the surface by one OH group (coverage of 0.25 ML). Note that in agreement with the reference, the states 2 to 6 energies have been calibrated by considering the energy of one proton sitting onto the most stable position on the Fe_3S_4(001) surface.

In the hydroxylated surface, the O−H distance remains the same than in the H_2O of pathway 1, both at stage 2, see **Table 6.2**. However, the Fe_B−O bond length is 0.02 Å shorter, suggesting that the OH group is bonded slightly stronger in the absence of the second H atom. Our calculations show that this state is 0.09 eV lower in energy than the equivalent stage of pathway 1, which corroborates the thermodynamic feasibility of the H migration. The charge analysis showed that 0.6 e^- were transferred from the Fe_B to the OH in agreement with this shortened bond. We also found that the absence of a proton attached nearby generates further changes on the surface electronic structure. For example, the OH-coordinated Fe_B and the three top Fe_A release 1.7 e^- overall, 88 % of which is supplied to the topmost S atoms and to the hydroxyl (the O atom is 0.9 e^- more negative than the same stage of pathway 1). This increase in the nucleophilic character makes the O more eager to coordinate cations, *i.e.* take a position on the surface and being surrounded by a higher number of Fe ions. The charge density difference of the second state is shown in **Figure 6.4**, illustrating that

much of the electronic density located between the Fe_B and O atoms originally came from the O electron lone pair.

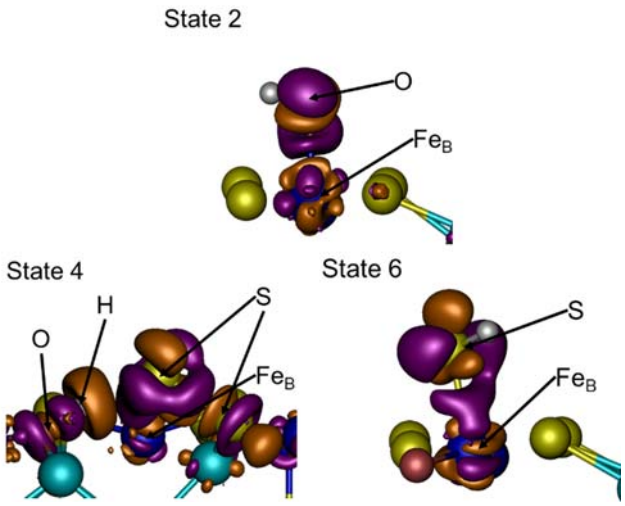

Figure 6.4. Charge density difference plot of the adsorption at different stages along the oxidation of the Fe_3S_4(001) surface following pathway 2. Isosurfaces of the difference density are displayed at a value of ±0.05 e·Å^{-3}, where purple and orange represent gain and lost electron density respectively. Light blue atoms represent Fe_A, dark blue for Fe_B, yellow for S, red for O and white for H.

Table 6.2. Calculated bond distances (Å) at different minima states along the Fe_3S_4(001) surface oxidation following pathway 2.

state	2	4	6
d(O−Fe_{B1})	1.81	--	--
d(S−Fe_{B2})	--	2.27	2.22
d(H−O)	0.98	1.00	--
d(H−S)	--	--	1.35
d(H···S)	--	2.07	--

The hydroxylated Fe_B is surrounded by four non-equivalent S atoms. In the absence of a protonated sulfur, the hydroxyl O replaces the S leading to the thermodynamic product, which is equivalent to the last configuration of pathway 1. Despite the similarities, as the replaced S atom remains unprotonated, it forms a hydrogen bond (d(H···S) = 2.07 Å) with the hydroxyl H, see state 4 on **Figure 6.5** and **Table 6.2**. The O−H bond distance is longer by 0.02 Å while the O is displaced outward the surface by 0.07 Å as well as along the [110] direction, with regard to the same stage of pathway 1. Moreover, the S atom leans towards the hydroxyl H, pushing the cation holding it across the [110] direction. The charge analysis shows a rearrangement of 0.4 e^- involving the O atom as acceptor and the replaced S as donor. The adsorbed S atom is 1.0 e^- more negative than the SH in pathway 1, which also explains its higher nucleophilicity. **Figure 6.4** shows the charge density difference plot for this stage, where it is possible to localize the charge around the adsorbed S. The energy of this state is 0.15 eV lower than the reference system, contrarily to 0.10 eV higher in pathway 1. Moreover, the activation energy required to take our system from state 2 to 4 is 0.17 eV lower than in pathway 1. The higher thermodynamic and kinetic tendency of our system to undergo the exchange step in pathway 2 is related with the absence of one water H and hence a more negatively charged hydroxyl O, which prefers higher coordination.

The next step along the oxidation process is the formation of the SH group. The protonated S moves 2.22 Å nearly straight atop the Fe_B ion, which relaxes to its original position within the atomic row along the [110] direction, see state 6 on **Figure 6.5** and **Table 6.2**. At this stage, the S−H bond length is equal to the one in the states

4 and 6 of pathway 1. Once the SH is formed, the O atom has moved horizontally along the [110] direction and 0.11 Å vertically towards the surface. An analysis of the charges reveals that after OH dissociation, the O atom together with the top Fe ions lose 0.5 e^- overall, which is supplied to the S−H bond. The charge density difference representation, shown in **Figure 6.4**, illustrates the charge distribution after the SH formation onto the partially oxidized Fe_3S_4(001) surface. The OH dissociation process is endothermic (by 0.79 eV) and kinetically unfavourable, becoming the rate limiting step, which is determined by the O nucleophilicity. Thus, the O atom prefers to sit at the S place and retain the H, leaving the surface hydroxylated. The net energy change of the O−H dissociation is more endothermic and with higher activation energy than the second dissociation in pathway 1 by 0.34 and 0.70 eV respectively.

In the final step of pathway 2, the SH group interacts with a co-adsorbed H atom, leading to the formation and desorption of the H_2S molecule. This leaves a partially oxidized surface slab identical to the one obtained after the solid state diffusion of pathway 1. We could also consider a variation of pathway 2, where the exchange of S by O takes place after the OH dissociation, see **Figure 6.5**. Nevertheless, the energies of the stationary states are higher than in the suggested pathway. Therefore, we do not describe the stationary points of this alternative mechanism as it is highly unlikely to be the one leading to the (001) surface oxidation.

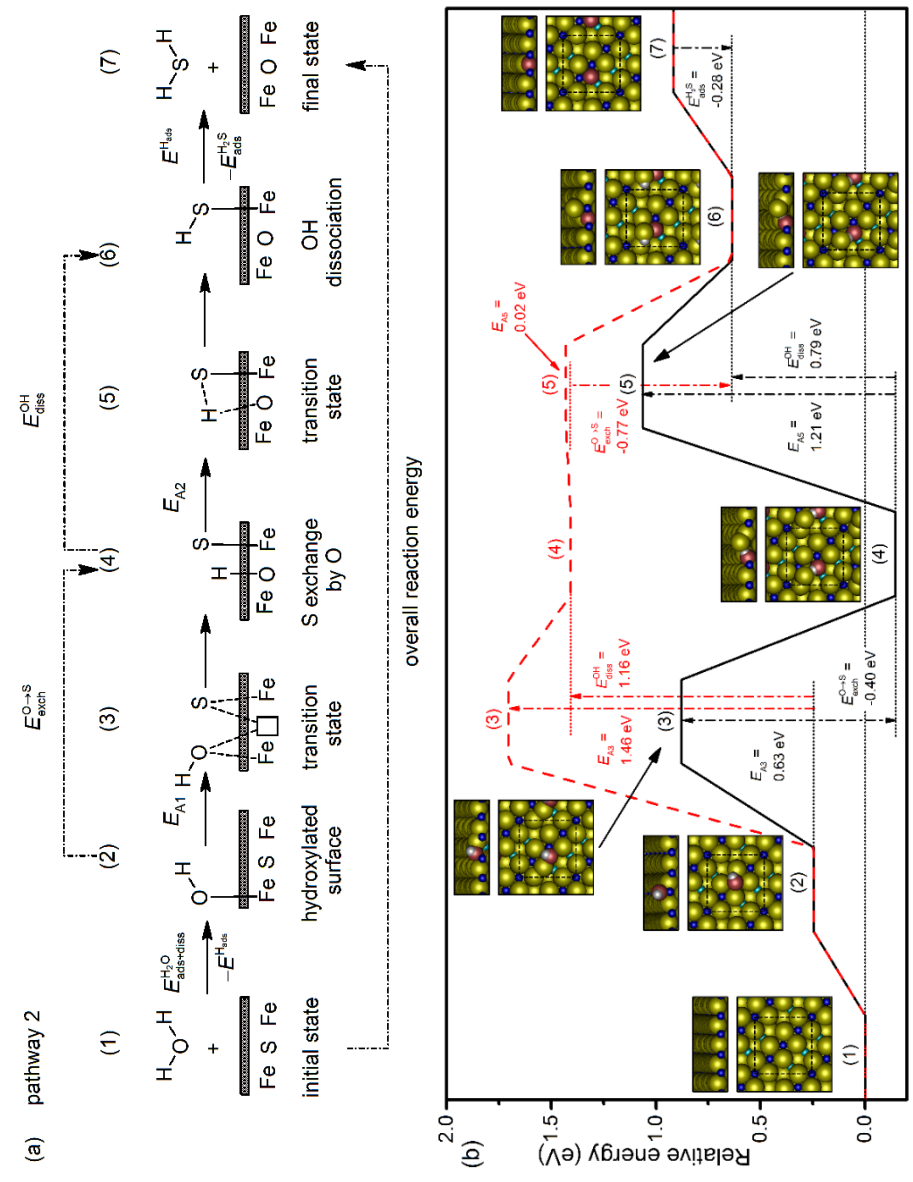

Figure 6.5. (a) Schematic representation and (b) reaction profile for the oxidation of the $Fe_3S_4(001)$ surface via pathway 2 (the red dashed line represents a variation of pathway 2 in which OH dissociation takes place first). Insets show side and top view of the structure of the numbered states. Only the surface and species adsorbed to it are shown. Light blue atoms represent Fe_A, dark blue for Fe_B, yellow for S, red for O and white for H.

6.3.3 Pathway 3

We next investigated the effect of an extra H_2O molecule (0.50 ML) on the oxidation mechanism, see **Figures 6.7** and **6.8**. Previous works on Fe_3S_4 and the analogue spinel $FeNi_2S_4$ suggested that the adsorption of a second H_2O molecule after dissociation of the first one is most likely to take place on the surface Fe_B ion next to the protonated S, see state 2 on **Figure 6.8** and **Table 6.3** (Haider *et al.*, 2014; Roldan and de Leeuw, 2015). As a result of the interaction with the surface, the bond angle of the newly added H_2O molecule is increased to 108.1°, with respect to the 104.7° calculated for the isolated molecule, which is in excellent agreement with the value obtained from microwave spectroscopy (Harmony *et al.*, 1979). The O of the second H_2O molecule is at 2.14 Å from the Fe_B ion and its O−H distances are 0.97 and 1.04 Å. While the shortest OH bond distance indicates no bond alteration (Harmony *et al.*, 1979), the elongated one is orientated towards the O atom of the neighbour OH group, forming a hydrogen bond of 1.56 Å. This makes both adsorbates, H_2O and OH, to be slightly bent with respect to the surface. Apart from the 0.10 Å elongation induced to the Fe−OH bond, the structure of the dissociatively adsorbed H_2O molecule remains essentially the same than in pathway 1, see **Table 6.3**. We found that the addition of a second H_2O molecule stabilizes the system by 0.56 eV with regard to the reference system of two isolated H_2O molecules and the pristine slab, see **Figure 6.8**. The charge density difference of the molecularly adsorbed H_2O with respect to the slab containing the dissociatively adsorbed H_2O indicates the electronic density relocation between the Fe_B and the second H_2O together with the hydrogen bond formation, see state 2 in **Figure 6.6**. The charge analysis reveals that after the molecular adsorption, the

hydrated Fe_B ion together with both O atoms release altogether 2.0 e^- which are supplied to the H_2O molecule.

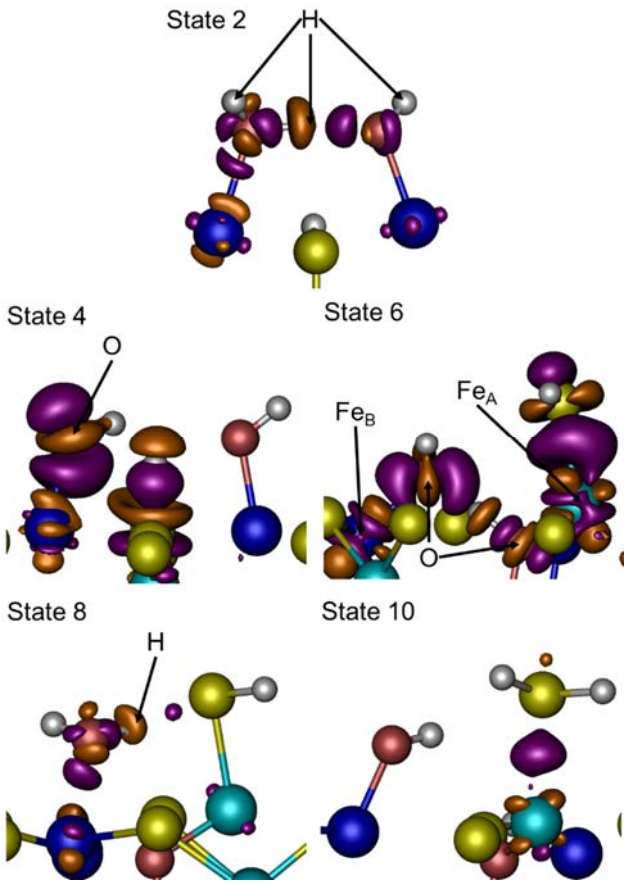

Figure 6.6. Charge density difference plot of the adsorption at different stages along the oxidation of the Fe_3S_4(001) surface following pathway 3. Isosurfaces of the difference density are displayed at a value of ±0.05 e·Å^{-3}, where purple and orange represent gain and lost electron density respectively. Light blue atoms represent Fe_A, dark blue for Fe_B, yellow for S, red for O and white for H.

Table 6.3. Calculated bond distances (Å) and angles (°) at different minima states along the Fe_3S_4(001) surface oxidation following pathway 3.

state	2	4	6	8	10	11	13
$d(O_1{-}Fe_{B1})$	1.93	1.83	1.91	2.13	1.84	1.80	1.83
$d(O_2{-}Fe_{B2})$	2.14	1.85	--	--	--	--	--
$d(S_2{-}Fe_A)$	--	--	2.23	2.27	2.45	--	--
$d(H_1{-}O_1)$	0.97	0.98	0.97	0.98	0.98	0.99	0.97
$d(H_2{-}S_1)$	1.38	1.35	1.35	1.36	1.36	1.36	1.36
$d(H_3{-}O_2)$	1.04	0.97	1.09	--	--	--	--
$d(H_3{-}S_2)$	--	--	--	--	1.35	--	--
$d(H_3{-}O_1)$	--	--	--	1.01	--	--	--
$d(H_4{-}O_2)$	0.97	--	--	--	--	--	--
$d(H_4{-}S_2)$	--	1.37	1.35	1.35	1.35		
$d(H_1{\cdots}O_2)$	--	--	--	--	--	1.77	--
$d(H_3{\cdots}O_1)$	1.56	2.53	1.38	--	--	--	--
$d(H_3{\cdots}S_2)$	--	--	--	2.20	--	--	--
$\angle H_1{-}O_1{-}H_3$	--	--	--	104.3	--	--	--
$\angle H_3{-}O_2{-}H_4$	108.1	--	--	--	--	--	--
$\angle H_3{-}S_2{-}H_4$	--	--	--	--	92.7	--	--

In order to generate a second SH group within close proximity to a subsurface Fe_A ion the dissociation of the molecular H_2O takes place, see state 4 in **Figure 6.8**. Hence, the two SH groups are bridging both hydroxylated Fe_B ions, which is a configuration similar to the one found on $FeNi_2S_4$ (Haider *et al.*, 2014). We could also consider that this dissociation takes place towards the protonated S ion, but as we showed on pathway 1, H_2S is unstable near a co-adsorbed OH as it is more basic. Hence, the new

S−H bond is nearly perpendicular to the surface and has the same bond length than the existing one, see **Table 6.3**. Likewise, the two now similarly spaced FeO bonds are more parallel than in the OH−H_2O co-adsorbed state, stretching the hydrogen bond by 0.97 Å. The weakening of the long-range hydrogen bond between the two OH groups is also expressed by the reduction of their intra bond length. The configuration with two adsorbed OH groups and two surface SH is 1.50 eV less stable than the OH−H_2O co-adsorbed state which is reached after the system overcomes an energy barrier of 1.70 eV. The charge analysis shows that dissociation of the second H_2O molecule is accompanied by the reduction of its charge by 0.9 e^-, while the S and Fe_B ions binding the dissociation products increased their charge by the same amount. The localization of charge between the S and H atoms and between the Fe_B and OH group as well as the weakening of the hydrogen bond can be seen graphically in the charge density difference plot, see state 4 in **Figure 6.6**.

The protonated S binding the subsurface Fe_A is the one most likely to be exchanged by an OH, see state 6 in **Figure 6.8**. After the exchange, the SH group is adsorbed at 2.23 Å from the Fe_A ion, see **Table 6.3**, which has also migrated outwards the surface by 1.23 Å occupying a free neighbour octahedral position. At this point, it is worth noting that 1/3 of the top Fe_A ions have high lability to move outward as their bulk-like position before relaxation of the pristine surface was just above the top S layer (Roldan and de Leeuw, 2015). The hydroxyl introduced on the Fe_3S_4 surface, like in the two previously proposed pathways, lies at 0.47 Å below the topmost atomic layer. While the S−H bond length is the same for the two SH groups, the O−H distance of the mineralized OH group is 0.12 Å larger than the one of the adsorbed OH. The

OH···OH distance of 1.38 Å indicates a hydrogen bond between these OH groups. The adsorbed OH group is, in turn, tilted towards the mineralized OH, which results in a 0.08 Å increase of the Fe_B–O distance. The absolute value of the energy released during the exchange step (1.00 eV), together with the activation energy (1.25 eV), are the largest of the three pathways we have studied for the oxidation of the Fe_3S_4(001). The charge analysis indicates a rearrangement of charges (quantified as 0.8 e^-) from the adsorbed OH group and the labile Fe_A ion to the mineralized OH and the cleared Fe_B, which can be seen graphically in the charge density difference plot of state 6 in **Figure 6.6**. This figure illustrates the localization of charge between the adsorbed OH and SH groups and the Fe ions binding them and between the mineral and adsorbed OH groups, corroborating their strong interaction.

In the next step takes place the formation a co-adsorbed H_2O molecule from the adsorbed OH, which receives the H atom from the mineralized OH group, see state 8 in **Figure 6.8**. This process requires 0.33 eV after overcoming an activation energy barrier of 0.36 eV, making it the less demanding step in this study, perhaps due to the equal nature of the donor and acceptor atoms. After the H migration step, the surface O atom moves inward by 0.09 Å while the H_2O elongates 0.22 Å its distance with the Fe_B, lying almost as an isolated molecule (Harmony *et al.*, 1979), see **Table 6.3**. The H_2O is tilted towards the adsorbed SH group, stablishing a weak hydrogen bond, d(HOH···SH) = 2.20 Å. The charge analysis reveals that after the H_2O formation step, the migrating H and the mineral O ion have regained 0.8 e^- and that 79% of it was drawn from the adsorbed OH group. The charge density difference plot of the adsorbed H_2O molecule with respect to the partially oxidized surface with both SH groups, see

state 8 in **Figure 6.6**, illustrates the localization of electronic density in the H_2O−Fe_B bond as well as in the HOH···SH hydrogen bond.

In the final step of the H_2S formation, one of the H atoms from the H_2O migrates to the SH group, see state 10 in **Figure 6.8**. This process is endothermic by 0.47 eV and its transition state has an energy barrier of 1.09 eV in agreement with their relative pKa. At this stage, the S of the H_2S molecule moves 0.18 Å outwards and the Fe_B−O distance is reduced by 0.29 Å, see **Table 6.3**. The calculated bond angle of the adsorbed H_2S molecule is 92.7° and the two S−H bond distances are 1.35 Å. This geometry is very close to the one calculated for the isolated molecule (92.1° and 1.35 Å respectively) and found from microwave spectroscopy (92.1° and 1.34 Å respectively) (Harmony *et al.*, 1979). These results highlight the weak interaction between the H_2S molecule and the partially oxidized surface. The charge analysis shows that after H_2S formation, the migrating H leaves behind 0.7 e^-, which results in the decrease of the charge of the adsorbed OH group and the increase of the charge of the SH group. The state 10 of **Figure 6.6** shows the charge density difference plot of the H_2S molecule with respect to the partially oxidized surface containing the dissociated H_2O, where we can notice a higher charge localization between H_2S and the Fe_A than in the state 6 of pathway 1 (**Figure 6.2**).

Desorption of the H_2S molecule requires an energy of 0.74 eV, see state 11 in **Figure 6.8**. The release of the H_2S molecule is accompanied by the formation of a hydrogen bond (at 1.77 Å) between the OH group and the mineral O atom, see **Table 6.3**. Nevertheless, the impact on the structure is minimal. A Bader analysis of the charges

reveals that after H_2S desorption, the mineral O atom has donated 0.2 e^- of negative charge and that 50% of it was taken by the H_2S molecule.

Unlike in pathways 1 and 2, the presence of the adsorbed OH group and the labile Fe_A that moved to an octahedral site, makes the most stable oxidation product to be found when the mineral O diffuses and takes the place of the neighbour S on the same raw of the $[\bar{1}\bar{1}0]$ direction. This process further stabilizes the surface by a 0.40 eV, which is nearly 3 times more exothermic than the diffusion process of pathway 1. However, the barrier of the transition state in pathway 3 is 6.6 times higher than in pathway 1, making this solid state transformation step much less likely than in pathway 1. In the final configuration, the O is at 0.44 Å below the level of the surface atomic layer, which is comparable with the outcome of the previously discussed pathways. There is, however, a lasting impact of the oxidation through the last mechanism on the position of the labile Fe_A ion, which remains in the octahedral cavity. The charge analysis indicates that the Fe_A and Fe_B ions coordinating the O have altogether lost 0.6 e^-, a charge that was given to the same type of atoms coordinated to the O atom prior to its diffusion.

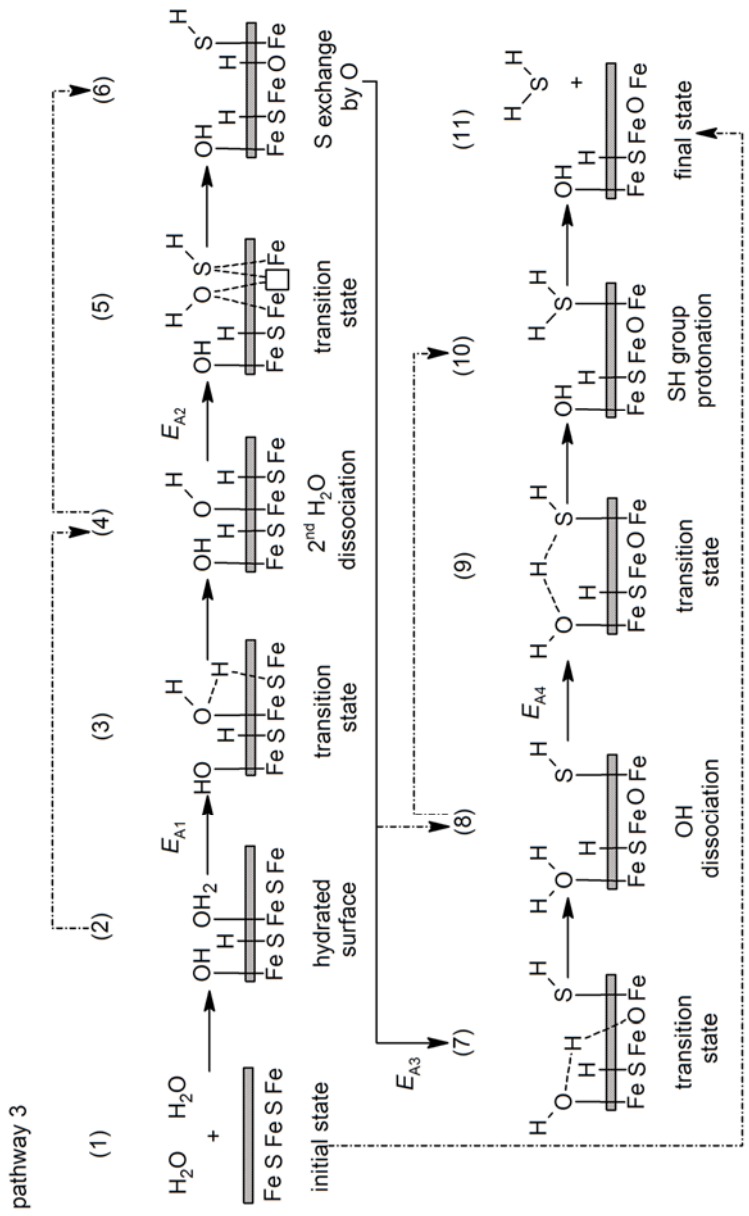

Figure 6.7. Schematic representation or the oxidation of the Fe_3S_4(001) surface via pathway 3. Only the surface and species adsorbed to it are shown.

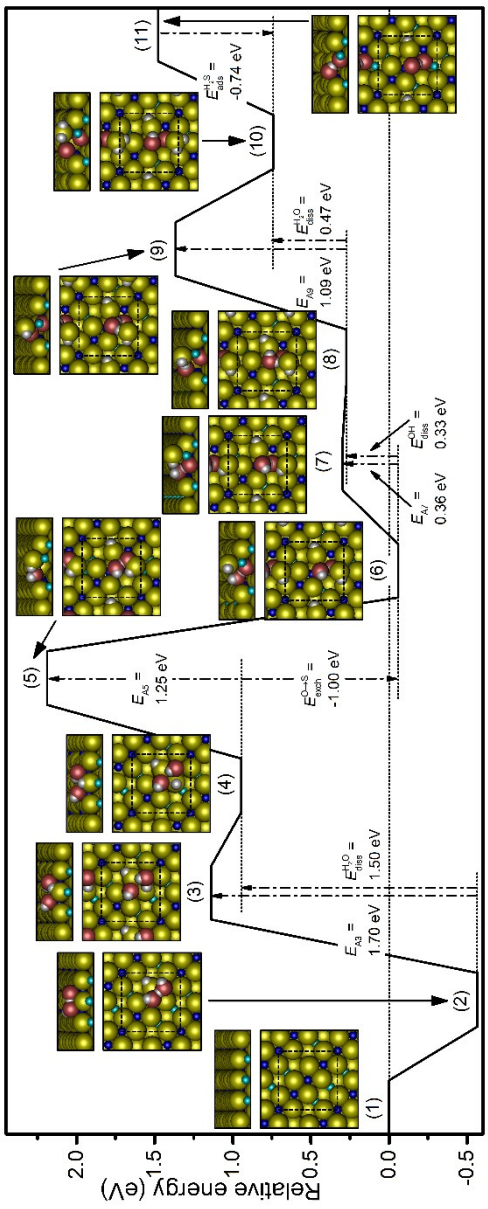

Figure 6.8. Reaction profile for the oxidation of the $Fe_3S_4(001)$ surface via pathway 3. Insets show side and top view of the structure of the numbered states. Only the surface and species adsorbed to it are shown. Light blue atoms represent Fe_A, dark blue for Fe_B, yellow for S, red for O and white for H.

6.3.4 Thermodynamics of H_2S and its ionization products in aqueous solution

Because of the interest in preventing the H_2S release from iron-sulfur compounds, and hence the acid mine drainage, we investigated the equilibrium concentration of these species in aqueous solution. We have calculated the concentration of aqueous H_2S from the oxidation of the Fe_3S_4(001) surface and the pH of this solution as a function of temperature, in the range from 293 to 373 K. In order to calculate the concentrations of the species in aqueous solution in equilibrium with the pristine and partially oxidized Fe_3S_4(001) surfaces, we considered the process of partial oxidation of this surface by a H_2O molecule, according to the following equation:

$$Fe_{24}S_{32}(s) + H_2O(l) \underset{\longleftarrow}{\overset{K_{o1}}{\longrightarrow}} Fe_{24}S_{31}O(s) + H_2S(aq) \qquad (6.2)$$

where the equilibrium constant (K_{o1}) is equal to the [H_2S] in equilibrium with the solid phases.

H_2S is a diprotic acid with two dissociation steps. The ionization constant of the first dissociation, represented by equation (6.3), is written as $K_{a1} = [H^+]\cdot[SH^-]\cdot[H_2S]^{-1}$ and its dependence with T at saturated water vapour pressure is shown in **Table 6.4**. We do not consider the second dissociation of H_2S as its constant K_{a2} (Suleimenov and Seward, 1997) is at least 8 orders of magnitude smaller than K_{a1} (Giggenbach, 1971) for the range of temperature considered. We are also ignoring the autodissociation of H_2O as its ionic product, K_W, is also at least 6 orders of magnitude smaller than K_{a1} in the range of temperatures of interest (Haynes, 2012). Consequently, the [H^+] is

controlled by the first dissociation of H_2S and the contribution of H^+ from the other processes is negligible.

$$H_2S(aq) \overset{K_{a1}}{\rightleftharpoons} H^+(aq) + SH^-(aq) \tag{6.3}$$

In order to link the gas phase state of the isolated molecules in our DFT simulations with the states in equation (6.2), we have considered the vapour pressure of H_2O in equilibrium with its condensed phase and the solubility of gaseous H_2S in water.

The vapour pressure is the partial pressure of a given gas above which, at constant temperature, the substance is going to condense into the liquid phase. This saturation property is a function of temperature and its empirical expression for H_2O is represented in **Table 6.4** (p_{H_2O}) while the equilibrium of H_2O between its liquid and gas states is shown in equation (6.4). This property increases with temperature and when it equals the total external pressure, the compound starts to boil.

$$H_2O(l) \overset{p_{H_2O}}{\rightleftharpoons} H_2O(g) \tag{6.4}$$

The solubility of a given gas in a given liquid is controlled by the Henry constant. This constant is a coefficient of proportionality between the partial pressure of the gas and the amount of it that can be dissolved in a given volume of the solvent at constant temperature. The Henry constant also depends on the temperature and the empirical expression for the solubility of H_2S in H_2O is represented in **Table 6.4** (K_{H_2S}), while the equilibrium can be written as equation (6.5) and the equilibrium constant is $K_{H_2S} = [H_2S] \cdot p_{H_2S}^{-1}$.

$$H_2S(g) \xrightleftharpoons{K_{H_2S}} H_2S(aq) \tag{6.5}$$

The combination of equations (6.2), (6.4) and (6.5), leads to the reaction of the partial oxidation of Fe_3S_4(001) surface where H_2O and H_2S are in the reference state of our DFT calculations:

$$Fe_{24}S_{32}(s) + H_2O(g) \xrightleftharpoons{K_o} Fe_{24}S_{31}O(s) + H_2S(g) \tag{6.6}$$

Table 6.4. Empirical expressions for the first ionization constant of H_2S (K_{a1}), vapour pressure of H_2O (p_{H_2O}) and Henry constant of H_2S (K_{H_2S}) as a function of the absolute temperature.

equation for constant	units of constant
$\lg(K_{a1}) = a_1 + a_2 T + a_3 T^2 + a_4 T^{-1} + a_5 \ln(T)$ $a_1 = 782.43945$ $a_4 = -20565.7315$ $a_2 = 0.361261$ $a_5 = -142.741722$ $a_3 = -1.6722 \cdot 10^{-4}$	molality[A]
$\ln(p_{H_2O}) = \frac{T_c}{T}\left[b_1\tau + b_2\tau^{1.5} + b_3\tau^3 + b_4\tau^{3.5} + b_5\tau^4 + b_6\tau^{7.5}\right] + \ln(p_c)$ $T_c = 647.096$ K $b_2 = 1.84408259$ $p_c = 2.2064 \cdot 10^7$ Pa $b_3 = -11.7866497$ $\tau = 1 - \theta$ $b_4 = 22.6807411$ $\theta = \frac{T}{T_c}$ $b_5 = -15.9618719$ $b_1 = -7.85951783$ $b_6 = 1.80122502$	Pa[B]
$\lg(K_{H_2S}) = c_1 + c_2 T + c_3 T^2 + c_4 T^{-1} + c_5 \lg(T)$ $c_1 = -0.6342702616 \cdot 10^3$ $c_4 = 0.1671907660 \cdot 10^5$ $c_2 = -0.2709284796$ $c_5 = 0.2619219571 \cdot 10^3$ $c_3 = 0.1113202904 \cdot 10^{-3}$	molality/bar[C]

[A] Suleimenov and Seward (1997)

[B] Wagner and Pruss (1993)

[C] Suleimenov and Krupp (1994)

K_o is then calculated as shown in equation (6.7), from the Gibbs free energy (G) of the partial oxidation of the Fe_3S_4(001) surface, where R and T are the ideal gas constant and the temperature of interest respectively.

$$K_o = \frac{p_{H_2S}}{p_{H_2O}} = \frac{K_{o1}}{K_{H_2S} \cdot p_{H_2O}} = e^{-\Delta G^{\ominus}/RT} \tag{6.7}$$

The change in the standard Gibbs free energy ($\Delta G^{\ominus}$) for the partial oxidation of the Fe_3S_4(001) surface according to equation (6.7) was calculated from $\Delta G^{\ominus} = \Delta H^{\ominus} - T\Delta S^{\ominus}$, where $\Delta H^{\ominus}$ is the enthalpy of this process, per H_2S molecule formed, $\Delta S^{\ominus}$ is the change in entropy and T is the temperature. The enthalpies for the initial oxidation of the (001) surface according to the three pathways investigated in this study are obtained directly from our calculations assuming that their values, strictly calculated at T = 0 K, will not depend appreciably on the temperature. We additionally assumed that the entropies of the solid phases remain largely unchanged through the oxidation reaction and that only the change in entropy due to the replacement of one of the gaseous H_2O by one H_2S molecule is necessary to take into account. Similar considerations have been used to explain the dehydration of a number of α-FeO(OH) and α-Fe_2O_3 surfaces (de Leeuw and Cooper, 2007) and the dissolution/nucleation process at the α-quartz (0001) surface in liquid H_2O (Du and de Leeuw, 2006). We have used the entropies of H_2O and H_2S calculated at different temperatures using statistical thermodynamics (Dzade *et al.*, 2013; Roldán *et al.*, 2010; Stoltze, 2000). For the range of temperature between 250 and 425 K, the maximum error between the calculated and previously reported (Chase, 1998) entropy are 2.8 and 0.3 % for H_2S and H_2O respectively, see **Figure 6.9**. Combining K_o with K_{H_2S} and p_{H_2O}, as shown in equation (6.7), it is possible to determine the reaction constant K_{o1} and therefore [H_2S] and the pH as a function of the temperature when H_2O is in the liquid state and H_2S is dissolved in water.

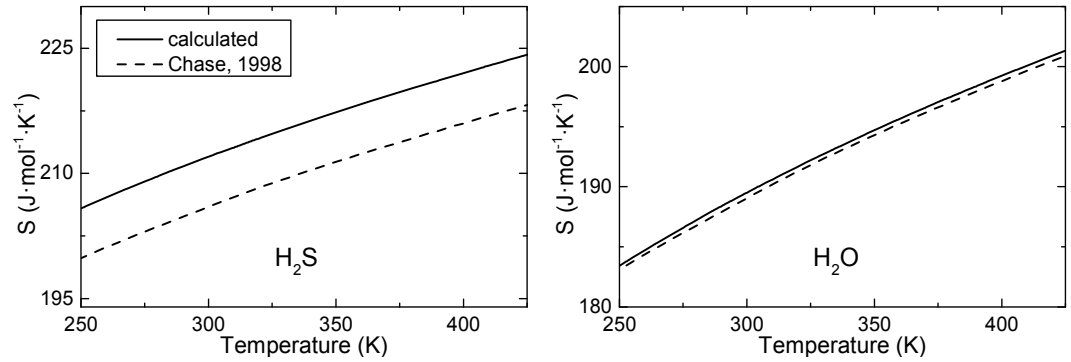

Figure 6.9. Comparison of the entropy as a function of temperature reported by Chase (1998) and calculated using statistical thermodynamics for gaseous H_2S and H_2O.

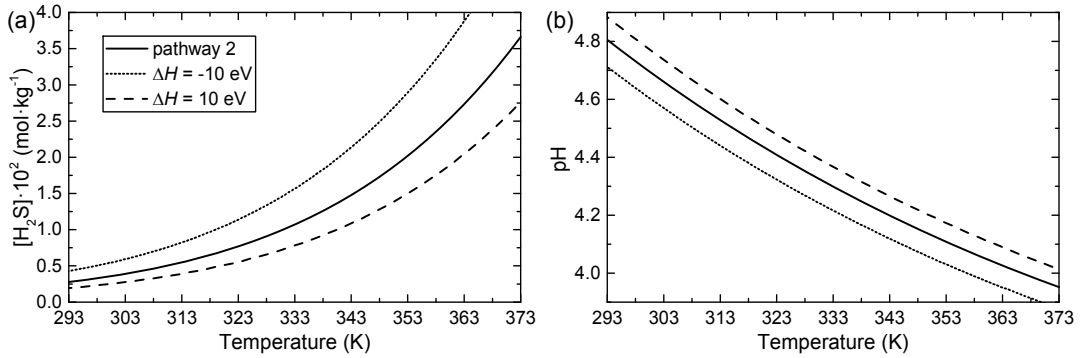

Figure 6.10. Calculated dependence of (a) $[H_2S]$ and (b) pH with respect to *T* for the partial oxidation of the Fe_3S_4(001) surface following pathway 2. The dotted and dashed lines are added for comparison porpoises and they represent processes with $\Delta H^{\ominus} = -10$ and 10 eV respectively.

The partial oxidation of the Fe_3S_4(001) surface in a wet environment, represented by the concentration of H_2S as a function of the temperature, is shown in **Figure 6.10 (a)**. This graph only shows the curve associated with pathway 2 ($\Delta H^{\ominus} = -0.92$ eV), which is the most kinetically and thermodynamically favourable, since the curves related with the rest of the pathways are almost coincident with this. As expected of an

endothermic process, the increment of temperature brings an exponential increase of the concentration of products: [H_2S] is equal to $2.77 \cdot 10^{-3}$ mol·kg^{-1} at T = 293 K and $3.65 \cdot 10^{-2}$ mol·kg^{-1} at T = 393 K. **Figure 6.10 (b)** shows how the pH decreases with temperature as it is also expected from a solution with an increasing concentration of a weak acid. In **Figure 6.10 (a)** and **(b)**, we have also added two auxiliary lines showing the behaviour of hypothetical pathways whose $\Delta H^{\ominus}$ are ±10 times bigger than pathway 2. These lines illustrate how noticeably the enthalpy of the process affects the dependence of [H_2S] and pH with T. Since the pH is always below 4.81 in the range of temperatures from 293 K to 373 K and large Fe_3S_4 deposits are present in aquatic environments, from our calculations it would appear that this mineral deposits could be significant contributors to acid mine drainage.

6.4 Chapter conclusions

In this paper, we have proposed and modelled three different pathways for the early steps of the oxidation of the Fe_3S_4(001) surface promoted by H_2O. We used DFT methods with a Hubbard Hamiltonian and empirical long-range dispersion corrections to optimize the geometry of any intermediate in the thermodynamic and kinetic energy profile. In each of these mechanisms, one surface S atom is replaced by an O atom from H_2O, producing one H_2S molecule. We found that the step where the OH group replaces the S atom always take place before the OH losses its H atom. However, for the pathway 2, we could model the alternative reaction route and we found that all intermediates were between 1.56 and 0.37 eV higher in energy than in the OH

mineralization mechanism, which agrees with suggested mechanisms on sulfides. We have found that pathways 1 and 2 are the most effective routes to initiate the oxidation of the Fe_3S_4(001) surface. Although in pathway 1 the total $\Delta H^{\ominus}$ (per H_2S molecule formed) is 0.14 eV higher than in pathway 2, the rate-determining step in pathway 1 is 0.41 eV smaller than in pathway 2. The presence of the dissociated H^+ from the H_2O on the vicinities of the reactive site on pathway 1 directs the oxidation reaction towards a kinetic product where the exchange of S by O becomes the step with highest activation energy. On the other hand, as the dissociated H^+ is absent from the vicinities of the reactive site on pathway 2, the oxidation product obtained directly is the most thermodynamic favourable and the O−H dissociation step becomes the rate-limiting one. When two H_2O molecules are adsorbed around the reactive centre, pathway 3, they direct the oxidation reaction to a kinetic product, which is 0.42 eV higher in energy than the one obtained in pathway 1. Moreover, the highest activation energy calculated in this study is associated with the dissociation of the second H_2O molecule in pathway 3, making it unlikely. The calculated [H_2S] in aqueous solution, and therefore pH, in chemical equilibrium with the solid phases at a range of temperatures, show that Fe_3S_4 may be amongst those minerals responsible for the AMD.

7

Conclusions and future works

7.1 Conclusions

We have presented a computational study of the inversion thermodynamics, the electronic and magnetic properties of FeM_2X_4 (thio)spinels; the mechanical and surface redox properties of Fe_3O_4 as well as the oxidation of the Fe_3S_4(001) surface, using first principles methods based on the density functional theory.

The thermodynamic inversion degree determined for the FeM_2X_4 (thio)spinels at temperatures used typically in their synthesis agrees reasonably well with the experimental evidence, wherever this exists. The analysis of the configurational free energies showed that different behaviors are expected for the equilibrium cation distributions in these structures: $FeCr_2X_4$ and $FeMn_2S_4$ are fully normal, $FeNi_2X_4$ and $FeCo_2S_4$ are intermediate, and $FeCo_2O_4$ and $FeMn_2O_4$ are fully inverted. We also found that $FeMn_2O_4$ presents a metastable intermediate inversion degree, which may be kinetically controlled. We found that none of the factors analyzed, *i.e.* the size of the ions and the crystal field stabilization effects, play a significant role in determining the equilibrium inversion degree of these compounds. We discussed how the electronic and magnetic structure of these spinels is modified by the degree of inversion, assuming that this could be varied from the equilibrium value. We obtained

electronic densities of states for the completely normal and completely inverse cation distribution of each compound. $FeCr_2X_4$, $FeMn_2X_4$, $FeCo_2O_4$ and $FeNi_2O_4$ are half-metals in the ferrimagnetic state when Fe is in tetrahedral positions. When *M* is filling the tetrahedral positions, the Cr containing compounds and $FeMn_2O_4$ are half-metallic systems, while the Co and Ni spinels are insulator. The Co and Ni sulfide counterparts are metallic for any inversion degree together with the inverse $FeMn_2S_4$. Our calculations suggest that the spin filtering properties of the FeM_2X_4 (thio)spinels could be modified via the control of the cation distribution by the synthesis conditions.

We investigated the elastic constants and other macroscopic properties of Fe_3O_4 by applying elastic strains on the unit cell of this compound. The calculated properties are shown to be in excellent agreement with experiments. The comparison of the mechanical properties calculated for Fe_3O_4 with those reported for its sulfide counterpart Fe_3S_4 indicates that the oxide is harder than the sulfide, but less liable to fracture. The mechanical properties also showed that the Fe−O interaction is more ionic in Fe_3O_4 than the Fe−S interaction in Fe_3S_4.

We have studied the geometries and surface free energies of a number of surfaces of Fe_3O_4 at different compositions, including the stoichiometric plane, and those with a deficiency or excess of oxygen atoms. The most stable surfaces are the (001) and (111), leading to a cubic Fe_3O_4 crystal morphology with truncated corners under equilibrium conditions. The scanning tunnelling microscopy images of the different terminations of the (001) and (111) stoichiometric surfaces were calculated. The Fe_3O_4 morphology, together with the STM images of the surfaces expressed in it, were compared with

previous reports and found to be in excellent agreement with them. Our calculations showed that under reducing conditions, the creation of oxygen vacancies in the surface leads to the formation of reduced Fe species in the surface in the vicinity of the vacant oxygen. The (001) surface is slightly more prone to reduction than the (111), due to the higher stabilisation upon relaxation of the atoms around the oxygen vacancy, but molecular oxygen adsorbs preferentially at the (111) surface. In both oxidized surfaces, the oxygen atoms are located on bridge positions between two surface iron atoms, from which they attract electron density. The oxidised state is thermodynamically favourable with respect to the stoichiometric surfaces under ambient conditions, although not under the conditions when bulk Fe_3O_4 is thermodynamically stable with respect to Fe_2O_3. This finding is important in the interpretation of the catalytic properties of Fe_3O_4 due to the presence of oxidised species under experimental conditions.

Finally, we have investigated the replacement of one sulfur (forming H_2S) by one oxygen atom (provided by H_2O) at the $Fe_3S_4(001)$ surface. We have proposed three pathways for the oxidation of this surface at different levels of H_2O coverage. One or two H_2O molecules on this surface give different intermediate oxidation products followed by diffusion of the introduced O atom towards the most stable position, while the OH group gives the thermodynamic product directly. Low levels of H_2O coverage seems to be essential to give the overall most favourable energetic landscape for the oxidation of the $Fe_3S_4(001)$ surface. When the concentration of H_2S and H^+, in aqueous solution and thermodynamic equilibrium with the stoichiometric and partially oxidized $Fe_3S_4(001)$ surface, is plotted against the temperature, taking into account

statistical entropies calculated for H_2S and H_2O and other experimental parameters, it appears that this mineral may well be among those responsible for the generation of acid mine drainage when it is exposed to weathering conditions.

The research presented in this thesis has provided a theoretical rationalization for a number of known structural, bulk and surface properties of Fe_3O_4 and related spinel-structured materials. We have also postulated a theoretical spinel structure for $FeMn_2S_4$ and $FeCo_2S_4$ and predicted their equilibrium inversion degree and electronic and magnetic properties.

7.2 Future works

Having investigated the inversion thermodynamics of the $Fe\mathit{M}_2\mathit{X}_4$ spinel-structured materials, where we proposed a theoretical spinel structure for $FeMn_2S_4$ and $FeCo_2S_4$, we would like now to further this research by studying the mixing thermodynamics in Fe/Co and Fe/Mn thiospinels. We would also like to extend the investigation of the surface properties of Fe_3O_4 by studying the interaction of its low index surfaces with small molecules such as H_2O and CO_2, with the final aim of modelling the surface carbonation and CO_2 conversion. A final direction for future research steaming from this thesis is the simulation of the oxidation of the rest of the low index surfaces of Fe_3S_4, considering O_2 and a mixture of O_2 and H_2O as oxidants.

References

Addadi, L., Weiner, S., 1992. Control and Design Principles in Biological Mineralization. Angew. Chemie Int. Ed. English 31, 153–169.

Aika, K., Yamaguchi, J., Ozaki, A., 1973. Ammonia Synthesis over Rhodium, Iridium and Platinum Promoted by Potassium. Chem. Lett. 2, 161–164.

Ainsworth, R.I., Di Tommaso, D., de Leeuw, N.H., 2011. A density functional theory study of structural, mechanical and electronic properties of crystalline phosphorus pentoxide. J. Chem. Phys. 135, 234513.

Akcil, A., Koldas, S., 2006. Acid Mine Drainage (AMD): causes, treatment and case studies. J. Clean. Prod. 14, 1139–1145.

Alexandrov, K.S., Ryzhova, T. V., 1961. The elastic properties of crystals. Sov. Phys. Crystallogr. USSR 6, 228 – 252.

Almquist, J.A., Crittenden, E.D., 1926. A Study of Pure-Iron and Promoted-Iron Catalysts for Ammonia Synthesis. Ind. Eng. Chem. 18, 1307–1309.

Andersen, O.K., 1975. Linear methods in band theory. Phys. Rev. B 12, 3060–3083.

Andersson, D.A., Stanek, C.R., 2013. Mixing and non-stoichiometry in Fe-Ni-Cr-Zn-O spinel compounds: density functional theory calculations. Phys. Chem. Chem. Phys. 15, 15550 – 15564.

Ángyán, J.G., Jansen, G., Loss, M., Hättig, C., Heß, B.A., 1994. Distributed polarizabilities using the topological theory of atoms in molecules. Chem. Phys. Lett. 219, 267–273.

Anisimov, V.I., Korotin, M.A., Zaanen, J., Andersen, O.K., 1992. Spin bags, polarons, and impurity potentials in $La_{2-x}Sr_xCuO_4$ from first principles. Phys. Rev. Lett. 68, 345 – 348.

Anisimov, V.I., Zaanen, J., Andersen, O.K., 1991. Band theory and Mott insulators: Hubbard U instead of Stoner I. Phys. Rev. B 44, 943–954.

Anthony, J.W., Bideaux, R.A., Bladh, K.W., Nichols, M.C. (Eds.), n.d. Handbook of Mineralogy. Mineralogical Society of America, Chantilly, VA 20151-1110, USA.

Aparicio, L.M., Dumesic, J.A., 1994. Ammonia Synthesis Kinetics: Surface Chemistry, Rate Expressions, and Kinetic Analysis. Top. Catal. 1, 233–252.

Appl, M., 2012. Ammonia, 2. Production Processes. In: Ullmann's Encyclopedia of Industrial Chemistry. Wiley-VCH Verlag GmbH & Co. KGaA, Weinheim, pp. 139–225.

Arai, T., Takeda, H., Warren, P.H., 1996. Four Lunar Mare Meteorites: Crystallization Trends of Pyroxenes and Spinels. Meteorit. Planet. Sci. 31, 877–892.

Armstrong, E.F., Hilditch, T.P., 1920. A Study of Catalytic Actions at Solid Surfaces. IV. The Interaction of Carbon Monoxide and Steam as Conditioned by Iron Oxide and by Copper. Proc. R. Soc. A Math. Phys. Eng. Sci. 97, 265–273.

Arnold, R.G., Malik, O.P., 1974. Violarite in Some Nickel Ores from Lynn Lake and Thompson, Manitoba, and Sudbury, Ontario, Canada. Can. Mineral. 12, 320–326.

Bacchella, G.L., Pinot, M., 1964. Étude sur la structure magnétique de $FeCr_2O_4$. Le J. Phys. 25, 537 – 541.

Bader, R., 1994. Principle of stationary action and the definition of a proper open system. Phys. Rev. B 49, 13348–13356.

Bader, R.F.W., 1990. Atoms in Molecules: A Quantum Theory. Oxford University Press, Oxford (UK).

Bader, R.F.W., Gillespie, R.J., MacDougall, P.J., 1988. A physical basis for the VSEPR model of molecular geometry. J. Am. Chem. Soc. 110, 7329–7336.

Bader, R.F.W., Popelier, P.L.A., Keith, T.A., 1994. Theoretical Definition of a Functional Group and the Molecular Orbital Paradigm. Angew. Chemie Int. Ed. English 33, 620–631.

Baldereschi, A., 1973. Mean-Value Point in the Brillouin Zone. Phys. Rev. B 7, 5212 – 5215.

Balke, B., Wurmehl, S., Fecher, G.H., Felser, C., Kübler, J., 2008. Rational design of new materials for spintronics: Co_2FeZ (Z =Al, Ga, Si, Ge). Sci. Technol. Adv. Mater. 9, 014102.

Banks, D., Younger, P.L., Arnesen, R.-T., Iversen, E.R., Banks, S.B., 1997. Mine-water chemistry: the good, the bad and the ugly. Environ. Geol. 32, 157–174.

Bare, S.R., Strongin, D.R., Somorjai, G.A., 1986. Ammonia Synthesis over Iron Single-Crystal Catalysts: The Effects of Alumina and Potassium. J. Phys. Chem. 90, 4726–4729.

Barth, T.F.W., Posnjak, E., 1932. Spinel structures: with and without variate atom equipoints. Zeitschrift für Krist. - Cryst. Mater. 82, 325 – 341.

Bazylinski, D.A., Moskowitz, B.M., 1998. Microbial biomineralization of magnetic iron minerals: microbiology , magnetism and environmental significance. In: Banfield, J.F., Nealson, K.H. (Eds.), Geomicrobiology: Interactions between Microbes and Minerals - Volume 35. Mineralogical Society of America, Washington DC, pp. 181 – 223.

Benning, L.G., Wilkin, R.T., Barnes, H.L., 2000. Reaction pathways in the Fe–S system below 100°C. Chem. Geol. 167, 25–51.

Berdunov, N., Murphy, S., Mariotto, G., Shvets, I.V., 2004a. Room temperature study of a strain-induced electronic superstructure on a magnetite (111) surface. Phys. Rev. B 70, 085404.

Berdunov, N., Murphy, S., Mariotto, G., Shvets, I. V., 2004b. Atomically Resolved Spin-Dependent Tunneling on the Oxygen-Terminated Fe_3O_4 (111). Phys. Rev. Lett. 93, 057201.

Berner, R.A., 1970. Sedimentary pyrite formation. Am. J. Sci. 268, 1–23.

Berner, R.A., 1984. Sedimentary pyrite formation: An update. Geochim. Cosmochim. Acta 48, 605–615.

Blakemore, R., 1975. Magnetotactic bacteria. Science 190, 377–379.

Blasse, G., 1963. No Title. Phil. Res. Rep. 18, 383.

Blesa, M.A., Mijalchik, M., Villegas, M., Rigotti, G., 1986. Transformation of akaganeite into magnetite in aqueous hydrazine suspensions. React. Solids 2, 85–94.

Bloch, F., 1929. Über die Quantenmechanik der Elektronen in Kristallgittern. Zeitschrift für Phys. 52, 555–600.

Blöchl, P.E., 1994. Projector augmented-wave method. Phys. Rev. B 50, 17953 – 17979.

Blöchl, P.E., Jepsen, O., Andersen, O.K., 1994. Improved tetrahedron method for Brillouin-zone integrations. Phys. Rev. B 49, 16223–16233.

Bogdandy, L. V., Schulz, H.P., Stranski, I.N., Würzner, B., 1963. Über den Reduktionsmechanismus von Eisenoxyden. Berichte der Bunsengesellschaft für Phys. Chemie 67, 958–964.

Bond, G.C., 1974. Heterogeneous Catalysis; Principles and Applications. Clarendon Press, Oxford.

Booy, M., Swaddle, T.W., 1978. Hydrothermal preparation of magnetite from iron chelates. Can. J. Chem. 56, 402–403.

Bordács, S., Varjas, D., Kézsmárki, I., Mihály, G., Baldassarre, L., Abouelsayed, A., Kuntscher, C.A., Ohgushi, K., Tokura, Y., 2009. Magnetic-Order-Induced Crystal Symmetry Lowering in ACr_2O_4 Ferrimagnetic Spinels. Phys. Rev. Lett. 103, 077205.

Born, M., Oppenheimer, R., 1927. Zur Quantentheorie der Molekeln. Ann. Phys. 389, 457–484.

Boucher, B., Buhl, R., Perrin, M., 1969. Magnetic Structure of Iron Manganite by Neutron Diffraction. J. Appl. Phys. 40, 1126–1127.

Bowen, G.G., Dussek, C., Hamilton, R.M., 1998. Pollution resulting from the abandonment and subsequent flooding of Wheal Jane Mine in Cornwall, UK. Geol. Soc. London, Spec. Publ. 128, 93–99.

Brabers, V.A.M., 1995. Progress in Spinel Ferrite Research. In: Buschow, K.H.J. (Ed.), Handbook of Magnetic Materials. Volume 8. Elsevier Science B.V., Amsterdam, pp. 189 – 324.

Bradley, J.P., Harvey, R.P., McSween Jr., H.Y., 1996. Magnetite whiskers and platelets in the ALH84001 Martian meteorite: Evidence of vapor phase growth. Geochim. Cosmochim. Acta 60, 5149–5155.

Bragg, W.H., 1915. The Structure of Magnetite and the Spinels. Nature 95, 561–561.

Bridger, G.W., Snowden, C.B., 1970. Ammonia synthesis catalysis. In: Catalyst Handbook. Wolfe Scientific Books, pp. 126–147.

Bučko, T., Hafner, J., Lebègue, S., Ángyán, J.G., 2010. Improved description of the structure of molecular and layered crystals: ab initio DFT calculations with van der Waals corrections. J. Phys. Chem. A 114, 11814–24.

Bučko, T., Lebègue, S., Hafner, J., Ángyán, J., 2013. Tkatchenko-Scheffler van der Waals correction method with and without self-consistent screening applied to solids. Phys. Rev. B 87, 064110.

Buhl, R., 1969. Manganites spinelles purs d'elements de transition preparations et structures cristallographiques. J. Phys. Chem. Solids 30, 805–812.

Bunch, T.E., Keil, K., Snetsinger, K.G., 1967. Chromite composition in relation to chemistry and texture of ordinary chondrites. Geochim. Cosmochim. Acta 31, 1569–1582.

Burke, K., Perdew, J.P., Levy, M., 1995. Semilocal Density Functionals for Exchange and Correlation: Theory and Applications. In: Seminario, J.M., Politzer, P. (Eds.), Modern Density Functional Theory - A Tool for Chemistry - Volume 2. Elsevier B.V., Amsterdam, pp. 29 – 74.

Burke, K., Perdew, J.P., Wang, Y., 1998. Derivation of a Generalized Gradient Approximation: The PW91 Density Functional. In: Dobson, J.F., Vignale, G., Das, M.P. (Eds.), Electronic Density Functional Theory - Recent Progress and New Directions. Springer-Verlag US, pp. 81 – 111.

Cameron, E.N., 1978. The Lower Zone of the Eastern Bushveld Complex in the Olifants River Trough. J. Petrol. 19, 437–462.

Campbell, C.T., Daube, K.A., 1987. A surface science investigation of the water-gas shift reaction on Cu(111). J. Catal. 104, 109–119.

Campbell, J.S., Craven, P., Young, P.W., 1970. Removal of carbon monoxide. In: Catalyst Handbook. Wolfe Scientific Books, pp. 97–126.

Cemič, L., Kleppa, O.J., 1987. High temperature calorimetry of sulfide systems. Phys. Chem. Miner. 14, 52 – 57.

Ceperley, D.M., Alder, B.J., 1980. Ground State of the Electron Gas by a Stochastic Method. Phys. Rev. Lett. 45, 566–569.

Chadi, D.J., Cohen, M.L., 1973. Special Points in the Brillouin Zone. Phys. Rev. B 8, 5747 – 5753.

Chainani, A., Yokoya, T., Morimoto, T., Takahashi, T., Todo, S., 1995. High-resolution photoemission spectroscopy of the Verwey transition in Fe_3O_4. Phys. Rev. B 51, 17976–17979.

Chambers, S.A., Thevuthasan, S., Joyce, S.A., 2000. Surface structure of MBE-grown Fe_3O_4 (001) by X-ray photoelectron diffraction and scanning tunneling microscopy. Surf. Sci. 450, L273–L279.

Chandra, A.P., Gerson, A.R., 2010. The mechanisms of pyrite oxidation and leaching: A fundamental perspective. Surf. Sci. Rep. 65, 293–315.

Chang, L., Rainford, B.D., Stewart, J.R., Ritter, C., Roberts, A.P., Tang, Y., Chen, Q., 2009. Magnetic structure of greigite (Fe_3S_4) probed by neutron powder diffraction and polarized neutron diffraction. J. Geophys. Res. 114, B07101.

Chang, L., Roberts, A.P., Tang, Y., Rainford, B.D., Muxworthy, A.R., Chen, Q., 2008. Fundamental magnetic parameters from pure synthetic greigite (Fe_3S_4). J. Geophys. Res. 113, B06104.

Charnock, J., Garner, C.D., Pattrick, R.A.D., Vaughan, D.J., 1990. An EXAFS Study of Thiospinel Minerals. Am. Mineral. 75, 247 – 255.

Chase, M.W.J., 1998. NIST JANAF Thermochemical Tables. American Chemical Society and American Institute of Physics for the National Institute of Standards and Technology, Washington DC.

Chen, S.-S., Updated by Staff, 2006. Styrene. In: Kirk-Othmer Encyclopedia of Chemical Technology. John Wiley & Sons, Inc.

Chikamii, J., Miyamotoi, M., Hiroshi, T., 1999. The variation of Zn content in spinel group minerals and daubreelites of primitive achondrites. Antarct. Meteor. Res. 12, 139–150.

Ciofini, I., Illas, F., Adamo, C., 2004. Performance of the tau-dependent functionals in predicting the magnetic coupling of ionic antiferromagnetic insulators. J. Chem. Phys. 120, 3811–3816.

Coey, J.M.D., Chien, C.L., 2011. Half-Metallic Ferromagnetic Oxides. MRS Bull. 28, 720–724.

Coey, J.M.D., Sanvito, S., 2004. Magnetic semiconductors and half-metals. J. Phys. D. Appl. Phys. 37, 988–993.

Coey, J.M.D., Spender, M.R., Morrish, A.H., 1970. The magnetic structure of the spinel Fe_3S_4. Solid State Commun. 8, 1605 – 1608.

Coey, J.M.D., Venkatesan, M., 2002. Half-metallic ferromagnetism: Example of CrO_2 (invited). J. Appl. Phys. 91, 8345 – 8350.

Coey, J.M.D., Venkatesan, M., Bari, M.A., 2001. Half-Metallic Ferromagnets. In: Berthier, C., Levy, L.P., Martinez, G. (Eds.), High Magnetic Fields. Lecture Notes in Physics, Vol. 595. Springer Berlin Heidelberg, pp. 377–396.

Condon, N.G., Leibsle, F.M., Parker, T., Lennie, A.R., Vaughan, D.J., Thornton, G., 1997. Biphase ordering on Fe_3O_4(111). Phys. Rev. B 55, 15885–15894.

Cooper, T.G., de Leeuw, N.H., 2006. A computer modelling study of the incorporation of K^+, Ca^{2+} and Mg^{2+} impurities in two Na_2SO_4 polymorphs: Introducing a Na_2SO_4 potential model. J. Cryst. Growth 294, 137–149.

Corà, F., 2005. The performance of hybrid density functionals in solid state chemistry: the case of $BaTiO_3$. Mol. Phys. 103, 2483–2496.

Cormack, A.N., Lewis, G.V., Parker, S.C., Catlow, C.R.A., 1988. On the cation distribution of spinels. J. Phys. Chem. Solids 49, 53 – 57.

Cornell, R.M., Schwertmann, U., 2003. The Iron Oxides, Second Edi. ed. Wiley-VCH Verlag GmbH & Co. KGaA, Weinheim, FRG.

Costa, R.C.C., Moura, F.C.C., Ardisson, J.D., Fabris, J.D., Lago, R.M., 2008. Highly active heterogeneous Fenton-like systems based on Fe^0/Fe_3O_4 composites prepared by controlled reduction of iron oxides. 83, 131–139.

Cottenier, S., Vanhoof, V., Torumba, D., Bellini, V., Çakmak, M., Rots, M., 2005. Ab Initio Calculation of Hyperfine Interaction Parameters: Recent Evolutions, Recent Examples. Hyperfine Interact. 158, 9–18.

Couling, S.B., Mann, S., 1985. The influence of inorganic phosphate on the crystallization of magnetite (Fe_3O_4) from aqueous solution. J. Chem. Soc. Chem. Commun. 1, 1713.

Craig, J.R., 1971. Violarite Stability Relations. Am. Mineral. 56, 1303–1311.

Cui, Z., Jiang, L., Song, W., Guo, Y., 2009. High-Yield Gas−Liquid Interfacial Synthesis of Highly Dispersed Fe_3O_4 Nanocrystals and Their Application in Lithium-Ion Batteries. Chem. Mater. 21, 1162–1166.

David, I., Welch, A.J.E., 1956. The oxidation of magnetite and related spinels. Constitution of gamma ferric oxide. Trans. Faraday Soc. 52, 1642.

De Groot, R.A., Mueller, F.M., van Engen, P.G., Buschow, K.H.J., 1983. New Class of Materials: Half-Metallic Ferromagnets. Phys. Rev. Lett. 50, 2024 – 2027.

De La Pierre, M., Orlando, R., Maschio, L., Doll, K., Ugliengo, P., Dovesi, R., 2011. Performance of six functionals (LDA, PBE, PBESOL, B3LYP, PBE0, and WC1LYP) in the simulation of vibrational and dielectric properties of crystalline compounds. The case of forsterite Mg_2SiO_4. J. Comput. Chem. 32, 1775 – 1784.

De Leeuw, N.H., Cooper, T.G., 2007. Surface simulation studies of the hydration of white rust $Fe(OH)_2$, goethite α-FeO(OH) and hematite α-Fe_2O_3. Geochim. Cosmochim. Acta 71, 1655–1673.

De Proft, F., Van Alsenoy, C., Peeters, A., Langenaeker, W., Geerlings, P., 2002. Atomic charges, dipole moments, and Fukui functions using the Hirshfeld partitioning of the electron density. J. Comput. Chem. 23, 1198–1209.

Dekkers, M.J., Passier, H.F., Schoonen, M.A.A., 2000. Magnetic properties of hydrothermally synthesized greigite (Fe_3S_4)-II. High- and low-temperature characteristics. Geophys. J. Int. 141, 809 – 819.

Dekkers, M.J., Schoonen, M.A.A., 1994. An electrokinetic study of synthetic greigite and pyrrhotite. Geochim. Cosmochim. Acta 58, 4147–4153.

Dekkers, M.J., Schoonen, M.A.A., 1996. Magnetic properties of hydrothermally synthesized greigite (Fe_3S_4)-I. Rock magnetic parameters at room temperature. Geophys. J. Int. 126, 360–368.

Devey, A.J., Grau-Crespo, R., de Leeuw, N.H., 2008. Combined Density Functional Theory and Interatomic Potential Study of the Bulk and Surface Structures and Properties of the Iron Sulfide Mackinawite (FeS). J. Phys. Chem. C 112, 10960–10967.

Devey, A.J., Grau-Crespo, R., de Leeuw, N.H., 2009. Electronic and magnetic structure of Fe_3S_4: GGA+U investigation. Phys. Rev. B 79, 195126.

Devouard, B., Pósfai, M., Hua, X., Bazylinski, D.A., Frankel, R.B., Buseck, P.R., 1998. Magnetite from Magnetotactic Bacteria: Size Distributions and Twinning. Am. Mineral. 83, 1387–1398.

Domka, F., Basinska, A., Fiedorow, R., 1983. Porous Structure of Fe_2O_3-Cr_2O_3 Catalysts Prepared from Iron Oxide-Hydroxide Systems. Surf. Technol. 18, 275–282.

Dos Santos Coelho, F., Ardisson, J.D., Moura, F.C.C., Lago, R.M., Murad, E., Fabris, J.D., 2008. Potential Application of Highly Reactive Fe(0)/Fe_3O_4 Composites for the Reduction of Cr(VI) Environmental Contaminants. Chemosphere 71, 90–6.

Dry, M.E., Ferreira, L.C., 1967. The Distribution of Promoters in Magnetite Catalysts. J. Catal. 7, 352–358.

Dry, M.E., Oosthuizen, G.J., 1968. The correlation between catalyst surface basicity and hydrocarbon selectivity in the Fischer-Tropsch synthesis. J. Catal. 11, 18–24.

Du, Z., de Leeuw, N.H., 2006. Molecular dynamics simulations of hydration, dissolution and nucleation processes at the α-quartz (0001) surface in liquid water. Dalton Trans. 2623–34.

Dudarev, S.L., Botton, G.A., Savrasov, S.Y., Humphreys, C.J., Sutton, A.P., 1998. Electron-energy-loss spectra and the structural stability of nickel oxide: An LSDA+U study. Phys. Rev. B 57, 1505 – 1509.

Dunitz, J.D., Orgel, L.E., 1957. Electronic properties of transition-metal oxides-II. J. Phys. Chem. Solids 3, 318 – 323.

Dzade, N.Y., Roldan, A., de Leeuw, N.H., 2013. Adsorption of methylamine on mackinawite (FES) surfaces: A density functional theory study. J. Chem. Phys. 139, 124708.

Dzade, N.Y., Roldan, A., de Leeuw, N.H., 2014. The surface chemistry of NO_x on mackinawite (FeS) surfaces: a DFT-D2 study. Phys. Chem. Chem. Phys. 16, 15444 – 15456.

Eerenstein, W., Palstra, T.T.M., Saxena, S.S., Hibma, T., 2002. Spin-Polarized Transport across Sharp Antiferromagnetic Boundaries. Phys. Rev. Lett. 88, 247204.

El Goresy, A., 1967. Quantitative electron microprobe analyses of coexisting sphalerite, daubreelite and troilite in the Odessa iron meteorite and their genetic implications. Geochim. Cosmochim. Acta 31, 1667–1676.

Emmett, P.H., Brunauer, S., 1934. The Adsorption of Nitrogen by Iron Synthetic Ammonia Catalysts. J. Am. Chem. Soc. 56, 35–41.

Ertl, G., 1983. Kinetics of Chemical Processes on Well-defined Surfaces. In: Anderson, D.J.R., Boudart, P.M. (Eds.), Catalysis — Science and Technology — Volume 4. Springer-Verlag, Berlin Heidelberg, pp. 209–282.

Faivre, D., Menguy, N., Guyot, F., Lopez, O., Zuddas, P., 2005. Morphology of nanomagnetite crystals: Implications for formation conditions. Am. Mineral. 90, 1793–1800.

Faivre, D., Schüler, D., 2008. Magnetotactic bacteria and magnetosomes. Chem. Rev. 108, 4875–4898.

Fassbinder, J.W., Stanjek, H., Vali, H., 1990. Occurrence of magnetic bacteria in soil. Nature 343, 161–3.

Fassbinder, J.W.E., Stanjek, H., 1994. Magnetic properties of biogenic soil greigite (Fe_3S_4). Geophys. Res. Lett. 21, 2349–2352.

Feitknecht, W., 1959. Uber die oxydation von festen hydroxyverbindungen des eisens in wassrigen losungen. Zeitschrift für Elektrochemie 63, 34–43.

Felser, C., Fecher, G.H., Balke, B., 2007. Spintronics: a challenge for materials science and solid-state chemistry. Angew. Chemie Int. Ed. 46, 668 – 699.

Ferreira, T.A.S., Waerenborgh, J.C., Mendonça, M.H.R.M., Nunes, M.R., Costa, F.M., 2003. Structural and morphological characterization of $FeCo_2O_4$ and $CoFe_2O_4$ spinels prepared by a coprecipitation method. Solid State Sci. 5, 383 – 392.

Ferry, J.G., 1995. CO dehydrogenase. Annu. Rev. Microbiol. 49, 305–33.

Fleet, M.E., 1982. The structure of magnetite: defect structure II. Acta Crystallogr. Sect. B Struct. Crystallogr. Cryst. Chem. 38, 1718–1723.

Fletcher, R., Reeves, C.M., 1964. Function minimization by conjugate gradients. Comput. J. 7, 149–154.

Fonin, M., Pentcheva, R., Dedkov, Y.S., Sperlich, M., Vyalikh, D. V., Scheffler, M., Rüdiger, U., Güntherodt, G., 2005. Surface electronic structure of the Fe_3O_4(100): Evidence of a half-metal to metal transition. Phys. Rev. B 72, 104436.

Fowler, T.A., Holmes, P.R., Crundwell, F.K., 1999. Mechanism of pyrite dissolution in the presence of Thiobacillus ferrooxidans. Appl. Environ. Microbiol. 65, 2987–93.

Fowler, T.A., Holmes, P.R., Crundwell, F.K., 2001. On the kinetics and mechanism of the dissolution of pyrite in the presence of Thiobacillus ferrooxidans. Hydrometallurgy 59, 257–270.

Francis, G.P., Payne, M.C., 1990. Finite basis set corrections to total energy pseudopotential calculations. J. Phys. Condens. Matter 2, 4395–4404.

Frank, U., Nowaczyk, N.R., Negendank, J.F.W., 2007. Palaeomagnetism of greigite bearing sediments from the Dead Sea, Israel. Geophys. J. Int. 168, 904–920.

Frankel, R.B., 1991. Iron biominerals: an overview. In: Frankel, R.B., Blakemore, R.P. (Eds.), Iron Biominerals. Springer US, New York, pp. 1 – 6.

Fritsch, D., Ederer, C., 2010. Epitaxial strain effects in the spinel ferrites $CoFe_2O_4$ and $NiFe_2O_4$ from first principles. Phys. Rev. B 82, 104117.

Fritsch, D., Ederer, C., 2011a. Strain effects in spinel ferrite thin films from first principles calculations. J. Phys. Conf. Ser. 292, 012014.

Fritsch, D., Ederer, C., 2011b. Effect of epitaxial strain on the cation distribution in spinel ferrites $CoFe_2O_4$ and $NiFe_2O_4$: A density functional theory study. Appl. Phys. Lett. 99, 081916.

Frost, B.R., 1991. Stability of oxide minerals in metamorphic rocks. In: Lindsley, D.H. (Ed.), Reviews in Mineralogy and Geochemistry - Volume 25 - Oxide Minerals: Petrologic and Magnetic Significance. Mineralogical Society of America, Washington DC, pp. 469 – 488.

Frost, B.R., Lindsley, D.H., 1991. Occurrence of Iron-Titanium Oxides in Igneous Rocks. In: Lindsley, D.H. (Ed.), Reviews in Mineralogy and Geochemistry - Volume 25 - Oxide Minerals: Petrologic and Magnetic Significance. Mineralogical Society of America, Washington DC, pp. 433–468.

Gaines, R. V., Skinner, H.C.W., Foord, E.E., Mason, B., Rosenzweig, A., 1997. Dana's New Mineralogy: The System of Mineralogy of James Dwight and Edward Salisbury. Wiley-Blackwell.

Galanakis, I., Dederichs, P.H., Papanikolaou, N., 2002. Origin and properties of the gap in the half-ferromagnetic Heusler alloys. Phys. Rev. B 66, 134428.

Garbassi, F., Fagherazzi, G., Calcaterra, M., 1972. Structural Study of the Al_2O_3-Promoted Ammonia Synthesis Catalyst I. Unreduced State. J. Catal. 26, 338–343.

Gartman, A., Luther, G.W., 2014. Oxidation of synthesized sub-micron pyrite (FeS_2) in seawater. Geochim. Cosmochim. Acta.

Gibbs, J.W., 1928. Collected Works. Longman, New York.

Giggenbach, W., 1971. Optical spectra of highly alkaline sulfide solutions and the second dissociation constant of hydrogen sulfide. Inorg. Chem. 10, 1333–1338.

Gill, P.E., Murray, W., Wright, M.H., 1981. Practical Optimization. Academic Press, London.

Goffredi, S.K., Waren, A., Orphan, V.J., Van Dover, C.L., Vrijenhoek, R.C., 2004. Novel Forms of Structural Integration between Microbes and a Hydrothermal Vent Gastropod from the Indian Ocean. Appl. Environ. Microbiol. 70, 3082–3090.

Gonzalez, J.C., Gonzalez, M.G., Laborde, M.A., Moreno, N., 1986. Effect of temperature and reduction on the activity of high temperature water gas shift catalysts. Appl. Catal. 20, 3–13.

Gould, J.L., Kirschvink, J.L., Deffeyes, K.S., 1978. Bees have magnetic remanence. Science 201, 1026–8.

Grant, F.S., 1985. Aeromagnetics, geology and ore environments, I. Magnetite in igneous, sedimentary and metamorphic rocks: An overview. Geoexploration 23, 303–333.

Grau-Crespo, R., Catlow, C.R.A., de Leeuw, N.H., 2007. A computer modeling study of redox processes on the $FeSbO_4$ (100) surface. J. Catal. 248, 77–88.

Grau-Crespo, R., Corà, F., Sokol, A.A., de Leeuw, N.H., Catlow, C.R.A., 2006a. Electronic structure and magnetic coupling in $FeSbO_4$: A DFT study using hybrid functionals and GGA+U methods. Phys. Rev. B 73, 035116.

Grau-Crespo, R., Moreira, I. de P.R., Illas, F., de Leeuw, N.H., Catlow, C.R.A., 2006b. The effect of cation coordination on the properties of oxygen vacancies in $FeSbO_4$. J. Mater. Chem. 16, 1943–1949.

Grimme, S., 2006. Semiempirical GGA-type density functional constructed with a long-range dispersion correction. J. Comput. Chem. 27, 1787 – 1799.

Grimme, S., Antony, J., Ehrlich, S., Krieg, H., 2010. A consistent and accurate ab initio parametrization of density functional dispersion correction (DFT-D) for the 94 elements H-Pu. J. Chem. Phys. 132, 154104.

Grimme, S., Ehrlich, S., Goerigk, L., 2011. Effect of the damping function in dispersion corrected density functional theory. J. Comput. Chem. 32, 1456–65.

Hafner, J., 2008. Ab-initio simulations of materials using VASP: Density-functional theory and beyond. J. Comput. Chem. 29, 2044–78.

Haider, S., Grau-Crespo, R., Devey, A.J., de Leeuw, N.H., 2012. Cation distribution and mixing thermodynamics in Fe/Ni thiospinels. Geochim. Cosmochim. Acta 88, 275–282.

Haider, S., Roldan, A., de Leeuw, N.H., 2014. Catalytic Dissociation of Water on the (001), (011), and (111) Surfaces of Violarite, $FeNi_2S_4$: A DFT-D2 Study. J. Phys. Chem. C 118, 1958 – 1967.

Hamann, D., Schlüter, M., Chiang, C., 1979. Norm-Conserving Pseudopotentials. Phys. Rev. Lett. 43, 1494–1497.

Hammarstrom, J.M., Sibrell, P.L., Belkin, H.E., 2003. Characterization of limestone reacted with acid-mine drainage in a pulsed limestone bed treatment system at the Friendship Hill National Historical Site, Pennsylvania, USA. Appl. Geochemistry 18, 1705–1721.

Hammer, B., Jacobsen, K., Nørskov, J., 1993. Role of nonlocal exchange correlation in activated adsorption. Phys. Rev. Lett. 70, 3971–3974.

Harmony, M.D., Laurie, V.W., Kuczkowski, R.L., Schwendeman, R.H., Ramsay, D.A., Lovas, F.J., Lafferty, W.J., Maki, A.G., 1979. Molecular structures of gas-phase polyatomic molecules determined by spectroscopic methods. J. Phys. Chem. Ref. Data 8, 619.

Haynes, W.M. (Ed.), 2012. CRC Handbook of Chemistry and Physics, 93rd ed. Boca Raton, Fla.: CRC; London: Taylor & Francis [distributor].

Hearmon, R.F.S., 1984. The elastic constants of crystals and other anisotropic materials. In: Hellwege, K.H., Hellwege, A.M. (Eds.), Landolt-Börnstein Tables, III/18. Springer-Verlag, Berlin, pp. 1–154.

Henderson, T.M., Paier, J., Scuseria, G.E., 2011. Accurate treatment of solids with the HSE screened hybrid. Phys. Status Solidi B 248, 767 – 774.

Henkelman, G., Arnaldsson, A., Jónsson, H., 2006. A fast and robust algorithm for Bader decomposition of charge density. Comput. Mater. Sci. 36, 354 – 360.

Henkelman, G., Jóhannesson, G., Jónsson, H., 2002. Methods for Finding Saddle Points and Minimum Energy Paths. In: Schwartz, S.D. (Ed.), Theoretical Methods in Condensed Phase Chemistry - Progress in Theoretical Chemistry and Physics - Volume 5. Springer Netherlands Kluwer Academic Publishers, pp. 269–300.

Henkelman, G., Jónsson, H., 1999. A dimer method for finding saddle points on high dimensional potential surfaces using only first derivatives. J. Chem. Phys. 111, 7010–7022.

Henkelman, G., Jónsson, H., 2000. Improved tangent estimate in the nudged elastic band method for finding minimum energy paths and saddle points. J. Chem. Phys. 113, 9978.

Henkelman, G., Uberuaga, B.P., Jónsson, H., 2000. A climbing image nudged elastic band method for finding saddle points and minimum energy paths. J. Chem. Phys. 113, 9901.

Henrici-Olive, G., Olive, S., 1976. The Fischer-Tropsch Synthesis: Molecular Weight Distribution of Primary Products and Reaction Mechanism. Angew. Chemie Int. Ed. English 15, 136–141.

Heyd, J., Peralta, J.E., Scuseria, G.E., Martin, R.L., 2005. Energy band gaps and lattice parameters evaluated with the Heyd-Scuseria-Ernzerhof screened hybrid functional. J. Chem. Phys. 123, 174101.

Heyd, J., Scuseria, G.E., 2004a. Efficient hybrid density functional calculations in solids: Assessment of the Heyd-Scuseria-Ernzerhof screened Coulomb hybrid functional. J. Chem. Phys. 121, 1187–1192.

Heyd, J., Scuseria, G.E., 2004b. Assessment and validation of a screened Coulomb hybrid density functional. J. Chem. Phys. 120, 7274–7280.

Heyd, J., Scuseria, G.E., Ernzerhof, M., 2003. Hybrid functionals based on a screened Coulomb potential. J. Chem. Phys. 118, 8207 – 8215.

Heyd, J., Scuseria, G.E., Ernzerhof, M., 2006. Erratum: “Hybrid functionals based on a screened Coulomb potential” [J. Chem. Phys. 118, 8207 (2003)]. J. Chem. Phys. 124, 219906.

Heyden, A., Bell, A.T., Keil, F.J., 2005. Efficient methods for finding transition states in chemical reactions: Comparison of improved dimer method and partitioned rational function optimization method. J. Chem. Phys. 123, 224101.

Heywood, B.R., Bazylinski, D.A., Garratt-Reed, A., Mann, S., Frankel, R.B., 1990. Controlled biosynthesis of greigite (Fe_3S_4) in magnetotactic bacteria. Naturwissenschaften 77, 536–538.

Hill, R.J., Craig, J.R., Gibbs, G. V., 1979. Systematics of the spinel structure type. Phys. Chem. Miner. 4, 317 – 339.

Hofmann, U., 1962. Die chemischen Grundlagen der griechischen Vasenmalerei. Angew. Chemie 74, 397–406.

Hohenberg, P., Kohn, W., 1964. Inhomogeneous Electron Gas. Phys. Rev. 136, B864–B871.

Horiuchi, S., Wada, H., Moori, T., 1974. Morphology and imperfection of hydrothermally synthesized greigite (Fe_3S_4). J. Cryst. Growth 24-25, 624–626.

Hubbard, J., 1963. Electron Correlations in Narrow Energy Bands. Proc. R. Soc. A Math. Phys. Eng. Sci. 276, 238–257.

Huber, C., Wächtershäuser, G., 1997. Activated Acetic Acid by Carbon Fixation on (Fe,Ni)S Under Primordial Conditions. Science 276, 245–247.

Huberty, J.M., Konishi, H., Heck, P.R., Fournelle, J.H., Valley, J.W., Xu, H., 2012. Silician magnetite from the Dales Gorge Member of the Brockman Iron Formation, Hamersley Group, Western Australia. Am. Mineral. 97, 26–37.

Huff, G.A., Satterfield, C.N., 1984. Intrinsic kinetics of the Fischer-Tropsch synthesis on a reduced fused-magnetite catalyst. Ind. Eng. Chem. Process Des. Dev. 23, 696–705.

Hunger, S., Benning, L.G., 2007. Greigite: a true intermediate on the polysulfide pathway to pyrite. Geochem. Trans. 8, 1.

Illas, F., Martin, R.L., 1998. Magnetic coupling in ionic solids studied by density functional theory. J. Chem. Phys. 108, 2519–2527.

Irrera, S., Roldan, A., Portalone, G., De Leeuw, N.H., 2013. The Role of Hydrogen Bonding and Proton Transfer in the Formation of Uracil Networks on the Gold (100) Surface: A Density Functional Theory Approach. J. Phys. Chem. C 117, 3949 – 3957.

Isida, S., Suzuki, M., Todo, S., Mori, N., Siratori, K., 1996. Pressure effect on the elastic constants of magnetite. Phys. B Condens. Matter 219-220, 638–640.

Ivanov, S., Hirata, S., Bartlett, R., 1999. Exact Exchange Treatment for Molecules in Finite-Basis-Set Kohn-Sham Theory. Phys. Rev. Lett. 83, 5455–5458.

James, D.H., Castor, W.M., 2012. Styrene. In: Ullmann's Encyclopedia of Industrial Chemistry. Wiley-VCH Verlag GmbH & Co. KGaA, Weinheim, pp. 529–544.

Jansen, R., Brabers, V.A.M., van Kempen, H., 1995. One-dimensional reconstruction observed on Fe_3O_4(110) by scanning tunneling microscopy. Surf. Sci. 328, 237–247.

Jansen, R., van Kempen, H., Wolf, R.M., 1996. Scanning tunneling microscopy and spectroscopy on thin Fe_3O_4 (110) films on MgO. J. Vac. Sci. Technol. B 14, 1173.

Jelinowska, A., Tucholka, P., Gasse, F., Fontes, J.C., 1995. Mineral magnetic record of environment in Late Pleistocene and Holocene sediments, Lake Manas, Xinjiang, China. Geophys. Res. Lett. 22, 953–956.

Jelinowska, A., Tucholka, P., Guichard, F., Lefe, I., Gasse, F., Tribovillard, N., Desprairies, A., Chalie, F., 1998. Mineral magnetic study of Late Quaternary South Caspian Sea sediments: palaeoenvironmental implications. Geophys. J. Int. 133, 499–509.

Jin, Y., Datye, A.K., 2000. Phase Transformations in Iron Fischer–Tropsch Catalysts during Temperature-Programmed Reduction. J. Catal. 196, 8–17.

Joeckel, R.M., Ang Clement, B.J., VanFleet Bates, L.R., 2005. Sulfate-mineral crusts from pyrite weathering and acid rock drainage in the Dakota Formation and Graneros Shale, Jefferson County, Nebraska. Chem. Geol. 215, 433–452.

Johnson, D.B., 2003. Chemical and Microbiological Characteristics of Mineral Spoils and Drainage Waters at Abandoned Coal and Metal Mines. ChemInform 34, 47–66.

Johnson, D.B., Hallberg, K.B., 2005. Acid mine drainage remediation options: a review. Sci. Total Environ. 338, 3–14.

Jónsson, H., Mills, G., Jacobsen, K.W., 1998. Nudged elastic band method for finding minimum energy paths of transitions. In: Berne, B.J., Ciccotti, G., Coker, D.F. (Eds.), Classical and Quantum Dynamics in Condensed Phase Simulations - Proceedings of the International School of Physics. World Scientific Publishing Co. Pte. Ltd., Singapore, New Jersey, London, Hong Kong, pp. 385–404.

Kąkol, Z., Honig, J.M., 1989. Influence of deviations from ideal stoichiometry on the anisotropy parameters of magnetite $Fe_{3(1-\delta)}O_4$. Phys. Rev. B 40, 9090–9097.

Kaneko, T., Derbyshire, F., Makino, E., Gray, D., Tamura, M., Li, K., 2012. Coal Liquefaction. In: Ullmann's Encyclopedia of Industrial Chemistry. Wiley-VCH Verlag GmbH & Co. KGaA, Weinheim, pp. 1–83.

Kaplan, T.A., Dwight, K., Lyons, D., Menyuk, N., 1961. Classical Theory of the Ground Spin State in Spinels. J. Appl. Phys. 32, S13.

Kawano, S., Achiwa, N., Yamamoto, N., Higashi, S., 1976. Metal-Ion Distribution and Magnetic Structure of Fe-Substituted Cobaltite Spinel: $FeCo_2O_4$. Mater. Res. Bull. 11, 911–916.

Kida, T., Honda, S., Itoh, H., Inoue, J., Yanagihara, H., Kita, E., Mibu, K., 2011. Electronic and Magnetic Structure at the Fe/Fe_3O_4 Interface. Phys. Rev. B 84, 104407.

Kiejna, A., Ossowski, T., Pabisiak, T., 2012. Surface properties of the clean and Au/Pd covered Fe_3O_4(111): DFT and DFT+U study. Phys. Rev. B 85, 125414.

Kim, S.J., 2004. Mössbauer studies of dynamic Jahn-Teller relaxation on the Cu-substituted sulfur spinel. J. Appl. Phys. 95, 6837.

Kirschvink, J.L., Jones, D.S., MacFadden, B.J. (Eds.), 1985. Magnetite Biomineralization and Magnetoreception in Organisms - A New Biomagnetism - Topics in Geobiology - Volume 5. Plenum Press, New York and London.

Kirschvink, J.L., Lowenstam, H.A., 1979. Mineralization and magnetization of chiton teeth: paleomagnetic, sedimentologic, and biologic implications of organic magnetite. Earth Planet. Sci. Lett. 44, 193–204.

Klemme, S., O'Neill, H.S.C., Schnelle, W., Gmelin, E., 2000. The heat capacity of $MgCr_2O_4$, $FeCr_2O_4$, and Cr_2O_3 at low temperatures and derived thermodynamic properties. Am. Mineral. 85, 1686–1693.

Kocsis, V., Bordács, S., Varjas, D., Penc, K., Abouelsayed, A., Kuntscher, C.A., Ohgushi, K., Tokura, Y., Kézsmárki, I., 2013. Magnetoelasticity in ACr_2O_4 spinel oxides (A= Mn, Fe, Co, Ni, and Cu). Phys. Rev. B 87, 064416.

Kohn, W., Sham, L.J., 1965. Self-Consistent Equations Including Exchange and Correlation Effects. Phys. Rev. 140, A1133–A1138.

Kominami, H., Onoue, S., Matsuo, K., Kera, Y., 1999. Synthesis of Microcrystalline Hematite and Magnetite in Organic Solvents and Effect of a Small Amount of Water in the Solvents. J. Am. Ceram. Soc. 82, 1937–1940.

Konhauser, K.O., 1998. Diversity of bacterial iron mineralization. Earth-Science Rev. 43, 91–121.

Koryabkina, N.A., Phatak, A.A., Ruettinger, W.F., Farrauto, R.J., Ribeiro, F.H., 2003. Determination of kinetic parameters for the water–gas shift reaction on copper catalysts under realistic conditions for fuel cell applications. J. Catal. 217, 233–239.

Kostov, I., 1968. Mineralogy. Oliver Boyd, Edinburgh, London.

Kresse, G., Furthmüller, J., 1996a. Efficiency of ab-initio total energy calculations for metals and semiconductors using a plane-wave basis set. Comput. Mater. Sci. 6, 15 – 50.

Kresse, G., Furthmüller, J., 1996b. Efficient iterative schemes for ab initio total-energy calculations using a plane-wave basis set. Phys. Rev. B 54, 11169 – 11186.

Kresse, G., Hafner, J., 1993. Ab initio molecular dynamics for liquid metals. Phys. Rev. B 47, 558 – 561.

Kresse, G., Hafner, J., 1994. Ab initio molecular-dynamics simulation of the liquid-metal–amorphous-semiconductor transition in germanium. Phys. Rev. B 49, 14251 – 14269.

Kresse, G., Joubert, D., 1999. From ultrasoft pseudopotentials to the projector augmented-wave method. Phys. Rev. B 59, 1758 – 1775.

Kriessman, C.J., Harrison, S.E., 1956. Cation Distributions in Ferrospinels. Magnesium-Manganese Ferrites. Phys. Rev. 103, 857 – 860.

Krukau, A. V., Vydrov, O.A., Izmaylov, A.F., Scuseria, G.E., 2006. Influence of the exchange screening parameter on the performance of screened hybrid functionals. J. Chem. Phys. 125, 224106.

Krupicka, S., Novak, P., 1982. Oxide Spinels. In: Wohlfarth, E.P. (Ed.), Ferromagnetic Materials. A Handbook on the Properties of Magnetically Ordered Substances. Volume 3. North-Holland Physics Publishing, Amsterdam, pp. 189 – 304.

Kulkarni, J.A., Darshane, V.S., 1985. Effect of High Temperatures on Cation Distribution: $NiMn_2O_4$-$FeMn_2O_4$ System. Thermochim. Acta 93, 473 – 476.

Kummer, J.T., Emmett, P.H., 1953. Fischer—Tropsch Synthesis Mechanism Studies. The Addition of Radioactive Alcohols to the Synthesis Gas. J. Am. Chem. Soc. 75, 5177–5183.

Le Trong, H., Barnabé, A., Presmanes, L., Tailhades, P., 2008. Phase Decomposition Study in $Co_xFe_{3-x}O_4$ Iron Cobaltites: Synthesis and Structural Characterization of the Spinodal Transformation. Solid State Sci. 10, 550 – 556.

Leblanc, M., 1980. Chromite growth, dissolution and deformation from a morphological view point: SEM investigations. Miner. Depos. 15, 201–210.

Lee, Y. Il, 1999. Geotectonic significance of detrital chromian spinel: a review. Geosci. J. 3, 23–29.

Lennie, A.R., Condon, N.G., Leibsle, F.M., Murray, P.W., Thornton, G., Vaughan, D.J., 1996. Structures of Fe_3O_4 (111) surfaces observed by scanning tunneling microscopy. Phys. Rev. B 53, 10244–10253.

Lennie, A.R., Redfern, S.A.T., Champness, P.E., Stoddart, C.P., Schofield, P.F., Vaughan, D.J., 1997. Transformation of mackinawite to greigite : An in situ X-ray powder diffraction and transmission electron microscope study. Am. Mineral. 82, 302–309.

Leung, T., Chan, C., Harmon, B., 1991. Ground-state properties of Fe, Co, Ni, and their monoxides: Results of the generalized gradient approximation. Phys. Rev. B 44, 2923–2927.

Li, S., Meitzner, G.D., Iglesia, E., 2001. Structure and Site Evolution of Iron Oxide Catalyst Precursors during the Fischer−Tropsch Synthesis. J. Phys. Chem. B 105, 5743–5750.

Lin, B.-L., Shen, X.-D., Cui, S., 2007. Application of nanosized Fe_3O_4 in anticancer drug carriers with target-orientation and sustained-release properties. Biomed. Mater. 2, 132–4.

Lins, U., Keim, C.N., Evans, F.F., Farina, M., Buseck, P.R., 2007. Magnetite (Fe_3O_4) and Greigite (Fe_3S_4) Crystals in Multicellular Magnetotactic Prokaryotes. Geomicrobiol. J. 24, 43–50.

Liu, P., Rodriguez, J.A., 2007. Water-gas-shift reaction on metal nanoparticles and surfaces. J. Chem. Phys. 126, 164705.

Liu, S.R., Ji, D.H., Xu, J., Li, Z.Z., Tang, G.D., Bian, R.R., Qi, W.H., Shang, Z.F., Zhang, X.Y., 2013. Estimation of cation distribution in spinel ferrites $Co_{1+x}Fe_{2-x}O_4$ ($0.0<x<2.0$) using the magnetic moments measured at 10 K. J. Alloys Compd. 581, 616 – 624.

Logan, S.R., Kemball, C., 1960. The catalytic decomposition of ammonia on evaporated metal films. Trans. Faraday Soc. 56, 144.

Loschen, C., Carrasco, J., Neyman, K.M., Illas, F., 2007. First-principles LDA+U and GGA+U study of cerium oxides: Dependence on the effective U parameter. Phys. Rev. B 75, 035115.

Lotgering, F.K., 1956. Oxygen and sulphur spinels containing cobalt (MCo_2O_4) and (MCo_2S_4). Phil. Res. Rep. 11, 337 – 350.

Lowenstam, H., 1981. Minerals formed by organisms. Science 211, 1126–1131.

Lowenstam, H.A., 1962. Magnetite in Denticle Capping in Recent Chitons (Polyplacophora). Geol. Soc. Am. Bull. 73, 435.

Lowson, R.T., 1982. Aqueous oxidation of pyrite by molecular oxygen. Chem. Rev. 82, 461–497.

Maher, B.A., Taylor, R.M., 1988. Formation of ultrafine-grained magnetite in soils. Nature 336, 368–370.

Makov, G., Payne, M.C., 1995. Periodic boundary conditions in ab initio calculations. Phys. Rev. B 51, 4014–4022.

Mann, S., Frankel, R.B., 1989. Magnetite biomineralization in unicellular microorganisms. In: Mann, S., Webb, J., Williams, R.J.P. (Eds.), Biomineralization: Chemical and Biochemical Perspectives. VCH, Weinheim, pp. 389–426.

Mann, S., Sparks, N.H.C., Couling, S.B., Larcombe, M.C., Frankel, R.B., 1989. Crystallochemical characterization of magnetic spinels prepared from aqueous solution. J. Chem. Soc. Faraday Trans. 1 Phys. Chem. Condens. Phases 85, 3033.

Mann, S., Sparks, N.H.C., Frankel, R.B., Bazylinski, D.A., Jannasch, H.W., 1990. Biomineralization of ferrimagnetic greigite (Fe_3S_4) and iron pyrite (FeS_2) in a magnetotactic bacterium. Nature 343, 258–261.

Manoharan, S.S., Patil, K.C., 1992. Combustion Synthesis of Metal Chromite Powders. J. Am. Ceram. Soc. 75, 1012–1015.

Mao, X., Lee, J., 2014. Facile Synthesis of Phase-Pure $FeCr_2Se_4$ and $FeCr_2S_4$ Nanocrystals via a Wet Chemistry Method. J. Mater. Chem. C 2, 3744.

Maris, G., Jdira, L., Hermsen, J.G.H., Murphy, S., Manai, G., Shvets, I.V., Speller, S., 2006a. Nano-Magnetic Probing on Magnetite. IEEE Trans. Magn. 42, 2927–2929.

Maris, G., Jdira, L., Hermsen, J.G.H., Murphy, S., Manai, G., Shvets, I. V., Speller, S., 2006b. Towards Spin-Polarized Scanning Tunneling Microscopy on Magnetite (110). Jpn. J. Appl. Phys. 45, 2225–2229.

Maris, G., Shklyarevskii, O., Jdira, L., Hermsen, J.G.H., Speller, S., 2006. One-dimensional structural and electronic properties of magnetite Fe_3O_4(110). Surf. Sci. 600, 5084–5091.

Martin, G.J., Cutting, R.S., Vaughan, D.J., Warren, M.C., 2009. Bulk and key surface structures of hematite, magnetite, and goethite: A density functional theory study. Am. Mineral. 94, 1341–1350.

Matlock, M.M., Howerton, B.S., Atwood, D.A., 2002. Chemical precipitation of heavy metals from acid mine drainage. Water Res. 36, 4757–4764.

McClure, D.S., 1957. The distribution of transition metal cations in spinels. J. Phys. Chem. Solids 3, 311 – 317.

McKay, D.S., Gibson Jr., E.K., Thomas-Keprta, K.L., Vali, H., Romanek, C.S., Clemett, S.J., Chillier, X.D.F., Maechling, C.R., Zare, R.N., 1996. Search for Past Life on Mars: Possible Relic Biogenic Activity in Martian Meteorite ALH84001. Science 273, 924–930.

McKibben, M.A., Barnes, H.L., 1986. Oxidation of pyrite in low temperature acidic solutions: Rate laws and surface textures. Geochim. Cosmochim. Acta 50, 1509–1520.

Mellan, T.A., Grau-Crespo, R., 2012. Density functional theory study of rutile VO_2 surfaces. J. Chem. Phys. 137, 154706.

Middleton, A.P., 1987. Technological Investigation of the Coatings on Some "Haematite-Coated" Pottery from Southern England. Archaeometry 29, 250–261.

Mijiritskii, A.V., Boerma, D.O., 2001. The (001) surface and morphology of thin Fe_3O_4 layers grown by O_2-assisted molecular beam epitaxy. Surf. Sci. 486, 73–81.

Mills, G., Jónsson, H., Schenter, G.K., 1995. Reversible work transition state theory: application to dissociative adsorption of hydrogen. Surf. Sci. 324, 305–337.

Monkhorst, H.J., Pack, J.D., 1976. Special points for Brillouin-zone integrations. Phys. Rev. B 13, 5188 – 5192.

Montoro, V., 1938. Miscibilita fra gli ossidi salini di ferro e di manganese. Gazz. Chim. Ital. 68, 728 – 733.

Morad, S., Aldahan, A.A., 1986. Alteration of detrital Fe-Ti oxides in sedimentary rocks. Geol. Soc. Am. Bull. 97, 567.

Moran, T., Lüthi, B., 1969. Elastic and Magnetoelastic Effects in Magnetite. Phys. Rev. 187, 710–714.

Moreira, I. de P.R., Illas, F., Martin, R.L., 2002. Effect of Fock exchange on the electronic structure and magnetic coupling in NiO. Phys. Rev. B 65, 155102.

Morse, J., Millero, F., Cornwell, J., Rickard, D., 1987. The chemistry of the hydrogen sulfide and iron sulfide systems in natural waters. Earth-Science Rev. 24, 1–42.

Moses, C.O., Kirk Nordstrom, D., Herman, J.S., Mills, A.L., 1987. Aqueous pyrite oxidation by dissolved oxygen and by ferric iron. Geochim. Cosmochim. Acta 51, 1561–1571.

Moura, F., Oliveira, G., Araujo, M., Ardisson, J., Macedo, W., Lago, R., 2006. Highly reactive species formed by interface reaction between Fe^0–iron oxides particles: An efficient electron transfer system for environmental applications. Appl. Catal. A Gen. 307, 195–204.

Mulakaluri, N., Pentcheva, R., Wieland, M., Moritz, W., Scheffler, M., 2009. Partial Dissociation of Water on Fe_3O_4(001): Adsorbate Induced Charge and Orbital Order. Phys. Rev. Lett. 103, 1–4.

Muñoz, D., Harrison, N.M., Illas, F., 2004. Electronic and magnetic structure of $LaMnO_3$ from hybrid periodic density-functional theory. Phys. Rev. B 69, 085115.

Muraliganth, T., Vadivel Murugan, A., Manthiram, A., 2009. Facile synthesis of carbon-decorated single-crystalline Fe3O4 nanowires and their application as high performance anode in lithium ion batteries. Chem. Commun. (Camb). 7360–2.

Murray, P.J., Linnett, J.W., 1976. Cation distribution in the spinels CoxFe3−xO4. J. Phys. Chem. Solids 37, 1041–1042.

Muthuselvam, I.P., Bhowmik, R.N., 2009. Structural phase stability and magnetism in Co_2FeO_4 spinel oxide. Solid State Sci. 11, 719 – 725.

Nakamura, J., Campbell, J.M., Campbell, C.T., 1990. Kinetics and mechanism of the water-gas shift reaction catalysed by the clean and Cs-promoted Cu(110) surface: a comparison with Cu(111). J. Chem. Soc. Faraday Trans. 86, 2725.

Navrotsky, A., Kleppa, O.J., 1967. The thermodynamics of cation distributions in simple spinels. J. Inorg. Nucl. Chem. 29, 2701 – 2714.

Ndione, P.F., Shi, Y., Stevanovic, V., Lany, S., Zakutayev, A., Parilla, P.A., Perkins, J.D., Berry, J.J., Ginley, D.S., Toney, M.F., 2014. Control of the Electrical

Properties in Spinel Oxides by Manipulating the Cation Disorder. Adv. Funct. Mater. 24, 610–618.

Néel, L., 1948. Magnetic properties of ferrites: ferrimagnetism and antiferromagnetism. Ann. Phys. (Paris). 3, 137 – 198.

Néel, L., 1954. L'approche à la saturation de la magnétostriction. J. Phys. le Radium 15, 376–378.

Nesson, M.H., Lowenstam, H.A., 1985. Biomineralization proceses of radula teeth of chitons. In: Kirschvink, J.L., Stone, D.S. (Eds.), Magnetite Biomineralization and Magneto Reception in Organisms. Plenum, New York, pp. 333–363.

Neugebauer, J., Scheffler, M., 1992. Adsorbate-substrate and adsorbate-adsorbate interactions of Na and K adlayers on Al(111). Phys. Rev. B 46, 16067–16080.

Nie, S., Starodub, E., Monti, M., Siegel, D.A., Vergara, L., El Gabaly, F., Bartelt, N.C., de la Figuera, J., McCarty, K.F., 2013. Insight into magnetite's redox catalysis from observing surface morphology during oxidation. J. Am. Chem. Soc. 135, 10091–10098.

Nielsen, A., 1981. Ammonia Synthesis: Exploratory and Applied Research. Catal. Rev. 23, 17–51.

Noll, W., 1980. Chemie vor unserer Zeit: Antike Pigmente. Chemie unserer Zeit 14, 37–43.

Nozaki, T., Kubota, H., Fukushima, A., Yuasa, S., 2013. Enhanced Tunnel Magnetoresistance Effect in an Epitaxial Magnetic Tunnel Junction with a Hybrid γ-Fe_2O_3/MgO Barrier. Appl. Phys. Express 6, 053005.

Nyström, J.O., Lindström, M., Wickman, F.E., 1988. Discovery of a second Ordovician meteorite using chromite as a tracer. Nature 336, 572–574.

O'Neill, H.S.C., Navrotsky, A., 1983. Simple spinels: crystallographic parameters, cation radii, lattice energies, and cation distribution. Am. Mineral. 68, 181 – 194.

Ohgushi, K., Okimoto, Y., Ogasawara, T., Miyasaka, S., Tokura, Y., 2008. Magnetic, Optical, and Magnetooptical Properties of Spinel-Type ACr_2X_4 (A = Mn, Fe, Co, Cu, Zn, Cd; X = O, S, Se). J. Phys. Soc. Japan 77, 034713.

Olsen, R.A., Kroes, G.J., Henkelman, G., Arnaldsson, A., Jónsson, H., 2004. Comparison of methods for finding saddle points without knowledge of the final states. J. Chem. Phys. 121, 9776–92.

Pacchioni, G., 2001. Theory of point defects at the MgO surface. In: Woodruff, D.P. (Ed.), The Chemical Physics of Solid Surfaces - Oxide Surfaces - Volume 9. Elsevier B.V., pp. 94–135.

Palin, E.J., Walker, A.M., Harrison, R.J., 2008. A computational study of order-disorder phenomena in Mg_2TiO_4 spinel (qandilite). Am. Mineral. 93, 1363–1372.

Papike, J.J., Hodges, F.N., Bence, A.E., Cameron, M., Rhodes, J.M., 1976. Mare basalts: Crystal chemistry, mineralogy, and petrology. Rev. Geophys. 14, 475–540.

Park, J.-H., Tjeng, L.H., Allen, J.W., Metcalf, P., Chen, C.T., 1997. Single-particle gap above the Verwey transition in Fe_3O_4. Phys. Rev. B Condens. Matter 55, 12813–12817.

Park, M.S., Kwon, S.K., Youn, S.J., Min, B.I., 1999. Half-metallic electronic structures of giant magnetoresistive spinels: $Fe_{1-x}Cu_xCr_2S_4$ (x = 0.0, 0.5, 1.0). Phys. Rev. B 59, 10018 – 10024.

Park, S., Ishikawa, T., Tokura, Y., 1998. Charge-gap formation upon the Verwey transition in Fe_3O_4. Phys. Rev. B 58, 3717–3720.

Parkinson, G.S., Manz, T.A., Novotný, Z., Sprunger, P.T., Kurtz, R.L., Schmid, M., Sholl, D.S., Diebold, U., 2012. Antiphase domain boundaries at the Fe_3O_4(001) surface. Phys. Rev. B 85, 195450.

Parkinson, G.S., Novotný, Z., Jacobson, P., Schmid, M., Diebold, U., 2011. A metastable Fe(A) termination at the Fe_3O_4(001) surface. Surf. Sci. 605, L42–L45.

Pashley, M.D., 1989. Electron counting model and its application to island structures on molecular-beam epitaxy grown GaAs(001) and ZnSe(001). Phys. Rev. B 40, 10481–10487.

Pentcheva, R., Wendler, F., Meyerheim, H.L., Moritz, W., Jedrecy, N., Scheffler, M., 2005. Jahn-Teller Stabilization of a “Polar” Metal Oxide Surface: Fe_3O_4(001). Phys. Rev. Lett. 94, 126101.

Peralta, J.E., Heyd, J., Scuseria, G.E., Martin, R.L., 2006. Spin-orbit splittings and energy band gaps calculated with the Heyd-Scuseria-Ernzerhof screened hybrid functional. Phys. Rev. B 74, 073101.

Perdew, J.P., Burke, K., Ernzerhof, M., 1996a. Generalized Gradient Approximation Made Simple. Phys. Rev. Lett. 77, 3865–3868.

Perdew, J.P., Burke, K., Ernzerhof, M., 1997. Generalized Gradient Approximation Made Simple [Phys. Rev. Lett. 77, 3865 (1996)]. Phys. Rev. Lett. 78, 1396–1396.

Perdew, J.P., Chevary, J.A., Vosko, S.H., Jackson, K.A., Pederson, M.R., Singh, D.J., Fiolhais, C., 1992. Atoms, molecules, solids, and surfaces: Applications of the generalized gradient approximation for exchange and correlation. Phys. Rev. B 46, 6671–6687.

Perdew, J.P., Chevary, J.A., Vosko, S.H., Jackson, K.A., Pederson, M.R., Singh, D.J., Fiolhais, C., 1993. Erratum: Atoms, molecules, solids, and surfaces: Applications of the generalized gradient approximation for exchange and correlation. Phys. Rev. B 48, 4978–4978.

Perdew, J.P., Ernzerhof, M., Burke, K., 1996b. Rationale for mixing exact exchange with density functional approximations. J. Chem. Phys. 105, 9982–9985.

Perdew, J.P., Ruzsinszky, A., Csonka, G.I., Vydrov, O.A., Scuseria, G.E., Constantin, L.A., Zhou, X., Burke, K., 2008. Restoring the Density-Gradient Expansion for Exchange in Solids and Surfaces. Phys. Rev. Lett. 100, 136406.

Perdew, J.P., Zunger, A., 1981. Self-interaction correction to density-functional approximations for many-electron systems. Phys. Rev. B 23, 5048–5079.

Petersen, N., von Dobeneck, T., Vali, H., 1986. Fossil bacterial magnetite in deep-sea sediments from the South Atlantic Ocean. Nature 320, 611–615.

Pichler, H., Schulz, H., 1970. Neuere Erkenntnisse auf dem Gebiet der Synthese von Kohlenwasserstoffen aus CO und H_2. Chemie Ing. Tech. - CIT 42, 1162–1174.

Piekarz, P., Oleś, A.M., Parlinski, K., 2010. Comparative study of the electronic structures of Fe_3O_4 and Fe_2SiO_4. Acta Phys. Pol. A 118, 307 – 312.

Pomiès, M.P., Menu, M., Vignaud, C., 1999. TEM observations of goethite dehydration: application to archaeological samples. J. Eur. Ceram. Soc. 19, 1605–1614.

Pugh, S.F., 1954. XCII. Relations between the elastic moduli and the plastic properties of polycrystalline pure metals. Philos. Mag. Ser. 7 45, 823–483.

Pulay, P., 1980. Convergence acceleration of iterative sequences. the case of SCF iteration. Chem. Phys. Lett. 73, 393–398.

Ramdohr, P., 1967. Chromite and chromite chondrules in meteorites—I. Geochim. Cosmochim. Acta 31, 1961–1967.

Ramirez, A.P., Cava, R.J., Krajewski, J., 1997. Colossal magnetoresistance in Cr-based chalcogenide spinels. Nature 386, 156 – 159.

Regazzoni, A.E., Urrutia, G.A., Blesa, M.A., Maroto, A.J.G., 1981. Some observations on the composition and morphology of synthetic magnetites obtained by different routes. J. Inorg. Nucl. Chem. 43, 1489–1493.

Reichmann, H.J., Jacobsen, S.D., 2004. High-pressure elasticity of a natural magnetite crystal. Am. Mineral. 89, 1061–1066.

Rethwisch, D.G., Dumesic, J.A., 1986. The effects of metal-oxygen bond strength on properties of oxides: II. Water-gas shift over bulk oxides. Appl. Catal. 21, 97–109.

Rethwisch, D.G., Phillips, J., Chen, Y., Hayden, T.F., Dumesic, J.A., 1985. Water-gas shift over magnetite particles supported on graphite: Effects of treatments in CO/CO_2 and H_2/H_2O gas mixtures. J. Catal. 91, 167–180.

Reuter, K., Scheffler, M., 2001. Composition, structure, and stability of $RuO_2(110)$ as a function of oxygen pressure. Phys. Rev. B 65, 035406.

Rhodes, C., Hutchings, G.J., Ward, A.M., 1995. Water-gas shift reaction: finding the mechanistic boundary. Catal. Today 23, 43–58.

Rigby, V., Middleton, A.P., Freestone, I.C., 1989. The Prunay workshop: Technical examination of La Tène bichrome painted pottery from Champagne. World Archaeol. 21, 1–16.

Rimstidt, J.D., Vaughan, D.J., 2003. Pyrite oxidation: a state-of-the-art assessment of the reaction mechanism. Geochim. Cosmochim. Acta 67, 873–880.

Ritter, M., Weiss, W., 1999. $Fe_3O_4(111)$ surface structure determined by LEED crystallography. Surf. Sci. 432, 81–94.

Robbins, M., Wertheim, G.K., Sherwood, R.C., Buchanan, D.N.E., 1971. Magnetic Properties and Site Distributions in the System $FeCr_2O_4$-Fe_3O_4, ($Fe^{2+}Cr_{2-x}Fe^{3+}_xO_4$). Le J. Phys. Colloq. 32, C1–266–C1–267.

Roberts, A.P., Turner, G.M., 1993. Diagenetic formation of ferrimagnetic iron sulphide minerals in rapidly deposited marine sediments, South Island, New Zealand. Earth Planet. Sci. Lett. 115, 257–273.

Roberts, A.P., Weaver, R., 2005. Multiple mechanisms of remagnetization involving sedimentary greigite (Fe_3S_4). Earth Planet. Sci. Lett. 231, 263–277.

Rohrbach, A., Hafner, J., Kresse, G., 2003. Electronic correlation effects in transition-metal sulfides. J. Phys. Condens. Matter 15, 979 – 996.

Roldan, A., de Leeuw, N.H., 2015. Water Dissociation on (001), (011) and (111) Fe3S4 Surfaces. To be Submitted.

Roldán, A., Novell, G., Ricart, J.M., Illas, F., 2010. Theoretical Simulation of Temperature Programmed Desorption of Molecular Oxygen on Isolated Au Nanoparticles from Density Functional Calculations and Microkinetics Models. J. Phys. Chem. C 114, 5101–5106.

Roldan, A., Santos-Carballal, D., de Leeuw, N.H., 2013. A comparative DFT study of the mechanical and electronic properties of greigite Fe_3S_4 and magnetite Fe_3O_4. J. Chem. Phys. 138, 204712.

Rollmann, G., Rohrbach, A., Entel, P., Hafner, J., 2004. First-principles calculation of the structure and magnetic phases of hematite. Phys. Rev. B 69, 165107.

Russell, M.J., Hall, a. J., 1997. The emergence of life from iron monosulphide bubbles at a submarine hydrothermal redox and pH front. J. Geol. Soc. London. 154, 377–402.

Russell, M.J., Martin, W., 2004. The rocky roots of the acetyl-CoA pathway. Trends Biochem. Sci. 29, 358–63.

Rustad, J.R., Wasserman, E., Felmy, A.R., 1999. A molecular dynamics investigation of surface reconstruction on magnetite (001). Surf. Sci. 432, L583–L588.

Ruzsinszky, A., Perdew, J.P., Csonka, G.I., 2005. Binding energy curves from nonempirical density functionals II. van der Waals bonds in rare-gas and alkaline-earth diatomics. J. Phys. Chem. A 109, 11015–21.

Santos-Carballal, D., Roldan, A., Grau-Crespo, R., de Leeuw, N.H., 2014. A DFT study of the structures, stabilities and redox behaviour of the major surfaces of magnetite Fe_3O_4. Phys. Chem. Chem. Phys. 16, 21082–21097.

Sanville, E., Kenny, S.D., Smith, R., Henkelman, G., 2007. Improved grid-based algorithm for Bader charge allocation. J. Comput. Chem. 28, 899 – 908.

Sapieszko, R.S., Matijević, E., 1980. Preparation of well-defined colloidal particles by thermal decomposition of metal chelates. I. Iron oxides. J. Colloid Interface Sci. 74, 405–422.

Sarel, S., Avramovic-Grisaru, S., Bauminger, E.R., Felner, I., Nowik, I., Williams, R.J.P., Hughes, N.P., 1989. A novel ferromagnetic inorganic-organic host-guest system. Synthesis of crystalline small magnetite particles complexed with bis(pyridoxylidenehydrazino)phthalazine (DPDHP) at ambient temperature and neutral pH. Inorg. Chem. 28, 4183–4187.

Satterfield, C.N., Hanlon, R.T., Tung, S.E., Zou, Z.M., Papaefthymiou, G.C., 1986. Effect of water on the iron-catalyzed Fischer-Tropsch synthesis. Ind. Eng. Chem. Prod. Res. Dev. 25, 407–414.

Sawatzky, G., Allen, J., 1984. Magnitude and Origin of the Band Gap in NiO. Phys. Rev. Lett. 53, 2339–2342.

Schikorr, G., 1929. Über die Reaktionen zwischen Eisen, Seinen Hydroxyden und Wasser. Zeitschrift für Elektrochemie und Angew. Phys. Chemie 35, 65–70.

Schippers, A., Sand, W., 1999. Bacterial leaching of metal sulfides proceeds by two indirect mechanisms via thiosulfate or via polysulfides and sulfur. Appl. Environ. Microbiol. 65, 319–21.

Scholten, J.J.F., Zwietering, P., Konvalinka, J.A., de Boer, J.H., 1959. Chemisorption of nitrogen on iron catalysts in connection with ammonia synthesis. Part 1.-The kinetics of the adsorption and desorption of nitrogen. Trans. Faraday Soc. 55, 2166.

Schüler, D., 1999. Formation of magnetosomes in magnetotactic bacteria. J. Mol. Microbiol. Biotechnol. 1, 79–86.

Seko, A., Oba, F., Tanaka, I., 2010. Classification of spinel structures based on first-principles cluster expansion analysis. Phys. Rev. B 81, 054114.

Seminovski, Y., Palacios, P., Wahnón, P., Grau-Crespo, R., 2012. Band gap control via tuning of inversion degree in $CdIn_2S_4$ spinel. Appl. Phys. Lett. 100, 102112.

Shafer, M.W., 1962. Preparation and Properties of Ferrospinels Containing Ni^{3+}. J. Appl. Phys. 33, 1210 – 1211.

Shannon, R.D., 1976. Revised effective ionic radii and systematic studies of interatomic distances in halides and chalcogenides. Acta Crystallogr. Sect. A 32, 751 – 767.

Shein, I.R., Ivanovskii, A.L., 2008. Elastic properties of quaternary oxypnictides LaOFeAs and LaOFeP as basic phases for new 26–52K superconducting materials from first principles. Scr. Mater. 59, 1099–1102.

Sheppard, D., Terrell, R., Henkelman, G., 2008. Optimization methods for finding minimum energy paths. J. Chem. Phys. 128, 134106.

Shirane, G., Cox, D.E., Pickart, S.J., 1964. Magnetic Structures in $FeCr_2S_4$ and $FeCr_2O_4$. J. Appl. Phys. 35, 954 – 955.

Shull, C.G., Wollan, E.O., Koehler, W.C., 1951. Neutron Scattering and Polarization by Ferromagnetic Materials. Phys. Rev. 84, 912 – 921.

Sidhu, P.S., Gilkes, R.J., Posner, A.M., 1978. The synthesis and some properties of Co, Ni, Zn, Cu, Mn and Cd substituted magnetites. J. Inorg. Nucl. Chem. 40, 429–435.

Sidhu, P.S., Gilkes, R.J., Posner, A.M., 1980. The Behavior of Co, Ni, Zn, Cu, Mn, and Cr in Magnetite during Alteration to Maghemite and Hematite1. Soil Sci. Soc. Am. J. 44, 135.

Sinha, A.P.B., Sanjana, N.R., Biswas, A.B., 1957. On the structure of some anganites. Acta Crystallogr. 10, 439–440.

Siratori, K., Kino, Y., 1980. A note on the magnetic anisotropy of Fe_3O_4. J. Magn. Magn. Mater. 20, 87–90.

Skinner, B.J., Erd, R.C., Grimaldi, F.S., 1964. Greigite, the Thio-spinel of Iron; a New Mineral. Am. Mineral. 49, 543 – 555.

Slick, P.I., 1980. Ferrites for Non-Microwave Applications. In: Wohlfarth, E.P. (Ed.), Ferromagnetic Materials. A Handbook on the Properties of Magnetically Ordered Substances. Volume 2. North-Holland Publishing Company, Amsterdam, pp. 189 – 242.

Smith, P.A., Spencer, C.D., Stillwell, R.P., 1978. Co^{57} and Fe^{57} Mössbauer studies of the spinels $FeCo_2O_4$ and $Fe_{0.5}Co_{2.5}O_4$. J. Phys. Chem. Solids 39, 107 – 111.

Snowball, I., Thompson, R., 1990a. A mineral magnetic study of Holocene sedimentation in Lough Catherine, Northern Ireland. Boreas 19, 127–146.

Snowball, I., Thompson, R., 1990b. A stable chemical remanence in Holocene sediments. J. Geophys. Res. 95, 4471.

Snowball, I.F., 1991. Magnetic hysteresis properties of greigite (Fe_3S_4) and a new occurrence in Holocene sediments from Swedish Lappland. Phys. Earth Planet. Inter. 68, 32–40.

Somorjai, G.A., Salmeron, M., 1986. Surface properties of catalysts. Iron and its oxides. Surface chemistry, photochemistry and catalysis. In: Pelizzetti, E., Serpone, N. (Eds.), Homogeneous and Heterogeneous Photocatalysis. D. Reidel Publ. Co., Doordrecht, The Netherlands, NATO ASI Series C, 174, pp. 445–478.

Spencer, N.D., Schoonmaker, R.C., Somorjai, G.A., 1982. Iron single crystals as ammonia synthesis catalysts: Effect of surface structure on catalyst activity. J. Catal. 74, 129–135.

Spender, M.R., Coey, J.M.D., Morrish, A.H., 1972. The Magnetic Properties and Mössbauer Spectra of Synthetic Samples of Fe_3S_4. Can. J. Phys. 50, 2313 – 2326.

Spiridis, N., Barbasz, J., Łodziana, Z., Korecki, J., 2006. Fe_3O_4(001) films on Fe(001): Termination and reconstruction of iron-rich surfaces. Phys. Rev. B 74, 155423.

Stanka, B., Hebenstreit, W., Diebold, U., Chambers, S.A., 2000. Surface reconstruction of Fe_3O_4(001). Surf. Sci. 448, 49–63.

Stixrude, L., Cohen, R., Singh, D., 1994. Iron at high pressure: Linearized-augmented-plane-wave computations in the generalized-gradient approximation. Phys. Rev. B 50, 6442–6445.

Stoltze, P., 2000. Microkinetic simulation of catalytic reactions. Prog. Surf. Sci. 65, 65–150.

Stolz, J.F., Chang, S.-B.R., Kirschvink, J.L., 1986. Magnetotactic bacteria and single-domain magnetite in hemipelagic sediments. Nature 321, 849–851.

Sugimoto, T., Matijević, E., 1980. Formation of uniform spherical magnetite particles by crystallization from ferrous hydroxide gels. J. Colloid Interface Sci. 74, 227–243.

Sukegawa, H., Miura, Y., Muramoto, S., Mitani, S., Niizeki, T., Ohkubo, T., Abe, K., Shirai, M., Inomata, K., Hono, K., 2012. Enhanced tunnel magnetoresistance in a spinel oxide barrier with cation-site disorder. Phys. Rev. B 86, 184401.

Suleimenov, O.M., Krupp, R.E., 1994. Solubility of hydrogen sulfide in pure water and in NaCl solutions, from 20 to 320°C and at saturation pressures. Geochim. Cosmochim. Acta 58, 2433–2444.

Suleimenov, O.M., Seward, T.M., 1997. A spectrophotometric study of hydrogen sulphide ionisation in aqueous solutions to 350°C. Geochim. Cosmochim. Acta 61, 5187–5198.

Surerus, K.K., Kennedy, M.C., Beinert, H., Münck, E., 1989. Mössbauer study of the inactive Fe_3S_4 and Fe_3Se_4 and the active Fe_4Se_4 forms of beef heart aconitase. Proc. Natl. Acad. Sci. U. S. A. 86, 9846–50.

Szotek, Z., Temmerman, W.M., Ködderitzsch, D., Svane, A., Petit, L., Winter, H., 2006. Electronic structures of normal and inverse spinel ferrites from first principles. Phys. Rev. B 74, 174431.

Taberna, P.L., Mitra, S., Poizot, P., Simon, P., Tarascon, J.-M., 2006. High rate capabilities Fe_3O_4-based Cu nano-architectured electrodes for lithium-ion battery applications. Nat. Mater. 5, 567–73.

Tafreshi, S.S., Roldan, A., Dzade, N.Y., de Leeuw, N.H., 2014. Adsorption of hydrazine on the perfect and defective copper (111) surface: A dispersion-corrected DFT study. Surf. Sci. 622, 1–8.

Takahashi, M., Fine, M.E., 1972. Magnetic behavior of quenched and aged $CoFe_2O_4$-Co_3O_4 alloys. J. Appl. Phys. 43, 4205 – 4216.

Tamaura, Y., Ito, K., Katsura, T., 1983. Transformation of γ-FeO(OH) to Fe_3O_4 by adsorption of iron(II) ion on γ-FeO(OH). J. Chem. Soc. Dalt. Trans. 189.

Tanaka, M., Tokoro, T., Aiyama, Y., 1966. Jahn-Teller Effects on Mössbauer Spectra of Fe^{57} in $FeCr_2O_4$ and FeV_2O_4. J. Phys. Soc. Japan 21, 262–267.

Tang, W., Sanville, E., Henkelman, G., 2009. A grid-based Bader analysis algorithm without lattice bias. J. Phys. Condens. Matter 21, 084204.

Tasker, P.W., 1979. The stability of ionic crystal surfaces. J. Phys. C Solid State Phys. 12, 4977–4984.

Taylor, R.M., Schwertmann, U., 1974. Maghemite in Soils and Its Origin. II Maghemite Synthesis at Ambient Temperature and pH 7. Clay Miner. 10, 299–310.

Tenailleau, C., Etschmann, B., Ibberson, R.M., Pring, A., 2006. A neutron powder diffraction study of Fe and Ni distributions in synthetic pentlandite and violarite using ^{60}Ni isotope. Am. Mineral. 91, 1442–1447.

Terakura, K., Oguchi, T., Williams, A., Kübler, J., 1984. Band theory of insulating transition-metal monoxides: Band-structure calculations. Phys. Rev. B 30, 4734–4747.

Tersoff, J., Hamann, D.R., 1985. Theory of the scanning tunneling microscope. Phys. Rev. B 31, 805–813.

Tielens, F., Calatayud, M., Franco, R., Recio, J.M., Pérez-Ramírez, J., Minot, C., 2006. Periodic DFT study of the structural and electronic properties of bulk $CoAl_2O_4$ spinel. J. Phys. Chem. B 110, 988–95.

Tkatchenko, A., DiStasio, R.A., Car, R., Scheffler, M., 2012. Accurate and Efficient Method for Many-Body van der Waals Interactions. Phys. Rev. Lett. 108, 236402.

Tkatchenko, A., Scheffler, M., 2009. Accurate Molecular Van Der Waals Interactions from Ground-State Electron Density and Free-Atom Reference Data. Phys. Rev. Lett. 102, 073005.

Topham, S., 1985. The hystory of the catalytic synthesis of ammonia. In: Anderson, J.R. (Ed.), Catalysis: Science and Technology. Springer, Berlin 7, pp. 1–50.

Topsøe, H., Boudart, M., 1973. Mössbauer spectroscopy of CO shift catalysts promoted with lead. J. Catal. 31, 346–359.

Torres de Araujo, F.F., Pires, M.A., Frankel, R.B., Bicudo, C.E.M., 1986. Magnetite and Magnetotaxis in Algae. Biophys. J. 50, 375–378.

Torres-Ruiz, J., 1983. Genesis and evolution of the Marquesado and adjacent iron ore deposits, Granada, Spain. Econ. Geol. 78, 1657–1673.

Towe, K.M., Lowenstam, H.A., 1967. Ultrastructure and development of iron mineralization in the radular teeth of Cryptochiton stelleri (mollusca). J. Ultrastruct. Res. 17, 1–13.

Townsend, M.G., Gosselin, J.R., Horwood, J.L., Ripley, L.G., Tremblay, R.J., 1977. Violarite, a metallic natural spinel. Phys. Status Solidi 40, K25 – K29.

Vali, H., Kirschvink, J.L., 1991. Observations of magnetosome organization, surface structure, and iron biomineralization of undescribed magnetic bacteria: Evolutionary speculations. In: Frankel, R.B., Blakemore, R.P. (Eds.), Iron Biominerals. Plenum Press, New York, pp. 97–115.

Van Landuyt, J., De Ridder, R., Brabers, V.A.M., Amelinckx, S., 1972. Jahn-Teller domains in $Mn_xFe_{3-x}O_4$ as observed by electron microscopy. Mater. Res. Bull. 7, 327 – 338.

Vandenberghe, R.E., De Grave, E., De Bakker, P.M.A., Krs, M., Hus, J.J., 1991. Mössbauer effect study of natural greigite. Hyperfine Interact. 68, 319 – 322.

Vanderbilt, D., 1990. Soft self-consistent pseudopotentials in a generalized eigenvalue formalism. Phys. Rev. B 41, 7892–7895.

Vanpoucke, D.E.P., Brocks, G., 2008. Formation of Pt-induced Ge atomic nanowires on Pt/Ge(001): A density functional theory study. Phys. Rev. B 77, 241308.

Vaughan, D.J., Craig, J.R., 1978. Mineral chemistry of metal sulfides. Cambridge University Press, Cambridge, United Kingdom.

Vaughan, D.J., Craig, J.R., 1985. The crystal chemistry of iron-nickel thiospinels. Am. Mineral. 70, 1036 – 1043.

Vaughan, D.J., Ridout, M.S., 1971. Mössbauer studies of some sulphide minerals. J. Inorg. Nucl. Chem. 33, 741 – 746.

Vaughan, D.J., Tossell, J.A., 1981. Electronic structure of thiospinel minerals: results from MO calculation. Am. Mineral. 66, 1250 – 1253.

Verwey, E.J.W., 1939. Electronic Conduction of Magnetite (Fe_3O_4) and its Transition Point at Low Temperatures. Nature 144, 327 – 328.

Voigt, W., 1928. Lehrbuch der kristallphysik (mit ausschluss der kristalloptik). B.G. Teubner, Leipzig Berlin.

Voogt, F.C., Fujii, T., Smulders, P.J.M., Niesen, L., James, M.A., Hibma, T., 1999. NO_2-assisted molecular-beam epitaxy of Fe_3O_4, $Fe_{3-\delta}O_4$, and γ-Fe_2O_3 thin films on MgO(100). Phys. Rev. B 60, 11193–11206.

Vosko, S.H., Wilk, L., Nusair, M., 1980. Accurate spin-dependent electron liquid correlation energies for local spin density calculations: a critical analysis. Can. J. Phys. 58, 1200–1211.

Wagner, W., Pruss, A., 1993. International Equations for the Saturation Properties of Ordinary Water Substance. Revised According to the International Temperature Scale of 1990. Addendum to J. Phys. Chem. Ref. Data 16, 893 (1987). J. Phys. Chem. Ref. Data 22, 783.

Walcott, C., Gould, J., Kirschvink, J., 1979. Pigeons have magnets. Science 205, 1027–1029.

Waldner, P., 2009. Thermodynamic modelling of violarite. J. Chem. Thermodyn. 41, 171 – 174.

Walsh, A., Wei, S.-H., Yan, Y., Al-Jassim, M.M., Turner, J.A., Woodhouse, M., Parkinson, B.A., 2007. Structural, magnetic, and electronic properties of the Co-Fe-Al oxide spinel system: Density-functional theory calculations. Phys. Rev. B 76, 165119.

Wang, L., Maxisch, T., Ceder, G., 2006. Oxidation energies of transition metal oxides within the GGA+U framework. Phys. Rev. B 73, 195107.

Wang, X., Zhang, R., Wu, C., Dai, Y., Song, M., Gutmann, S., Gao, F., Lv, G., Li, J., Li, X., Guan, Z., Fu, D., Chen, B., 2007. The application of Fe_3O_4 nanoparticles in cancer research: a new strategy to inhibit drug resistance. J. Biomed. Mater. Res. A 80, 852–60.

Wang, X.-G., Weiss, W., Shaikhutdinov, S.K., Ritter, M., Petersen, M., Wagner, F., Schlögl, R., Scheffler, M., 1998. The Hematite (α-Fe_2O_3) (0001) Surface: Evidence for Domains of Distinct Chemistry. Phys. Rev. Lett. 81, 1038–1041.

Watson, G.W., Kelsey, E.T., de Leeuw, N.H., Harris, D.J., Parker, S.C., 1996. Atomistic simulation of dislocations, surfaces and interfaces in MgO. J. Chem. Soc. Faraday Trans. 92, 433–438.

Webb, J., Macey, D., Mann, S., 1989. Biomineralization of iron in molluscan teeth. In: Mann, S., Webb, J., Williams, R. (Eds.), Biomineralization: Chemical and Biochemical Perspectives. VCH, Weinheim, pp. 345–387.

Wei, H., Wang, E., 2008. Fe_3O_4 magnetic nanoparticles as peroxidase mimetics and their applications in H_2O_2 and glucose detection. Anal. Chem. 80, 2250–4.

Wei, S.-H., Zhang, S., 2001. First-principles study of cation distribution in eighteen closed-shell $A^{II}B_2^{III}O_4$ and $A^{IV}B_2^{II}O_4$ spinel oxides. Phys. Rev. B 63, 045112.

Weiss, W., Ranke, W., 2002. Surface chemistry and catalysis on well-defined epitaxial iron-oxide layers. Prog. Surf. Sci. 70, 1–151.

Westrik, R., 1953. On the Lattice Parameters and Curie Points of Unreduced Iron Catalysts. J. Chem. Phys. 21, 2094.

Wiberg, K.B., Rablen, P.R., 1993. Comparison of atomic charges derived via different procedures. J. Comput. Chem. 14, 1504–1518.

Wilkin, R.T., Barnes, H.L., 1996. Pyrite formation by reactions of iron monosulfides with dissolved inorganic and organic sulfur species. Geochim. Cosmochim. Acta 60, 4167–4179.

Williamson, M.A., Rimstidt, J.D., 1994. The kinetics and electrochemical rate-determining step of aqueous pyrite oxidation. Geochim. Cosmochim. Acta 58, 5443–5454.

Wood, D.M., Zunger, A., 1985. A new method for diagonalising large matrices. J. Phys. A. Math. Gen. 18, 1343–1359.

Wood, E.A., 1964. Vocabulary of Surface Crystallography. J. Appl. Phys. 35, 1306–1312.

Wright, J.P., Attfield, J.P., Radaelli, P.G., 2002. Charge ordered structure of magnetite Fe_3O_4 below the Verwey transition. Phys. Rev. B 66, 214422.

Wu, X., Vanderbilt, D., Hamann, D., 2005. Systematic treatment of displacements, strains, and electric fields in density-functional perturbation theory. Phys. Rev. B 72, 1–13.

Wu, Y., Hu, W., 2007. Elastic and brittle properties of the B2-MgRE (RE = Sc, Y, Ce, Pr, Nd, Gd, Tb, Dy, Ho, Er) intermetallics. Eur. Phys. J. B 60, 75–81.

Wulff, G., 1901. On the question of speed of growth and dissolution of crystal surfaces. Z. Krystallogr. Minera. 34, 449–530.

Yafet, Y., Kittel, C., 1952. Antiferromagnetic Arrangements in Ferrites. Phys. Rev. 87, 290–294.

Younger, P.L., 2002. Mine water pollution from Kernow to Kwazulu-Natal: geochemical remedial options and their selection in practice. Geosci. south-west Engl. 10, 255–266.

Zaanen, J., Sawatzky, G., Allen, J., 1985. Band gaps and electronic structure of transition-metal compounds. Phys. Rev. Lett. 55, 418–421.

Zhang, B., de Wijs, G., de Groot, R.A., 2012. Switchable Fermi surface sheets in greigite. Phys. Rev. B 86, 2–5.

Zhang, L., Zhang, Y., 2009. Fabrication and magnetic properties of Fe_3O_4 nanowire arrays in different diameters. J. Magn. Magn. Mater. 321, L15–L20.

Zhang, Z., Satpathy, S., 1991. Electron states, magnetism, and the Verwey transition in magnetite. Phys. Rev. B 44, 13319 – 13331.

Zhao, L., Zhang, H., Xing, Y., Song, S., Yu, S., Shi, W., Guo, X., Yang, J., Lei, Y., Cao, F., 2008. Morphology-Controlled Synthesis of Magnetites with Nanoporous Structures and Excellent Magnetic Properties. Chem. Mater. 20, 198–204.

Zhu, M., Diao, G., 2011. Synthesis of Porous Fe_3O_4 Nanospheres and Its Application for the Catalytic Degradation of Xylenol Orange. J. Phys. Chem. C 115, 18923–18934.

Žutić, I., Fabian, J., Das Sarma, S., 2004. Spintronics: Fundamentals and applications. Rev. Mod. Phys. 76, 323 – 410.